



HAL
open science

Multiscale Relationships in Polymer-Based Heterogeneous Systems: Experiments and Simulations

Flandin Lionel

► **To cite this version:**

Flandin Lionel. Multiscale Relationships in Polymer-Based Heterogeneous Systems: Experiments and Simulations. Mechanics [physics.med-ph]. Université de Savoie, 2006. tel-00454578

HAL Id: tel-00454578

<https://theses.hal.science/tel-00454578>

Submitted on 8 Feb 2010

HAL is a multi-disciplinary open access archive for the deposit and dissemination of scientific research documents, whether they are published or not. The documents may come from teaching and research institutions in France or abroad, or from public or private research centers.

L'archive ouverte pluridisciplinaire **HAL**, est destinée au dépôt et à la diffusion de documents scientifiques de niveau recherche, publiés ou non, émanant des établissements d'enseignement et de recherche français ou étrangers, des laboratoires publics ou privés.

Multiscale Relationships in Polymer-Based Heterogeneous Systems: Experiments and Simulations

Lionel Flandin

Mémoire d'Habilitation à Diriger des Recherches

Présentée et soutenue publiquement le 27 Octobre 2006

Jury:

Prof. N.D. Albérola	LMOPS	Université de Savoie	Examineur
Prof. E. Baer	CAPRI	CWRU, Cleveland	Président
Prof. Y. Bréchet	LTPCM	INP de Grenoble	Rapporteur
Prof. C. Brosseau	LEST	U. Bretagne Occidentale	Examineur
Prof. J.-Y. Cavallé	GEMPPM	INSA de Lyon	Rapporteur
Prof. A. Hiltner	CAPRI	CWRU, Cleveland	Rapporteur

Laboratoire Matériaux Organiques à Propriétés Spécifiques,
UMR 5041 Université de Savoie - CNRS

We have a word game in English called “Twenty questions.” To play Twenty Questions, one player imagines some object, and the other players must guess what it is by asking questions that can be answered with a “yes” or a “no.” I imagine every language has a similar game, and, for those of us who speak the language of science, the game is called The Scientific Method.

Barry K. Sharpless
Speech at the Nobel Banquet
December 10, 2001

“Foreword”: what is this document?

1- Why does one need an “HDR”?

Although not as clearly defined as Ph.D.’s, the “Habilitation à Diriger des Recherches” is an important step for French faculty (similar degrees do exist in other European countries, and outside Europe as well). There are two reasons for this:

- The main reason is for them to be eligible for promotions.
- The degree also allows someone to be the official advisor of Ph.D. students.

2- How does one get the “HDR”?

This HDR report and defence are meant, roughly following the official text, to:

- Show an innovative approach in a given scientific area.
- Describe the ability to conduct scientific research.

3- Please note ...

This report isn’t a Ph.D. (or a “second Ph.D.”, like it used to be). The main difference with a Ph.D., is that this is not based on original results. It also is supposed to be broader than a Ph.D. and yet more concise¹. It can’t be considered as a review of the literature either, because it is essentially based on the papers co-authored by the candidate.

——— ✎ *How do I quote this report?* ———

Please don’t!

**Although you *will* find unpublished materials
in it, this manuscript is essentially based on
co-authored papers, quote them preferentially**

Thank you !

¹As a result the original publications were modified and reorganized. You may sometimes have to read the original papers to find experimental details.

Acknowledgements

Je tiens à remercier chaleureusement les personnes qui ont contribué à ce travail, d'un point de vue scientifique et humain.

- N.D. Albérola, P. Mélé, C. Bas
LMOPS, Université de Savoie , Le Bourget du Lac
- G. Canova
GPM2, Grenoble, France
- A. Hiltner, E. Baer
CAPRI, Case Western Reserve University, Cleveland, OH
- J.Y. Cavaillé
GEMPPM, Lyon, France
- Y. Bréchet
LTPCM, Grenoble, France
- K. Schulte
TUHH, Hambourg, Germany
- L.A. Dissado
Leicester University, UK
- L. Vouyovitch, J.C. Honoré
LMOPS, Université de Savoie , Le Bourget du Lac
- Les collègues du LMOPS et du DUT SGM
En particulier Jean-Louis Martin
- J. Shewchuk, (pour Triangle)
University of California at Berkeley
- W. Rasband, (pour ImageJ)
National Institutes of Health

Contents

Introduction	1
I Conducting fillers	3
1 meso macro relationships	11
1.1 Introduction	12
1.2 2D systems	12
1.3 3D systems	14
1.4 Conclusion	20
2 in situ damage monitoring	21
2.1 Introduction	22
2.2 Materials and methods	22
2.3 Results and discussion	24
2.4 Conclusion	30
3 Control of the structure	31
3.1 Percolation failed?	32
3.2 Control at the <i>meso</i> scale	37
3.3 Conclusion	40
II Insulating fillers	41
4 meso macro relationships	47
4.1 Introduction	48
4.2 Case of isopotential particles	48
4.3 Case of non - isopotential particles	51
4.4 Conclusion	52
5 Process/structure/HV property	57
5.1 Introduction	58
5.2 Influence of the processing on completion of curing	59
5.3 Influence of the micro and meso scales on high voltage properties	65

6 Physical and Chemical aging	77
6.1 Structural changes induced by aging	78
6.2 Consequences on high voltage properties	88
7 Research projects	99
7.1 Aging of fuel cells	100
7.2 Modeling of the mechanical properties	101
7.3 New characterization device for electrical and mechanical properties	101
7.4 Energy density	102
Lists & references	111
List of Figures	111
List of Tables	113
References	125

Introduction

My research interests are primarily focused on the effect of filler particles and other heterogeneities on polymers.

I have worked on many projects, but there are several things that they all had in common. First, nearly all projects involved searching for the structural parameters that governed the macroscopic properties of the polymers and composite materials. A second common denominator is that even though my work was performed in an “academic context”, the goals were targeted toward industrial needs. Lastly, the methods and procedures were similar; they were all based on experimental results obtained for various scales of measurement (see Fig. 1).

Hence, multi-scale modeling was very useful and beneficial for these projects. The models developed (mainly numerical and sometimes analytical) were initially derived from experimental evidence and then validated and improved with further experimentation. The refined models provided an efficient means of: (i) optimizing the composites according to specific needs, (ii) better understanding the hierarchical relations between the different scales, (iii) controlling the micro or meso structure and thereby the macroscopic properties.

This study of the relations between structure and properties was performed on a wide variety of physical properties and materials. However, the electric and dielectric properties of composites constituted the majority of it and will be presented in this report. The remaining property investigations provided supplemental but valuable information. This work often requires altering various conventional experimental techniques or using well-known techniques for new purposes. I also developed, when needed, several unconventional but necessary measurement techniques.

This report contains two major parts which are separated according to the nature of the fillers:

Part I : Conducting fillers. In the first part, the main interest both for application and fundamental point of view, is related to the changes in properties in the vicinity of the sharp percolation transition. After a brief introduction to the percolation theory, this part will be subdivided in three chapters:

Chapter 1. presents a numerical method that correlates the mesostructure to the macroscopic electrical properties both in two and three dimensions.

Chapter 2. will show that an external variable (the mechanical stress) may largely alter the microstructure of the percolating network within composites as revealed the macroscopic conductivity. The understanding of the mesoscale changes will be based on the chemical structure of the polymer matrix.

Chapter 3. is devoted to the description of a unique case in term of percolation behavior, which made possible the control of the phase arrangement within the composite and thereby the control of the macroscopic resistivity.

Part II : Insulating fillers. In the second part, the main interest is to obtain good electrical insulators, *i.e.* that can withstand large electric fields. This part thus starts with a brief introduction to the common failure mechanisms, associated with the dielectric breakdown and is also divided in three chapters:

Chapter 4. is devoted to the description of a numerical simulation of the relationships between mesostructure and dielectric breakdown.

Chapter 5. reveals the influence of the processing conditions of a composite utilized in the industry on the microstructure and the quantitative consequences on breakdown properties.

Chapter 6. presents the aging of these composites under “real word” conditions which will further be compared to accelerated aging performed in controlled conditions, in the laboratory. A comparison of the two aging situations will furnish a quantitative understanding of the relative influence of the chemical and physical contributions to the aging process.

This report will then be concluded with a description of the current and future projects.

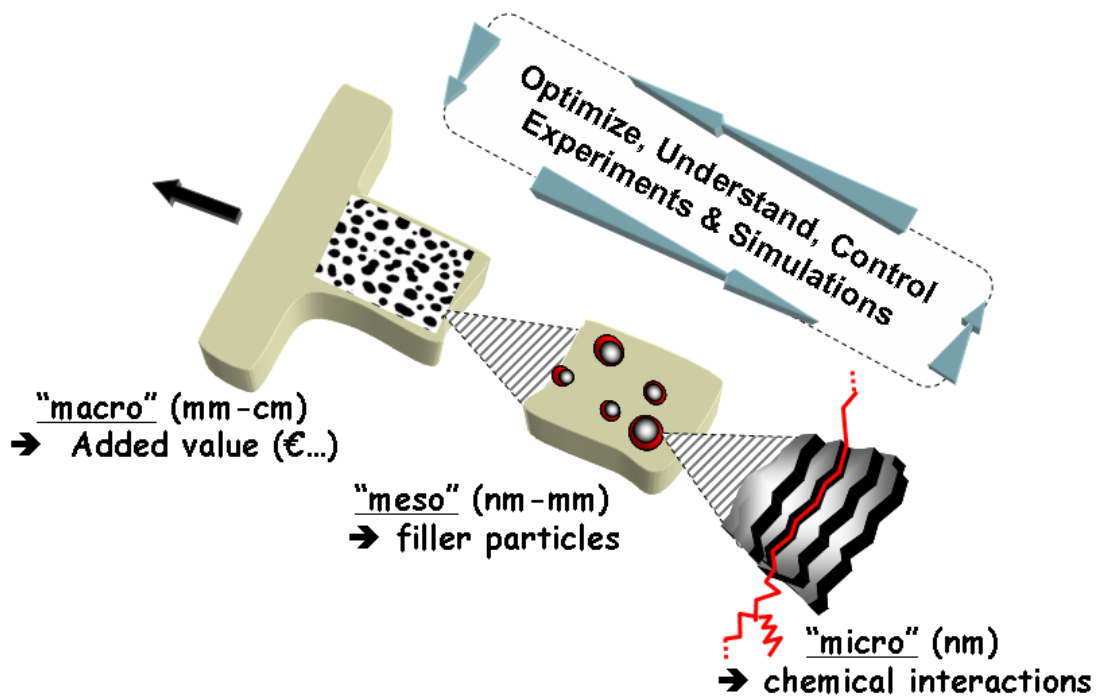


Figure 1 : The “multi-scale approach”: definition of the main three scales utilized in the manuscript: 1- macroscopic scale, essentially that of the final product, 2- mesoscopic scale, corresponding to the size of the *biggest heterogeneities* *i.e.* the fillers in the present case, and 3- microscopic scale, that of chemical interactions. This figure was developed with Prof. Patrice Mélé for the [Master’s lectures](#). This was largely inspired by Fig. 9 in publication (1)

Part I

Conducting fillers

Macroscopic point of view of the percolation process

Introduction²

Polymers contain a very low concentration of free charge carriers, and are therefore generally good electrical insulators (see part 2, page 43). However, conducting plastics or thermosets are useful for many applications⁽⁶⁾. Electrical conductivity can be achieved by incorporation of highly conductive fillers, such as carbon-black (CB) particles, carbon fibers, metallic fillers, or intrinsically conducting polymers⁽⁶⁾.

The transition from an “insulating” to a “conducting” state in a composite by gradually adding fillers to a polymer is brutal, mainly because of the huge difference in electrical conductivity between the two phases (generally more than 10 orders of magnitude). This sudden transition^(2;3;5) in the macroscopic properties of a composite (most often the electrical conductivity, but many other quantities may be concerned) defines, for a given system, a critical volume fraction of fillers called the percolation threshold ; the related transition is named the percolation transition.

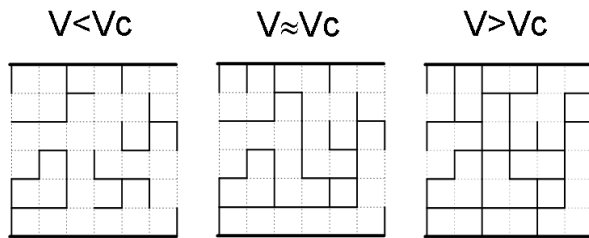


Figure 2 : The three basic connectivity states on a network as a function of the number of active bonds.

The introduction of the percolation concept is generally credited to Broadbent and Hammersley for their pioneering work⁽⁷⁾, published in 1957. The most

²this description is brief and only aims at giving the basic concepts, the reader interested in more details should refer to the numerous books^(2;3) and review^(4;5) on the topic.

prominent⁽⁴⁾ mathematical description of the transition is the statistical percolation model, first proposed by Kirkpatrick⁽⁸⁾. The aim of the statistical percolation theory is to predict the behavior of a non-completely connected set of objects. By varying the number of connections, this model describes the transition from a local to an infinite “communication” state, Fig.2. “Statistical percolation” assumes that the fillers are not interacting with each other or, in other words, that they are randomly dispersed within the matrix⁽³⁾. Under such condition a binary mixture can be modeled⁽⁸⁾ with a lattice possessing a given fraction of active sites (or bonds) randomly chosen, *i.e.* independently of the occupation status of their neighbors. Sufficiently close to the transition, the statistical percolation predicts a power law variation for any relevant quantity with the volume fraction of fillers.

The statistical percolation model can be used to determine variations in both geometric and physical quantities in the vicinity of the percolation threshold. Among geometric quantities, the correlation length occupies a very important place. The correlation length is defined as the average distance between two sites belonging to the same cluster³. It is directly related to the cluster formation and reaches very high values on both sides of the transition. Close to the threshold this parameter follows a power law divergence⁽³⁾: $\xi = |V - V_c|^{-\nu}$, with a value of 0.88 for ν in three-dimensional systems. In the statistical percolation theory the divergence of the correlation length or, in other words, the formation of an infinite cluster, is not due to any agglomeration, which should involve a driving force and a diffusion process, but to an increasing amount of randomly placed occupied sites.

The main macroscopic quantities, namely dielectric constant (ϵ) and dc electrical conductivity (σ), also

³One can in a first approximation consider that ξ is the size of the largest clusters for a given configuration.

exhibit a power law dependence close to the percolation threshold^(9;10):

$$\varepsilon \propto |V - V_c|^{-s} \quad (1)$$

and, for $V > V_c$:

$$\sigma \propto |V - V_c|^t \quad (2)$$

The exponents s and t , characterizing the transition, are assumed to be universal *i.e.* to *only* depend upon the dimensionality of the system, see Table. 1. In three-dimensional systems the universal values are $t \approx 2$ and $s \approx 0.7$ for the conductivity and for the dielectric constant, respectively⁽¹¹⁾. Experimentally both universal and non universal values have been reported⁽¹²⁾ for the exponent t , Fig. 3.

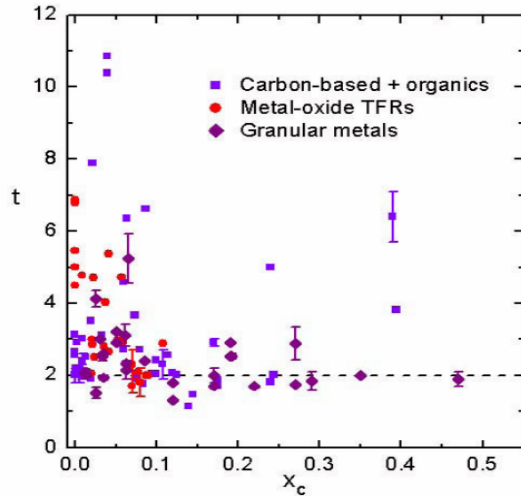


Figure 3 : Collection of critical exponent values t and corresponding critical threshold concentration x_c for various disordered conductor-insulator composites. The dashed line denotes the universal value $t \approx 2.0$, from Vionnet-Menot *et al.*⁽¹³⁾.

Experimental data reported^(14;15;16), for the exponent s are generally in agreement with Eq. 2, although a controversy exist on the latter^(17;18;19;20) and references therein.

Counterintuitive features on percolation

The percolation transition is a mature theory that is used in many area of research. Reading many papers on this subject, one may however notice that four basic features remain somewhat poorly understood.

	Cond.	exp.	div.	1D	2D	3D
P	$p > p_c$	β	$(p - p_c)^{-\beta}$	0	5/36	0.4
S	$\forall p$	γ	$ p - p_c ^{-\gamma}$	0	48/18	1.8
G	$\forall p$	α	$ p - p_c ^{2-\alpha}$	0	-2/3	-0.6
ξ	$\forall p$	ν	$ p - p_c ^{-\nu}$	0	4/3	0.89
ε	$\forall p$	s	$ p - p_c ^{-\beta}$	1	1.35	≈ 0.7
σ	$p > p_c$	t	$(p - p_c)^t$	0	5/36	≈ 2
ρ	$p > p_c$	t	$(p - p_c)^{-t}$	0	5/36	≈ 2

Table 1 : Collection of Universal exponents describing the percolation transition, in the vicinity of the percolation threshold. Geometrical quantities (P : strength of the percolating network, S : average size of finite clusters, G : number of finite clusters and ξ : correlation length). Physical quantities (ε : permittivity, σ : conductivity [$S.m^{-1}$], ρ : resistivity [$\Omega.m$]).

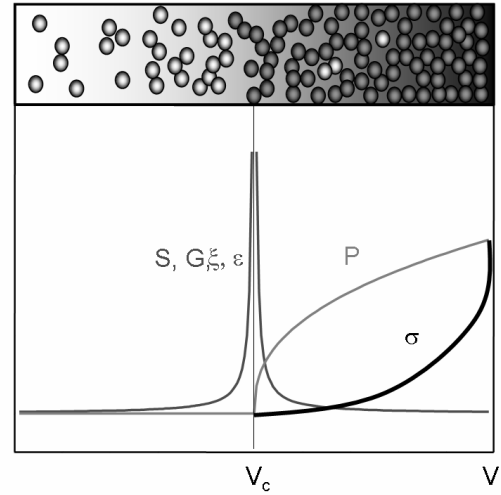


Figure 4 : Summarized representation of the percolation process. The geometrical and physical quantities are presented on linear arbitrary scales.

The first one concerns the experimental determination of the critical exponents, the second one concern the actual reason for the divergence in permittivity, the third one is related to the finite size effect on the percolation threshold and the fourth one is related to the concept of “universality”.

1- The exponents...

The critical exponents are named like this because they describe the behavior or the physical quantities around a critical transition. It can also be thought that their name came from the fact that they “critique” the strength of the transition.

An example of dc conductivity measurements, at

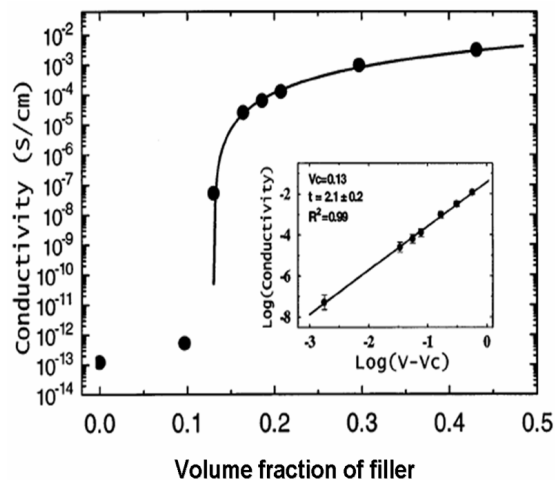


Figure 5 : dc electrical conductivity as a function of filler content (case of spherical filler) and comparison with percolation theory [Source: (21)] .

room temperature, is plotted in Fig. 5. Using a least-squares fit (solid lines), the conductivity exponent t and the percolation threshold V_c of Eq. 2 can be determined.

This method seems so straightforward that the uncertainties on the values are regularly not mentioned in the literature⁴. It is, however, rather well-accepted that the absolute value for the percolation threshold strongly depends on processing conditions. Indeed, if one wants to create an “infinite” cluster, one has to consider the interactions between the fillers. By the way, “do interactions raise or lower the percolation threshold?”. An excellent paper on the subject from Bug *et al.*(22), would actually convince anyone that there is no answer to the “simple” question. The Chapter 3, page 31 of the current report will also be devoted to this question.

In addition, the value of the percolation threshold, much like any experimental value, can not be determined with an infinite precision. As a result, the insert in Fig. 5 can hardly⁵ be lower than few 10^{-3} . One can indeed not get closer to a given value than the error on it. Getting $V - V_c \approx 10^{-3}$ already means that V_c is known at 0.5×10^{-4} .

Even though the absolute value for V_c does not have a physical meaning, it is quite important because it

⁴You may think this is not specific to the critical exponents, you may even be right about it.

⁵Here I have to quote fruitful discussions with Jérôme Fournier who actually was the first, when we were grad. students, to clearly point out this notion of “distance to V_c ”.

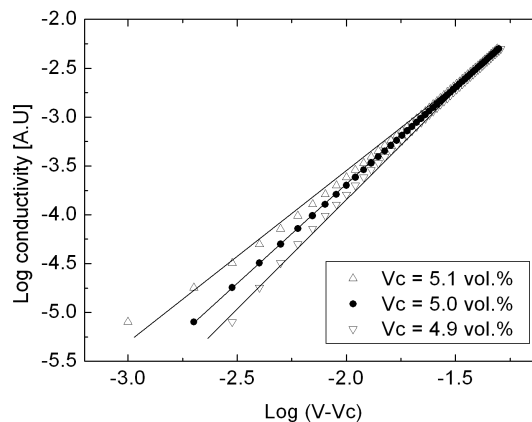


Figure 6 : Sensibility of the percolation threshold on the determination of the critical exponent. Slightly varying V_c , t varied from 1.76 ± 0.02 to $2 \pm 2 \times 10^{-10}$ to 2.18 ± 0.02 . Note that the quality of the fit is not much affected by the changes in V_c .

strongly alters the values of the “universal” critical exponents. On Fig. 6 an example is given with a series of virtual experimental results. It was first assumed a percolation threshold of 5 vol% with an exponent of exactly 2. By changing the percolation threshold by only 2%, the exponents varied from 1.7 to 2.2. This may explain why several values in the literature were reported for the universal exponent t (generally $t = 1.7$ and $t = 2$). This is obviously not the case for the geometrical values that can not be determined experimentally.

2- Divergence of the permittivity

As described above, the exponent s is still the subject to a controversy. It was even claimed -it is hard to deny we even were among the firsts(23)- that the permittivity does not even diverge in the vicinity of the percolation threshold. Because of the very “sharp” expected divergence for the permittivity (the critical exponent should be 0.7) , clearly verifying this would require to develop a series of especially designed samples for which the percolation threshold is very accurately known and that present very reproducible behavior.

Here again there is a very strong experimental issue, related to the fact that above the percolation threshold $\tan \delta$ becomes very close to zero at low frequency and the permittivity is virtually impossible to determine accurately.

One should however bear in mind that, although this point presents few experimental evidence, the theory does give very strong reasons for the divergence of the permittivity in the vicinity of the percolation threshold. Let's consider the well-known expression for the capacity :

$$C = \varepsilon_0 \varepsilon_r \frac{A}{L_0}$$

where ε_0 is the vacuum permittivity and ε_r the relative permittivity of the material, A the Area and L_0 the thickness of the capacitors.

As depicted in Fig. 7, increase the correlation length induces an apparent decrease the value of L_0 . As a result, for a constant intrinsic ε_r , the capacitance value diverges, which leads to the divergence of the apparent permittivity.

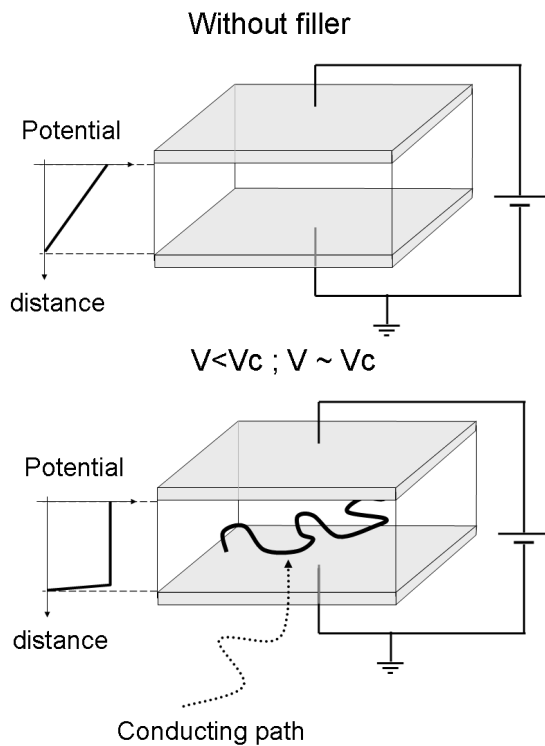


Figure 7 : Simple geometrical explanation for the divergence of the permittivity observed close but below the percolation threshold

3- Size effect?

Another counterintuitive feature concerns the finite size effect on the percolation threshold. It seems rather natural to say that decrease the size of the

“sample”, either on numerical (see Fig. 8) or real experiments would decrease the percolation threshold. There is even a *wrong* explanation to this : “*the correlation length does not depend on the size of the box, so if I decrease the size of the sample it may be lower than the correlation length, therefore the percolation threshold will be reached for lower volume fractions*”. This “demonstration” hides the fact that a sample with a size below the percolation threshold can not be representative of the statistical system. As a result anything can be found for the percolation threshold and the error will be high. Increasing the size of the sample actually reduces the error on V_c without changing the average value Fig. 8. In conclusion, the statement “*the percolation threshold is lower than expected because the samples were not big enough*” is wrong twice, once because the size of the sample does not affect V_c and a second time because there is generally not much to expect from the absolute value of V_c ⁶

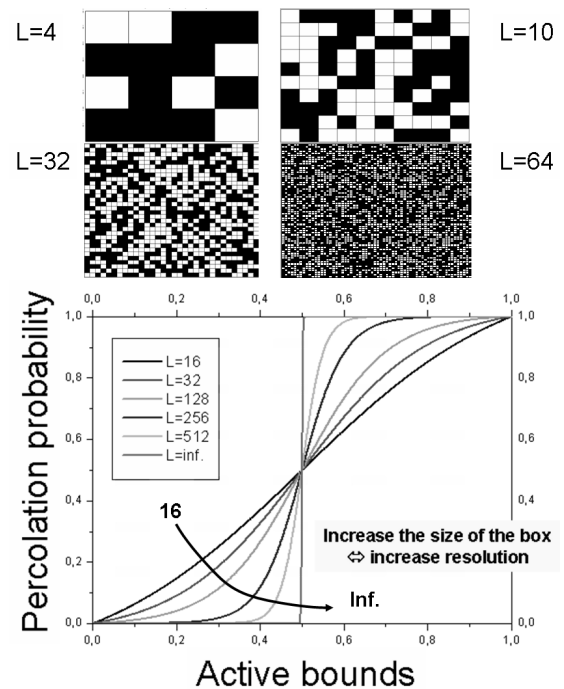


Figure 8 : The percolation threshold does not depend on the size of the box, however increasing the size of the system reduces the error on the estimation of V_c .

⁶Within a given series of similar samples a comparison of the V_c may be interesting. In some cases -short fiber, etc.- one can actually “understand” the value of V_c .

4- Principle of universality

There are two basic assumptions in the principle of universality. The first one is geometric : the fillers are randomly dispersed within the matrix. The second one relates to the conduction mechanisms between the fillers. It thus can be summarized as follow:

$$\begin{array}{l} \text{Random dispersion of the fillers} \\ + \text{ No "tricks"}^\circ \text{ with the conduction mechanisms} \\ \Rightarrow \frac{\quad}{\text{the exponent } t \approx 2} \end{array}$$

◦The main thing that can go wrong is a non Ohmic behavior, as revealed by current-voltage characteristics. The temperature dependence can be useful as well to identify the nature of the conduction mechanisms.

This "equation" does oversimplify the problem and could never be published or would be the subject of a strong controversy. It can however be considered as a starting point one should keep in mind, to prevent things like "*This is a universal behavior with a different exponent*", or "*In the case of a universal behavior, the values for the critical exponents depend on the nature of the sample (network or continuum)*".

Chapter 1

A numerical approach of the meso-macro relationships

⊙ **Abstract** ⊙

The relation between microstructure and electrical properties of polymer reinforced by electrically conducting nanofibers is investigated using a RC type simulation. Real and imaginary parts of the conductivity vs. the frequency and the filler fraction are presented both for two- and three-dimensional systems. In the latter case, resistors and capacitors values are deduced from a random microstructure and the measured macroscopic properties of each component. These results are compared with experimental data obtained on a nanocomposite material composed of electrically conductive fillers dispersed in an insulating matrix.

Contents

1.1	Introduction	12
1.2	2D systems	12
1.2.1	Definition (2D)	12
1.2.2	Results (2D)	13
1.3	3D systems	14
1.3.1	Generation of a Random Composite	14
1.3.2	Equivalent RC Circuit	15
1.3.3	Resolution of the Network	16
1.3.4	Results on the Random Microstructures	17
1.4	Conclusion	20

1.1 Introduction

The first publication concerning simulation of the conductivity of insulator-conductor networks was reported in 1973 by Kirpatrick.⁽⁸⁾ As already mentioned this work lead to the first values for the critical exponents. Since this pioneering work, the numerical methods have been considerably improved, especially for the understanding of the ac response,⁽⁹⁾ that contains much more information than the static one. In particular, the RC model (*RC* stands for Resistor, Capacitor) has been developed to explain the frequency dependence of the complex conductivity. Basically, this model describes the electrical properties of the composites with an appropriate choice of bond conductance on a given network. The contact between particles is identified with resistors while the capacitors model either the inter cluster polarization⁽⁹⁾ or the anomalous diffusion within clusters⁽²⁴⁾. Improvement of this RC model, namely R-RC^(9;25;26;27;28), and RLC⁽²⁹⁾ models, have also been proposed to correlate the optical properties of conductor- insulator mixtures with the local conduction mechanisms. For example, Clerc *et al.*⁽²⁶⁾, showed that resonant phenomenon in the optical properties of composites can be accounted for by numerical simulations using an RLC model, Fig. 1.1.

As already mentioned, these simulations were developed on incompletely connected networks in which the bonds (or sites) are active with a given probability. Changes in both real and imaginary parts of the conductivity can be related to changes in morphological properties of the composite. Thus, the sharp

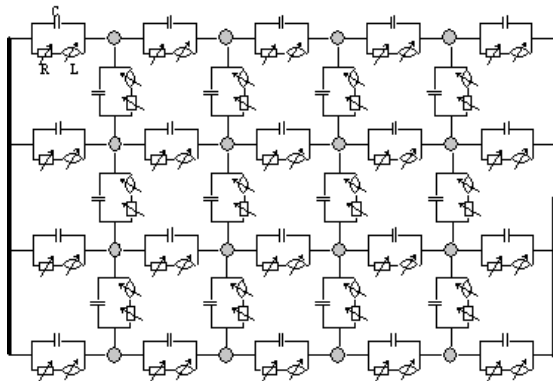


Figure 1.1 : Numerical simulations on a square lattice of links. All sites are occupied by conducting grains. The links bold a distribution of resonant circuits, from Clerc *et al.*⁽²⁶⁾.

increase in the dc conductivity is related to the increasing number of paths created on the network by increasing the probability of the random occupation. The divergence in the relative permittivity is correlated to the divergence in the correlation length.

Nevertheless, many parameters may influence the final microstructure of heterogeneous composites,⁽⁴⁾ thereby influencing the electrical properties. The geometrical properties of binary mixtures have also been simulated, mainly to determine the influence of particle interactions⁽³⁰⁾ orientation⁽³¹⁾ or aspect ratio^(32;33;34;35) on the value of the percolation threshold.

Several solutions have been proposed in the case of diluted systems.⁽³³⁾ It was also of interest to develop a numerical simulation that combines geometrical and electrical properties or that, in other words, relates the macroscopic electrical properties of composites with their meso structures.

The processing of polymer-based composites consisting of an insulating matrix and conducting polypyrrole fillers used in the present study was described in^(21;36;37;38). Fillers with a high aspect ratio (close to 15) were obtained through the polymerization of polypyrrole onto the surface of cellulose whiskers. The materials were prepared by mixing aqueous suspensions of conducting and insulating polymers. The suspensions were freeze dried and compression molded to obtain homogeneous films having different filler contents. The fillers were dispersed within the matrix with a random position and orientation and these composites qualified to validate the numerical simulation.

1.2 2D systems

1.2.1 Definition (2D)

For the 2D simulation, both square networks and random Voronoi tessellation were utilized, Fig. 1.2. The Voronoi diagrams were obtained with help of the *Triangle*^(40;41) software. A network was built, with a fraction p of randomly positioned active edges substituted in a *RC* circuit by resistors, while the nonactive edges were replaced by capacitors. Resistors and capacitors values are usually, in the RC model, chosen either to be constant or to follow a given statistical distribution -Gaussian, etc-. In the present approach, their value were meant to reflect the local geometry.

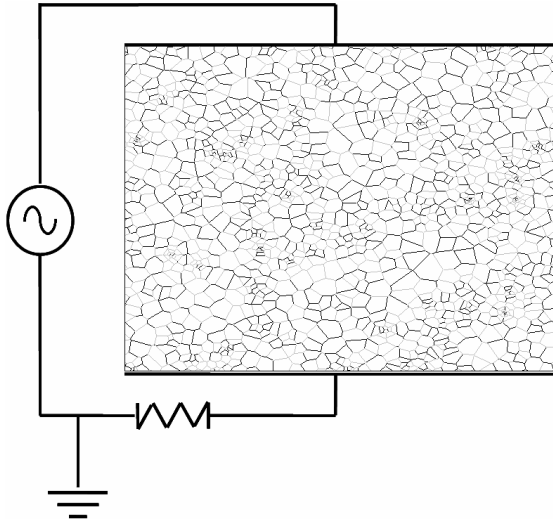


Figure 1.2 : 2D random tessellation with Voronoi polygons (1000 edges). This graph was obtained with a probability of active bounds p equal to 0.6. Black segments represent active bounds (resistors) and the gray links represent non-active bounds (capacitors). Schematic representation of the electrodes, the voltage source, and the current measurement resistor [Source: (39)] .

Thus, by defining the distance between two nodes i and j as D_{ij} , the values of the resistors were calculated from:

$$R_{ij} = \rho_l * D_{ij} \quad (1.1)$$

where ρ_l is the linear resistivity of the active edges. The values of the capacitors are governed by:

$$C_{ij} = K/D_{ij} \quad (1.2)$$

where K is a second adjustable parameter, related to the dielectric properties of the matrix. However, as already outlined,⁽²⁵⁾ the parameters ρ_l and K are difficult to compare with any measurable quantity (this point will be further discussed in the section concerning the 3D simulation).

As schematically depicted in Fig. 1.2, different measurement elements were placed in the network, namely: (i) two electrodes on two opposite sides, (ii) a tension source between the ground and one electrode, and (iii) a known resistor (called measurement resistor) between the ground and the other electrode. The electrodes consist of resistors with a very low values ($10^{-15}\Omega$) between the edges crossing the top edges on the one side and the bottom edges on the other side. The tension source was a sine wave voltage of 10V in amplitude in a frequency range from 10 Hz

to 1 MHz. The measurement resistance was chosen with a value of $10^8 \Omega$. The output of the computation was a complex voltage V_{out}^* determined across the measurement resistance (R_{meas}). Defining V_{in} as the applied voltage, the admittance Y^* of the simulated composite is governed by:

$$\frac{1}{Y^*} = R_{meas} \left(\frac{V_{in}}{V_{out}} - 1 \right) \quad (1.3)$$

The RC circuits were solved with the help of “Spice 3f5” software^(42;43), developed at the University of California, Berkeley.

1.2.2 Results (2D)

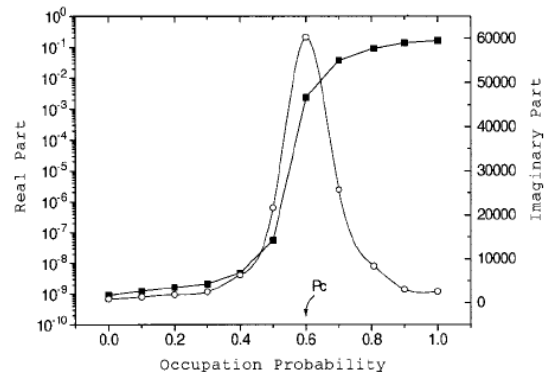


Figure 1.3 : Real (■) and imaginary (O) parts of the conductivity at 1 kHz vs. occupation probability for a 2D Voronoi tessellation [Source: (39)] .

Simulations were performed with lattices containing about 10^4 edges, with different fractions of active bonds. Fig. 1.3 displays the evolution of the real and imaginary part of the conductivity for a 2D Voronoi network as a function of the active bounds. The results agreed well with the prediction of the percolation theory. In particular, the real part of the conductivity was found to remain almost constant up to an active bond fraction close to 0.6. This value for the critical probability is in agreement with the one found on a 2D random Voronoi tessellation of the plane⁽⁴⁴⁾. For higher occupation probability a sharp increase corresponding to the percolation transition is observed. The imaginary part of the conductivity diverged at the percolation threshold, as predicted by the percolation theory. The data obtained for both the real and the imaginary part of the conductivity vs. the filler content were fitted to power law equations. The

	t	s	P_c
Voronoi	1.2 ± 0.2	1.1 ± 0.2	0.62 ± 0.05
Square	1.3 ± 0.2	1.2 ± 0.2	0.5 ± 0.5
Universal 2D	1.3	1.3	—

Table 1.1 : Numerical values for the critical exponents s and t calculated on a 2D random network, and comparison with predictions of the percolation theory [Source: (39)]

critical exponents obtained for 2D Voronoi diagrams and square networks are summarized in Table 1.1.

As expected, the values for these exponents confirmed that the RC model with random occupation of edges is consistent with the statistical percolation theory.^(2,3) The percolation threshold p_c could, however, not easily⁽⁴⁵⁾ be compared with the experimental value, thus limiting the application of this model to real materials. Furthermore, the macroscopic conductivity as well as permittivity depends on adjustable parameters. The local resistors and capacitors which were thus only loosely connected to the real microstructure. To overcome these drawbacks, a more realistic 3D model was developed. The aim is to relate the local R and C values of a RC type model to geometrical features of the 3D reinforcement in the polymer.

1.3 3D systems

The 3D ac electrical properties were determined in three steps, namely (i) the generation of the composite, (ii) the computation of the RC circuit corresponding to this microstructure, and (iii) the network resolution. The model proposed here corresponds to an inter-cluster polarization¹, which assumes that the polarization effect between clusters is responsible for the macroscopic permittivity.

1.3.1 Generation of a Random Composite

The first step involved the definition of random set of N_f fibers in a given volume. All particles were chosen with the same size and placed into a cube (corresponding to the matrix). The volume L^3 of the cube was homothetically adjusted to obtain the desired V_f . The position of each filler i within the cube was defined with five parameters Fig. 1.4-a.

¹Inter-cluster polarization is opposed to the anomalous diffusion model⁽²⁴⁾

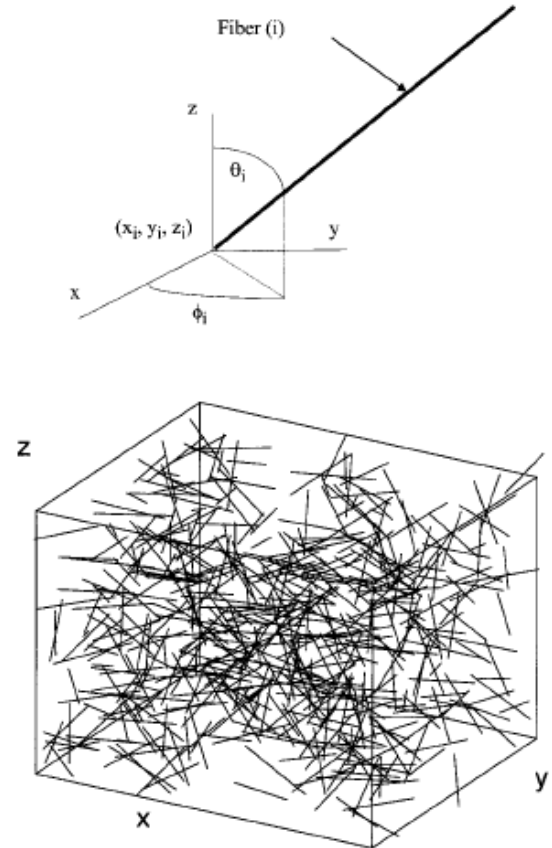


Figure 1.4 : (a) Definition of the short fiber's positions in the cube being modelled, and (b) example of microstructure with 500 elements. Periodic conditions were applied in the Y and Z direction and the conductivity was computed in the X direction. Fibers intersecting the boundary of the cube in the X direction were cut [Source: (39)] .

The first three parameters give the coordinates (x_i, y_i, z_i) of an extremity of the particle and the two other parameters defined ϕ_i and θ_i , the orientation of the fiber. A random and uniform distribution of both the particle's positions and orientation was obtained with (x_i, y_i, z_i) , ϕ_i and $\cos(\theta_i)$ varied randomly and uniformly from 0 to L , 0 to 2π , and -1 to 1, respectively. Periodic boundary conditions were applied in two directions to avoid boundary effects and the electrical properties were measured in the third direction. For this reason, the elements crossing the surface of the cube in the last direction were cut. An example of the final microstructure with 500 elements is displayed in Fig. 1.4. Once the microstructure was set, the corresponding RC circuit could be built in a similar way to that used for the 2D systems (Fig. 1.2).

1.3.2 Equivalent RC Circuit

Basically, the RC circuit is developed on the nodes of a network corresponding to the fibers center of mass. Each filler i is assumed to develop an electrical relationship with its N_n surrounding neighbors. The N_n value was fixed with the help of the average coordination number of the 3D Voronoi tessellation z_s that has been calculated analytically by Meijering⁽⁴⁶⁾ and found to be $z_s = \frac{48}{35}\pi^2 + 2 \cong 15.54$.

The number of the closest neighbors for each particle was therefore set to 16 and the other particles in the matrix were disregarded. The latter assumption corresponds to a statistical screening of the electrical field. Between a pair of closest neighbors (i, j) , either a resistor or a capacitor was added to the circuit, depending on the geometrical contact between these particles, leading to a RC network schematically displayed in Fig. 1.5-b.

The geometrical contact between fibers i and j was modeled by a resistor between nodes i and j . The value for this resistor can be estimated by:

$$R_{ij} = \rho \frac{4 \cdot (L_i + L_j)}{\pi \cdot d^2} \quad (1.4)$$

where L_i and L_j correspond to the lengths of the element i and j , respectively, d is the diameter of the particles, and ρ is the macroscopic resistivity of the filler. Under such conditions, ρ includes the contact resistance between the particles and no adjustable parameter corresponding to the interparticle resistivity

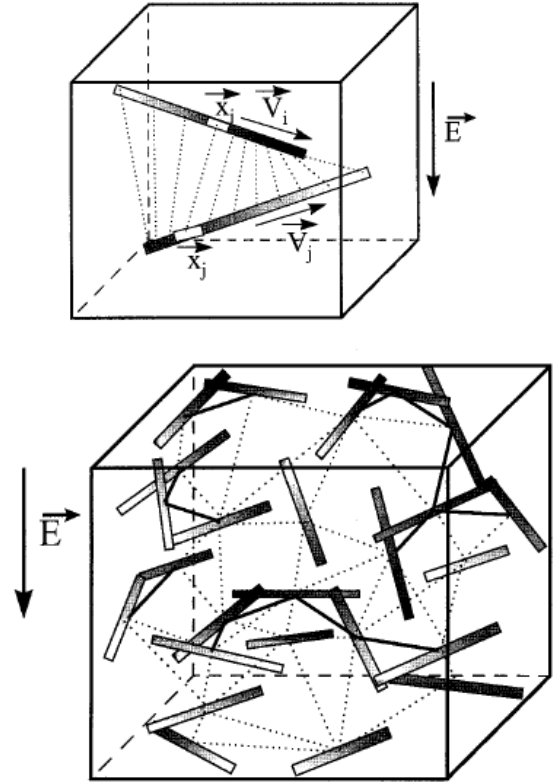


Figure 1.5 : (a) Determination of the equivalent capacitor value: dashed lines represent the assumed field lines, and (b) Schematic representation of the microstructure and equivalent RC circuit. The dashed lines represent the capacity and the solid lines represent the resistors [Source: (39)] .

was added to the simulation. However, Eq. 1.4 assumes the filler always contact to one another at their extremities. This non-realistic assumption could be replaced by a better one that makes a statistical correction for R_{ij} depending on the calculated total number of contacts N_c in the composite. The latter leading to:

$$R_{ij} = \rho \frac{4 \cdot (L_i + L_j)}{\pi \cdot d^2} \cdot \frac{N_f}{N_f + N_c} \quad (1.5)$$

The determination of an “equivalent capacity” between to fillers is much more difficult. When two isolated fillers i and j were not in contact, the mutual capacity had to be estimated. Therefore, the fillers i and j were considered as the “plates” of a capacitor. Gauss theorem states that the net flux out of a closed surface is equal to the enclosed charge divided by the permittivity of the medium. This can be applied to determine the electrical charge $Q_{enclosed}$, for two plates separated by a dielectric medium with a permittivity $\varepsilon = \varepsilon_0 \varepsilon_r$. The flux of the electrical field on Σ , a closed surface containing a plate, is:

$$\oint_{\Sigma} \vec{E} \cdot d\vec{A} = \frac{Q_{enclosed}}{\varepsilon_0 \varepsilon_r} \quad (1.6)$$

where ε_0 is the vacuum permittivity and ε_r the relative permittivity of the material. In the case of parallel plates, the electrical field is equal to the ratio between the applied voltage U and the distance between the plates L_0 . Using the definition for the capacity $C = Q/U$ and Eq. 1.6, one finds the well-known expression for the capacity :

$$C = \varepsilon_0 \varepsilon_r \frac{A}{L_0}$$

However, when the plates are rods that are neither parallel to one another nor perpendicular to the macroscopic electric field, the capacity between the elements is unknown. Furthermore, the lines of the electric field are unknown and one cannot easily apply Eq. 1.6. Thus, to estimate the value for each capacitor one has to make an assumption on the local electric field. The most realistic way seemed to assume that the electric field lines are segments on the ruled surface including the two rods and parallel to the common perpendicular to the two rods, Fig. 1.5(a). The value for the capacity was computed with the Gauss’ theorem for a small element in the plate, where the

electrical field is constant. The total capacity is consequently a finite sum of capacities associated in parallel. Thus, if one calls $\vec{x}_i(k)$ and $\vec{x}_j(k)$ the vectors of the elements i and j corresponding to the line field k , \vec{n}_k and \vec{v} the unit vectors describing the local electrical line field and the filler orientation, respectively, and $\Delta = L_i/N$ is the length of a local capacity, the total capacity value is equal to:

$$C_{ij} = \varepsilon_0 \varepsilon_r \sum_{k=1}^{n_s} \frac{d \cdot \Delta \cdot \left\| \vec{u} \otimes \vec{V}_i \right\| \cdot \left\| \vec{u} \otimes \vec{V}_j \right\|}{\left| \vec{x}_i(k) - \vec{x}_j(k) \right| - d} \quad (1.7)$$

where the product $d \cdot \Delta$ is the surface of an elementary capacitor. The vector product accounts for the orientation of the filler in the local field, while the denominator gives the distance between the elementary surfaces. This distance cannot become negative because the particles do not overlap in this the case (when two particles do overlap this calculation is not performed and a resistor is inserted in the equivalent circuit). Eq. 1.7 for the capacity, in comparison to the classical expression, presents the advantages of including the relative positions and orientations of the particles. It corresponds to a dipolar approximation and to a linear dependence of the ac response with the electric field, suitable for electric field with low intensity and frequency.

1.3.3 Resolution of the Network

The 3D simulation permitted the introduction of a real physical scale in the simulated composite and thereby permitted the determination of its intrinsic electrical properties. Thus, the admittance was calculated, like for the 2D version, using Eq. 1.3 and the intrinsic conductivity σ^* was obtained with:

$$\sigma^* = Y^*/L \quad (1.8)$$

where L is the size of the cube defined above. As already mentioned, to allow a quantitative comparison between the experimental and simulated results, the values of resistors and the capacitors introduced in the network are directly related to the macroscopic properties of each components. Thus, both parameters ε_r and ρ in Eqs. 1.5 and 1.7 were measured, with conductive fillers prepared in the same manner as the

composite films and for a film free of filler, respectively. The parameters were found to be $\rho = 0.1\Omega.m$ and $\varepsilon_r = 2.1$.

It is interesting to determine the order of magnitude for the resistors and capacitors in our composite. The fillers were $2\mu m$ in length and $140nm$ in diameter. The use of Eqs. 1.5 and 1.7 gives $R \cong 10^7\Omega$ and $C \cong 10^{-18}F$, which gives a ratio $R/C \cong 10^{25}$ which was a far too high a value and caused computational problems. Nevertheless, a linear “change” of the size of the particles (for instance from $1\mu m$ to $1m$) decreases the resistor’s values ($R \cong 10^1\Omega$) and an increase in the capacitor’s values ($C \cong 10^{-12}F$) without any change in $RC \cong 10^{-11}s^{-1}$. We verified that the final results for the macroscopic conductivity, in S/cm, remained constant with such a scale change and it was applied in the rest of the calculations². The decrease in the R/C ratio to 10^{13} reduced the CPU needs and the numerical uncertainties.

1.3.4 Results on the Random Microstructures

The following section summarizes the results of conductivity simulations based on the described model. The output from the simulation, with a constant number of 4000 elements but for different filler contents was compared with experimental data. The correlation length ξ represents the pertinent scale for the investigations of disordered media⁽³⁾. Close to the percolation threshold, ξ is governed by $\xi = \xi_0 |V - V_c|^{-\nu}$ with $\nu \cong 0.88$. Thus, to avoid finite size effect, the simulations were performed for $|V - V_c| > 10^{-2}$. Under such condition the correlation length was always lower than $10\mu m$, Fig. 1.6, whereas the size of the cube was greater than $20\mu m$.

1.3.4.1 Macroscopic point of view

The simulated geometrical percolation threshold V_c was first evaluated by dichotomy on five different samples and found to be $4.45 \pm 0.05\%$. This value slightly differs from the experimental of $3.0 \pm 0.05\%$. The difference between these values could be related to the distribution in filler length in the real material that is not accounted for in the simulation. Due to the large aspect ratio of the conducting fillers, this threshold is

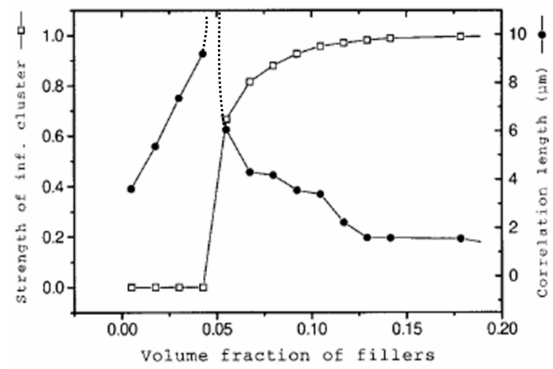


Figure 1.6 : Calculated geometric parameters: correlation length ξ (●) and strength of the infinite network P (□) vs. the filler content [Source: (39)] .

however much lower than that of 16% typically obtained for spherical fillers in both cases. The morphological quantities ξ and P were computed for different volume fraction V_f . By definition, the strength of the infinite network remained equal to zero up to V_c . P then followed a power law evolution. The correlation length diverged in the vicinity of V_c both for volume fraction slightly above and below the critical value. Even if for such a “small” network one should not expect a perfect agreement with the theory³, the simulation results agreed qualitatively well with the behavior expected for random infinite samples, Fig. 1.6. Moreover, the results were not sensitive to the size of the box, as long as the latter is representative from the heterogeneity of the binary mixture.

The real (σ') and imaginary (σ'') part of the conductivity at low frequency vs. the filler content were computed and depicted on a logarithm scale in Fig. 1.7(b). For comparison the experimental data were plotted with the same scale, 1.5(a). From these graphs, it is clear that the simulation describes accurately both (σ') and (σ'') of real materials. In particular, this RC model gave values rather comparable with the experimental data, except for the critical exponent “ t ” found to be equal to 3 in the experimental case whereas the simulation gave a value of 2.4. This difference can be explained on the one hand by the relative small size of the simulated composite that prevented the simulation from closely approaching the percolation threshold with representative samples. The difference could also be explained by assum-

²Eq. 1.8 must obviously also take into account the scale change.

³ the percolation threshold could not be approached sufficiently close with a representative sample.

ing other conduction mechanisms as, for instance, interparticle tunneling⁽¹³⁾, or whenever a distribution of conductance exists⁽⁴⁷⁾.

1.3.4.2 meso macro relationships

The local values of the resistor and capacitor are related to the geometrical arrangement of the fillers, it is thus worth investigating the evolution of the average value of these quantities while V_f increases and to compare it with the evolution of their macroscopic counterparts. Below the percolation threshold, no continuous path of resistor may be found in the RC network but the increase in the correlation length, corresponding to the development of the new contacts between fillers, lead to a large increase of the relative permittivity. Thus, while V_f varied from 0.5 to 4.5%, the average value of the local capacitor C_{ij} as defined in Eq. 1.7 varied from 3×10^{-19} to $7 \times 10^{-19} F$. The relative permittivity, on the contrary, varied from 5 to about 250. This shows that the divergence of the permittivity in the vicinity of the percolation cannot be related to local mechanisms but has to be considered as a cooperative effect. Above the threshold an important increase in σ' is related to the increase in the number of conducting paths through the simulated material. For a variation of V_f from 4.2% to 15%, an evolution of the average local resistor value from 10^8 to $7 \times 10^7 \Omega$ was observed, whereas the conductivity varied from 10^{-6} to $10^{-3} S/cm$. Here again the changes in macroscopic properties were primarily related to cooperative changes rather than to the local changes in modeled variables.

The frequency dependence of the conductivity and of the phase angle were determined in the range $10 Hz$ to $1 MHz$, Fig. 1.8 and 1.9. Here again, the simulation was found to fairly follow the experimental data. For V_f below the percolation threshold, the simulated composite, as well as the real material, exhibited typical dielectric behavior namely a linear increase in the conductivity as a function of frequency, and a phase angle close to $\pi/2$. In this range of volume fraction, the polarization effects that increase with increasing V_f govern the electrical properties. For volume fraction just above the percolation threshold, two mechanisms appeared, depending on the frequency of the applied field. A macroscopic behavior intermediate between a pure resistor and a pure capacitor is observed. While a plateau in the low frequency range corresponded to the electrical response

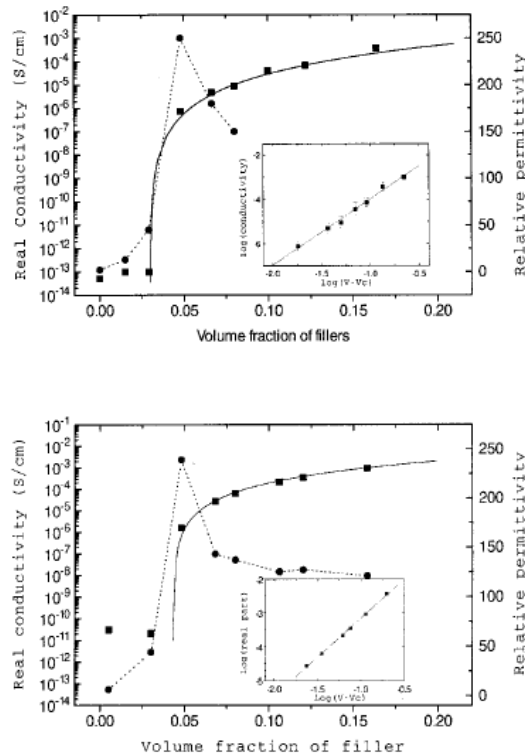


Figure 1.7 : Real part of the conductivity (p) and relative permittivity (\bullet) determined at $1 kHz$ vs. filler content (top) experimental, and (bottom) simulated data [Source:(39)] .

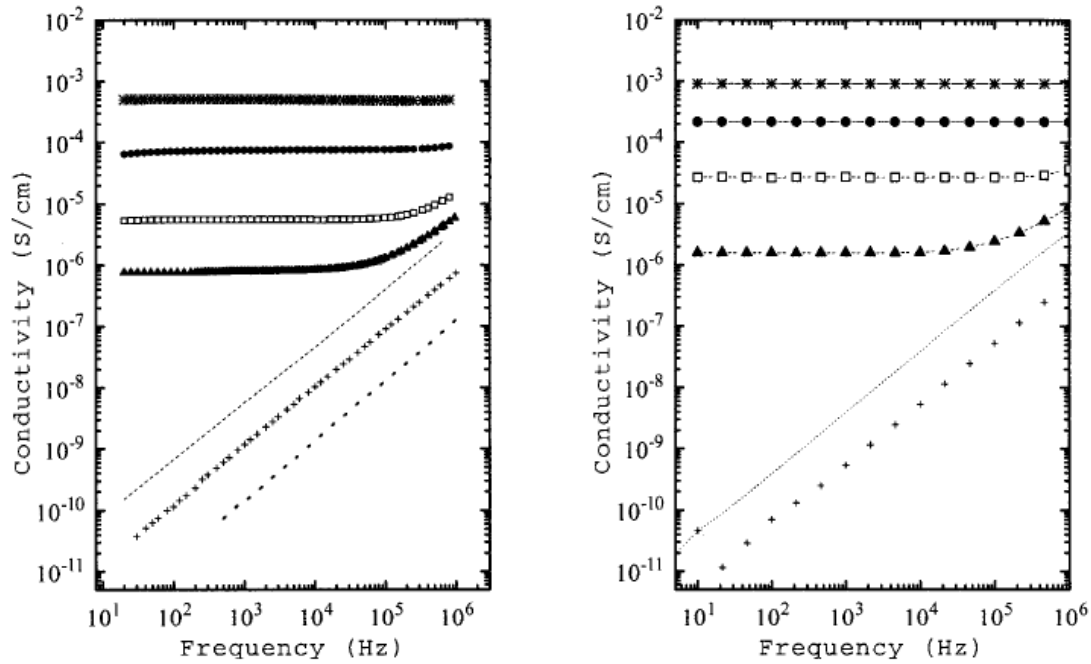


Figure 1.8 : Frequency dependence of the conductivity at room temperature for composites filled with 0 (\cdot), 1.5 (+), 3 (-), 4.8 (▲), 7 (□), 12 (○), and 16vol.% (*): (left) experimental, and (right) simulated data [Source:(39)] .

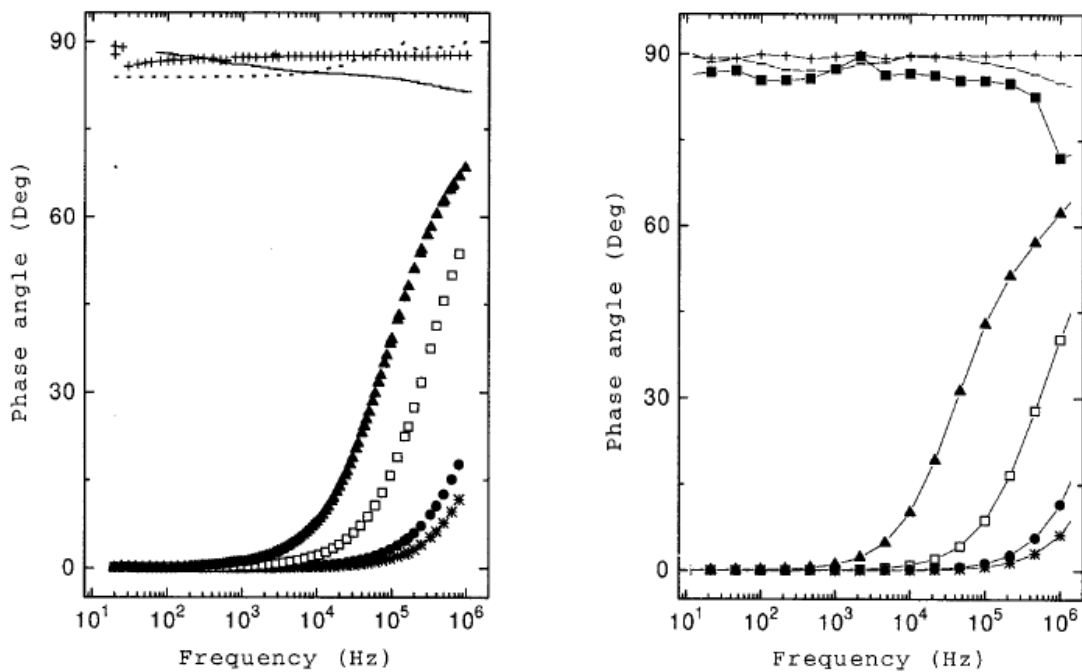


Figure 1.9 : Frequency dependence of the phase angle at room temperature for composites filled with 0 (\cdot), 1.5 (+), 3 (-), 4.8 (▲), 7 (□), 12 (●), and 16vol.% (*): (left) experimental, and (right) simulated data [Source:(39)] .

of the percolating network, the conductivity increased at higher frequencies due to the growing importance of the polarization effects on the macroscopic conductivity. These effects are related to the decrease of the impedance of the local capacitors, with increasing frequency.

Phases angle observed for average volume fractions are consistent with this observation although more accurate, the comparison of (a) and (b) indicated that phase angle began to “take off” from zero values for very similar frequencies both in experiments and simulations. For V_f higher than 20%, the composites exhibited a behavior very close to the one of a pure resistor and the relative permittivity could not be determined accurately with experimental measurement as phase angles were too close to zero.

1.4 Conclusion

The possibility to model a strongly heterogeneous material (from the viewpoint of electrical properties) using an improvement of an RC type model was explored. This model related R and C values to the geometrical characteristics of the network of reinforcing fibers.

The 2-D simulation was in fair agreement with the prediction of the percolation theory. Such a simulation, very flexible, could be further used for the qualitative understanding of the ac properties of binary mixtures. In particular, this method could be coupled with a careful image analysis to determine the changes in electrical properties with the filler content. This approach will in fact be developed in the chapter 4, page 47 of the current report. A 2-D simulation can not, however, give a quantitative description of the percolating network, which intrinsically possesses a 3-D structure.

The 3-D simulation naturally accounts for the structure of the heterogeneous composite. In particular, a good agreement was found between the simulated and experimental percolation thresholds.

Moreover, this work introduced a *physical length in the RC model*, with a simple definition of the resistor and capacitor values.

From the above discussion, the simulation largely succeeded in explaining the experimental data, such as the complex impedance and its frequency dependence. This type of numerical simulation is very useful to understand the relationships between meso scale and

macroscopic properties. Any conduction mechanism as well as a temperature dependence of the conductivity could be added, as long as the local electrical behavior is well defined. The present simulation was also employed to understand the electrical properties of composites during stretching⁽⁴⁸⁾. Recently, this type of simulation was applied to the case of non straight objects⁽⁴⁹⁾.

Chapter 2

Electrical properties: a way to dynamically probe microstructures

⊙ **Abstract** ⊙

The mechanical and dc electrical properties of a carbon black-filled ethylene-octene elastomer (EO) are reported. The stress-strain curves of the composites, scaled with that of the unfilled polymer up to approximately 500% strain, suggest good filler-matrix adhesion. The large reinforcement effect of the filler followed the Guth model for non-spherical particles. Electrical behavior under large strain was divided in four qualitatively or quantitatively different regimes that differentiated carbon black composites with the EO matrix from carbon black composites with chemically vulcanized matrices. Among the most notable features of the EO composites was the completely reversible variation of the resistivity, up to 20% strain, suggesting that these materials might be useful as strain gauges. In addition, depending on the carbon black content, the composites retained low resistivity to high strains. From the results of various thermo-mechanical treatments, a microstructural model for the response to stretching was proposed. This model incorporated dynamic junctions specific to the EO matrix to describe the mechanical properties, the decrease in resistivity at low strains (20%), and the low increase in resistivity at intermediate strains (up to about 400%).

Contents

2.1	Introduction	22
2.2	Materials and methods	22
2.2.1	Materials	22
2.2.2	Methods	23
2.3	Results and discussion	24
2.3.1	Mechanical properties	25
2.3.2	Electrical properties under uniaxial strain	26
2.3.3	Model for EO filled with high-structure carbon black	28
2.4	Conclusion	30

2.1 Introduction

Low-resistivity elastomers typically employ vulcanized rubber as a matrix for dispersion of a large variety of fillers, mainly carbon blacks^(50;51), carbon fibers⁽⁵²⁾ and metallic particles⁽⁵³⁾. In addition to imparting conductivity, the filler generally improves environmental resistance and mechanical properties. As these composites do not always exhibit the best balance of properties, alternative elastomeric matrices are of interest. The development of Dow's INSITE™ constrained geometry catalyst technology has led to the production of a new class of elastomers based on homogeneous ethylene- α -olefin copolymers. In particular, copolymers with more than 8% octene possess low crystallinity and rubber-like behavior that depends on physical rather than chemical junctions⁽⁵⁴⁾, Fig. 2.1.

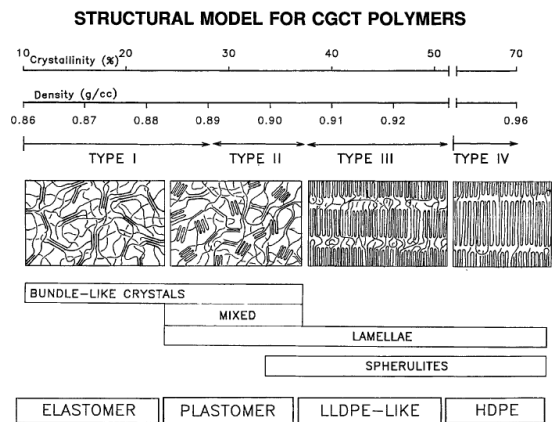


Figure 2.1 : Structural model for ethylene-octene copolymer as a function of comonomer content, from Bensason *et al.*⁽⁵⁴⁾

The main advantage of these polymers over chemically vulcanized elastomers, lies in their ease of processing and post-processing, much like conventional polyethylenes. These elastomeric materials have been commercialized and are the subject of numerous investigations as unfilled polymers^(55;56;57), however very little is known about their mechanical and electrical properties when reinforced with conducting fillers⁽⁵⁸⁾. Electrical properties of binary mixtures depend strongly on the microstructure. In particular, dispersion state⁽²³⁾, filler geometry⁽⁵⁹⁾, and filler-filler⁽²³⁾ and filler-matrix⁽⁶⁰⁾ interactions strongly affect the electrical properties of composite materials. External variables, such as temperature^(61;62) and mechanical stretching^(48;63), can significantly affect

the microstructure and thereby the macroscopic conductivity. If there is a simple relationship between electrical conductivity and an external variable, the composite has potential applications as a sensor. For these reasons, the development of new conductive composites requires an understanding of the changes in conductivity that might occur in service. Conversely, measurement of electrical conductivity under large strain can be a probe to understanding microstructural changes.

Composites that incorporate a conductive filler into an ethylene-octene (EO) elastomer matrix were evaluated for electrical and mechanical properties⁽⁶⁴⁾. Comparing three types of fillers (carbon fiber, high-structure carbon black, and low-structure carbon black), it was found that the composite with high-structure carbon black exhibited some interesting electrical and mechanical characteristics. The present work examines, in more detail, the properties of EO with a high-structure carbon black filler. The mechanical behavior was studied as a function of filler content in order to quantify the reinforcement effect of the particles. However, the work focused primarily on in situ changes of resistivity during uniaxial stretching. Particular attention was paid to the occurrence of reversible and irreversible phenomena. The electrical and mechanical properties were analyzed for the purpose of correlating macroscopic behavior with microstructural events.

2.2 Materials and methods

2.2.1 Materials

An EO elastomer, synthesized by the Dow INSITE™ technology and commercialized under the designation Engage DEG-8180, was the matrix in this study. The polymer had a density of 0.863 g.cm^{-3} and behaved as an elastomer at room temperature⁽⁵⁴⁾, Fig. 2.1. A high-structure carbon black designated as Conductex 975 Ultra was supplied by the Columbian Chemicals Company (particle diameter 21 nm ; dibutyl phthalate absorption number (DBPA) 170; surface area $242 \text{ m}^2.\text{g}^{-1}$; volatiles 1%; mean aggregate size 110 nm ; weight mean aggregate size 300 nm ; average aspect ratio 2.78).

Blending was carried out in a Haake Rheomix 600 mixing head with a 44 cm^3 mixing volume. The polymer was melted in the mixing head for 1 min before

the filler was slowly added. The total operation lasted 10 *min*, during which time the mixing head was maintained at 40 *rpm* and 200°C. All batches, as well as the unfilled elastomer, were processed under identical conditions. After cooling, the blends were compression molded into 2 *mm* thick plaques. The materials were sandwiched between Mylar sheets, heated at 200°C under minimal pressure for 2 *min*, then subjected to repeated pressure-release cycles for 8 *min* to remove any air bubbles resulting from the mixing procedure. Plaques were rapidly cooled to ambient temperature under minimal pressure in a cold molder.

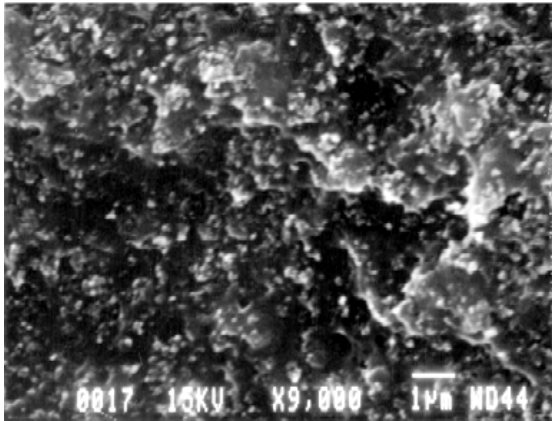


Figure 2.2 : Scanning electron micrograph of a cryofracture surface showing dispersion of the carbon black filler (20% v/v) [Source: (65)] .

To confirm good particle dispersion, specimens were broken in liquid nitrogen, coated with 10 *nm* of gold and observed in a JEOL JXA 840A instrument. Fig. 2.2 presents a micrograph of the cryofractured surface of a composite containing 20%(v/v) carbon black. Uniformly dispersed light spots represent carbon black particles. The particle size, in the range of 50 – 500 *nm*, is consistent with the primary aggregate size given by the manufacturer (weight mean aggregate size of 300 *nm*). The roughness of the fracture surface indicates good adhesion between the particles and the matrix.

2.2.2 Methods

Stress-strain behavior in uniaxial tension was measured at ambient temperature with ASTM 1708 microtensile specimens, cut from the compression molded plaques. The grip separation was 22.3 *mm* and included the fillet section, the specimen width was 4.8 *mm*. Specimens were deformed in an Instron

1123 testing machine at a rate of 20% *min*⁻¹, except when stipulated otherwise. Marks were drawn on the specimens to measure the draw ratio from a video recording. Electrical properties were measured with a four-terminal technique using a *Keithley* model 220 as current source, and *Keithley* model 619 for voltage and current measurement, as described previously⁽⁶⁴⁾. The device was interfaced to a computer to record data. The minimum time required to obtain a measurement was 0.12 s. The error in the measurements, determined with standard resistances, was less than 2% in the range 10⁻⁷ to 10⁻² *A* for current, and 10⁻⁵ to 100 *V* for voltage.

To measure in situ the changes in conductivity upon stretching, strip-like specimens were used with an initial length of $L_0 = 135$, width of $W_0 = 10$, and thickness $H_0 = 2$ *mm*. For measurements along the specimen length (parallel direction), flat clamps covered with copper foil were used. The clamps applied an approximately constant pressure even on the strained specimens and, therefore, could be used to measure resistance during deformation up to fracture. The measured resistivity did not depend on the specimen geometry or the pressure applied to the electrodes, furthermore gold electrodes deposited on the cut edges of the specimen gave the same resistivity as electrodes applied to the molded surfaces. Therefore, the measured parallel resistivity was taken as a bulk value, although the possibility that it represented a surface resistivity cannot be absolutely eliminated.

For electrical measurements through the thickness (perpendicular direction), electrodes consisted of thick gold layers (<200 *nm*) deposited on both surfaces. The specimen was mounted in the Instron and the stress σ , specimen length L , and voltage were recorded during uniaxial extension. The applied current was 10⁻⁵ *A* unless, at higher strains, the voltage approached the limits of the device, in which case the current was decreased. When this occurred, the resistance changed very slightly indicating that deformation did not alter the ohmic behavior.

All the composites exhibited ohmic behavior over the current range used to measure the electrical properties, Fig. 2.3. Linear behavior indicated that the conducting pathway existed in the as-processed materials and was not altered by application of voltage. Stretching did not compromise the ohmic behavior. The response remained linear after the materials were stretched to 20% strain and allowed to recover for 1 – 2 h.

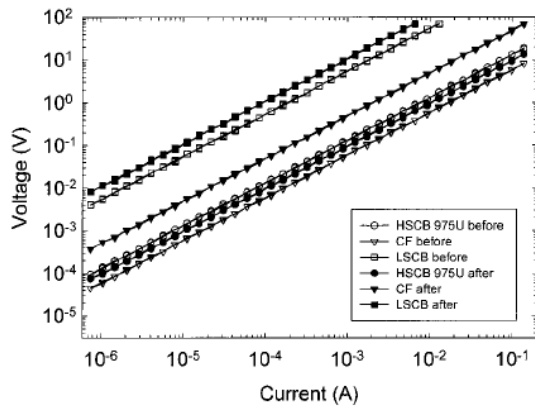


Figure 2.3 : Current-voltage relationship of EO with 20% (v/v) Carbon Fibre, 45% (v/v) Low Structure Carbon Black, and 20% (v/v) High Structure Carbon Black before (open symbols) and after (solid symbols) straining to 20% [Source: (64)] .

The resistivity was obtained from the measured resistance R and the geometrical changes in the specimen. The constant volume assumption, *i.e.* Poisson's ratio equal to $\nu \approx 0.5$, is generally considered valid for polymers above the glass transition temperature. With this assumption, the resistivities parallel and perpendicular to the extension direction were, respectively, given by:

$$\rho_{//} = R_{//} \left(\frac{WH}{L} \right) = R_{//} \left(\frac{V_0}{L^2} \right) \quad (2.1)$$

$$\rho_{\perp} = R_{\perp} \left(\frac{WL}{H} \right) = R_{\perp} \left(\frac{W_0 L}{H_0} \right) \quad (2.2)$$

By using Eqs. 2.1 and 2.2 to calculate resistivity, the volume V_0 was assumed constant, and possible volume changes due to void formation were neglected¹. Unless indicated otherwise, the parallel resistivity is reported.

2.3 Results and discussion

The percolation threshold is a basic characteristic of a conductive composite; in this case the percolation threshold defines the composition range for studying the effect of stretching on conductivity. Fig.2.4 shows the variation of the resistivity with the volume fraction of filler. A typical S-shaped curve is observed that separates three regions: insulating, transition, and conductive. The model that is most often

¹This assumption only rigorously stands for "low" strains.

used to quantify the changes in the transition and conductive regions is the so-called statistical percolation model⁽⁴⁾. Proposed by Kirkpatrick⁽⁸⁾ and Zallen⁽¹⁰⁾, this model predicts the electrical resistivity of an insulator-conductor binary mixture by assuming random positions of the filler particles. The result is a power-law variation of the resistivity ρ , above the percolation threshold:

$$\rho \propto \left(\frac{V - V_c}{1 - V_c} \right)^{-t} \quad (2.3)$$

where V is the volume fraction of filler, V_c the percolation threshold and t is a universal exponent that is close to 2 for a 3D dispersion. The two-parameter fit is represented in Fig. 2.4 by the solid line and gives $V_c = 0.12$ and $t = 2.05$. The value of the exponent t is consistent with the model prediction. On the basis of this result, composites with between 12.5 and 30%(v/v) filler were used to study the relationships between resistivity and mechanical deformation. The lower limit was determined by the percolation threshold, the upper limit was the maximum carbon black that could be dispersed in the EO matrix.

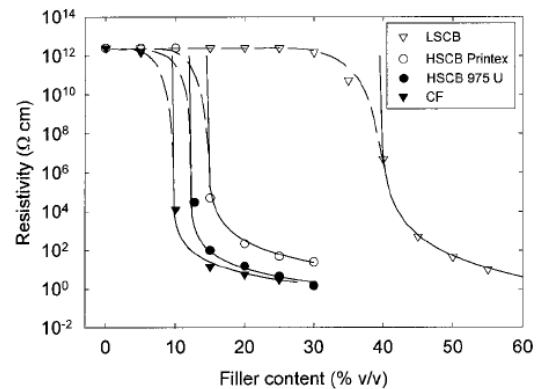


Figure 2.4 : Resistivity as a function of filler content. The solid lines are the statistical percolation fit from Eq. 2.3 [Source: (64)] .

The resistivity as a function of filler content showed the typical S-shaped dependency with three regions: dielectric, transition and conductive, Fig. 2.4. Specimens with low filler content were almost nonconductive. However, at a critical composition that depended on the specific filler, the resistivity fell sharply into the range of 1-10 Ω .cm. Assuming that the critical filler content corresponded to a percolation threshold, the HSCB and CF composites formed a continu-

ous network with 10-15% (v/v) filler, which was considerably less than the 40% (v/v) required for the LSCB composite. A value of 20-40% (v/v) is typical of spherical particles. The high aspect ratio of the fibers, and the aggregate form of the high structure carbon black, which increased the probability of particle-particle contacts, accounted for the low percolation thresholds.

2.3.1 Mechanical properties

The influence of filler content on the mechanical properties of reinforced-elastomers has been extensively reported in the literature⁽⁶⁶⁾. It is generally agreed that the increase in modulus is due to strong interactions between polymer chains and particles, and/or between particles and particles.

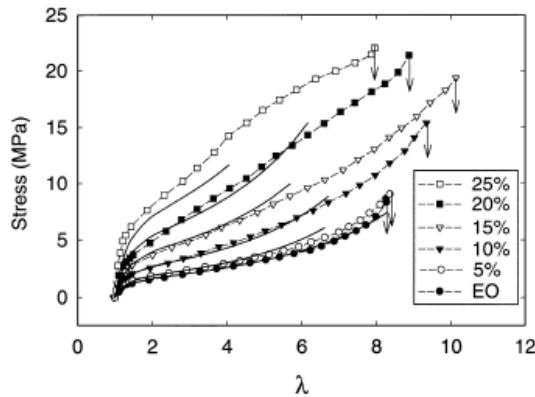


Figure 2.5 : Mechanical properties of composites with various amounts of carbon black. The solid lines are fits to the sliplink model, Eq. 2.6, with the shift factor from Eq. 2.5 for $f = 4.83$ [Source: (65)] .

Fig. 2.5 shows the stress-strain curves obtained with various amounts of carbon black dispersed in the EO matrix. By increasing the volume fraction of filler, gradual improvement in modulus and tensile strength was observed. The properties at higher strains were especially impressive. Typically, reinforcement even with high-structure carbon black is accompanied by a decrease in elongation to break^(67;68). This was not the case with the EO composites, which retained the high elongation of the unfilled elastomer even with the maximum filler content of 25% (v/v). As the stress-strain curves had the same shape as the unfilled EO, it was of interest to compare the reinforcement effect with the Guth hydrodynamic models⁽⁶⁹⁾ that are commonly used in the rubber litera-

ture. Assuming perfect adhesion between filler and matrix, an important consequence of the Guth analysis is that the stress-strain curves are proportional with the proportionality constant determined by the amount of filler. To test the possibility that the curves would superpose with a simple shift factor, the data are plotted in Fig. 2.6 as the rubber modulus $G_c = \sigma (\lambda - 1/\lambda^2)^{-1}$ where λ is the extension ratio and σ is the engineering stress. The curves for the composites were shifted by a factor α_v to obtain the best overlap with the unfilled elastomer. A gradually decreasing modulus at low strains was followed by a region of almost constant modulus. The stress-strain behavior superposed well to about 400% strain ($1/\lambda \approx 0.2$). Deviations toward lower modulus values at large strains, especially for high-filler contents, were consistent with loss of particle-matrix adhesion.

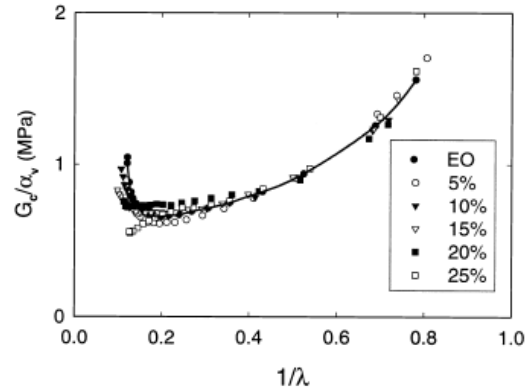


Figure 2.6 : Rubber modulus $G_c = \sigma (\lambda - 1/\lambda^2)^{-1}$ of composites with various amounts of carbon black. The moduli were vertically shifted (by a shift factor α_v) to the match that of unfilled EO. [Source: (65)]

Fig. 2.6 is a plot of the shift factors derived from the superposition. The variation of the shift factor with filler volume fraction was smooth and, in particular, there was no transition in the vicinity of the percolation threshold. Therefore the results were compared with Guth reinforcement models⁽⁶⁹⁾. The model for spherical reinforcing particles has the form:

$$G_C = G_0 (1 + 2.5V + 14.1V^2) \quad (2.4)$$

where G_C and G_0 are the moduli of the composite and matrix, respectively. The linear term accounts for the reinforcing effect of individual particles, and the second power term is the contribution of particle pair interactions. This model significantly underestimates

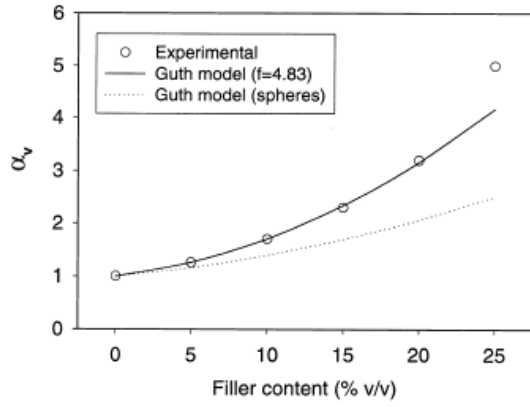


Figure 2.7 : Comparison of the experimental shift factors with the Guth models for spherical particles (dotted line, Eq. 2.4) and rodlike particles (solid line, Eq. 2.5) [Source: (65)]

the observed reinforcement, as shown in Fig. 2.7. The difference between experimental data and Eq. 2.4 was even observed for a volume fraction as low as 10% (v/v), where the model is most applicable. An alternative formulation accounts for non-spherical particles. For rod like particles of aspect ratio f , the reinforcement is given by²:

$$G_{Cf} = G_0 (1 + 0.67fV + 1.62f^2V^2) \quad (2.5)$$

Using f as an adjustable parameter, an excellent fit was obtained with $f \approx 4.83$ for filler contents less than 25% (v/v), Fig. 2.7. The importance of particle-particle interactions was inferred from the need for the second term in Eq. 2.5, to describe the mechanical reinforcement. The fit did not hold for a volume fraction of 25%(v/v), probably because the amount of polymer was insufficient to completely wet and disperse the filler. Unsuccessful attempts to disperse more than 30%(v/v) filler supported this hypothesis. Good agreement of experimental results with Eq.2 was, however, rather surprising because the model presumably applies only for one parameter stress-strain curves⁽⁶⁷⁾, and the mechanical behavior of the EO matrix cannot be described properly by classical rubber theory. Instead, the elastomeric EO copolymer is described by a slip-link model that operates with four parameters⁽⁵⁷⁾: the density of crosslinks

²One may notice that $\lim_{f \rightarrow 1} (G_{Cf}) \neq G_C$. Eq. 2.4 and 2.5 are thus incompatible. Eq. 2.5 can actually only be used for fillers with high aspect ratio, or for highly structured filler for which $f \geq 3$

(N_C), the density of slip-links (N_S), a slippage parameter (η) and an inextensibility parameter (α). The free energy derived from the slip-link theory takes the form:

$$\begin{aligned} \frac{F}{kT} = & \frac{1}{2}N_S \left(\sum_i \left[\frac{\lambda_i^2 (1 + \eta) (1 - \alpha^2)}{(1 - \alpha^2 \sum_i \lambda_i^2) (1 + \eta \lambda_i^2)} + \log (1 + \eta \lambda_i^2) \right] \right. \\ & \left. + \log \left(1 - \alpha^2 \sum_i \lambda_i^2 \right) \right) \\ & + \frac{1}{2}N_C \left(\sum_i \left[\frac{\lambda_i^2 (1 - \alpha^2)}{(1 - \alpha^2 \sum_i \lambda_i^2)} + \log (1 + \eta \lambda_i^2) \right] \right. \\ & \left. + \log \left(1 - \alpha^2 \sum_i \lambda_i^2 \right) \right) \end{aligned} \quad (2.6)$$

where the summation is made over the Cartesian components of strain. In uniaxial tension, the stress is obtained by:

$$\sigma = \left(\frac{\partial F}{\partial \lambda} \right)_{TV} \quad (2.7)$$

The stress-strain behavior of the unfilled matrix was fit with two parameters held constant, $\eta = 1.1$ and $\alpha = 6.5 \times 10^{-2}$. Values for N_C and N_S of 0.37 and 5.76 MPa, respectively, gave the calculated stress-strain curve in Fig. 2.5, which fit the entire experimental stress-strain curve very well. The calculated curves for the composites were obtained by multiplying the right side of Eq. 2.6 by the shift factor obtained from Eq. 2.4 with $f = 4.83$. Good fit with the experimental results extended to high strains, about 500%. The agreement demonstrated that the Guth model can apply for matrices with multiple parameter stress-strain curves. Loss of reinforcement due to extensive damage in the composite at higher strains caused the experimental curve to drop below the calculated one.

2.3.2 Electrical properties under uniaxial strain

The resistivity as a function of strain for different amounts of filler is displayed in Fig. 2.8.

These curves can be separated in four regimes with increasing strain, Fig. 2.9. Regime I is characterized by a sharp increase in resistivity and corresponds to

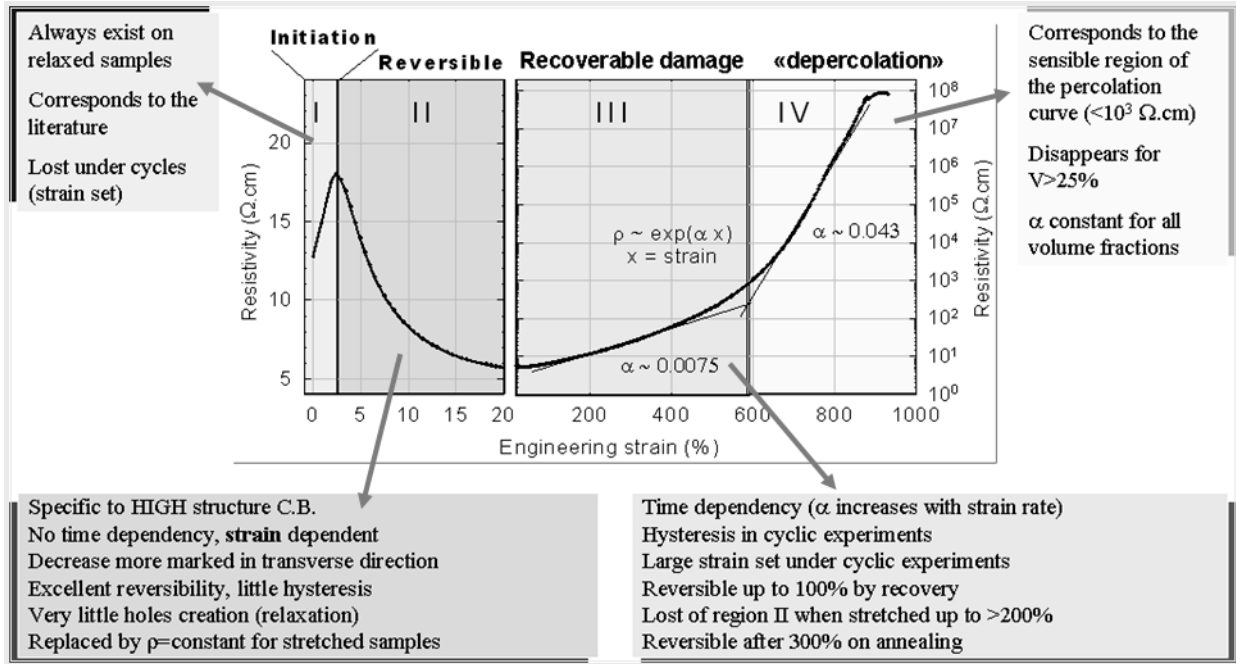


Figure 2.9 : Definition of the four regimes in the resistivity-strain relationship. Case of EO filled with 20%(v/v) carbon black [Source: (65)] .

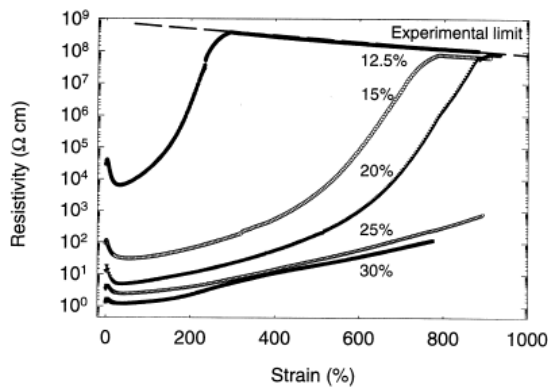


Figure 2.8 : Influence of carbon black content on the electrical properties under large strain. All carbon black contents are above the percolation threshold [Source: (65)] .

the behavior typically observed with vulcanized rubber composites. It is generally accepted that the increased resistivity is due to breakage of the carbon black network. Regime I ends at a few percent strain in the EO composites. Regime II, extends from the maximum in resistivity at 3 – 4% strain to about 30% strain. It is characterized by a rapid decrease in the resistivity. This behavior at such a low strain is unusual and has only been observed previously in a few instances^(58;70). In cases where a decrease in resistivity is observed in vulcanized rubber composites, it generally occurs at strains an order of magnitude higher⁽⁷¹⁾. In regime III, the resistivity gradually increased. The exponential relationship $\rho \propto \exp(\beta \varepsilon)$ where ε is the engineering strain. The dimensionless parameter β was essentially independent of composition: $\beta \approx 8 \times 10^{-3}$. This indicated that the filler volume fraction had little influence on the change in resistivity over a very broad range of strain, although the magnitude of the resistivity in regime III decreased with the amount of filler. Regime III ended when the resistivity reached about $10^3 \Omega \cdot \text{cm}$; the corresponding strain increased with the amount of filler. The resistivity at the onset of regime IV corresponded to that observed in the vicinity of the percolation transition, Fig. 2.4. The correlation suggests that the relatively weak conducting network with resistivity

about $10^3 \Omega \cdot \text{cm}$ can be destroyed either by decreasing the filler volume fraction, or by stretching the composite. “Depercolation” explained the rapid increase in resistivity upon further stretching. For all volume fractions of filler, growth in resistivity was exponential with a much larger exponent β' than in regime III, $\beta' \approx 5 \times 10^{-2}$. Although the electrical response to strain followed the same trends for all compositions, not all the compositions exhibited all four regimes. Thus, the composition with 12.5% (v/v) filler, which was close to the percolation threshold, did not exhibit regime III. Also, the composites with the most filler, 25 and 30% (v/v), did not exhibit depercolation, regime IV. The properties in regimes II and III were considered the most interesting, as these differentiated the EO composites from the more widely investigated composites that utilize a vulcanized elastomer matrix. Therefore, the properties in regimes II and III were explored in more depth using a single composition with 20% (v/v) filler. The effect of strain rate on the stress-strain and resistivity-strain behavior is demonstrated in⁽⁶⁵⁾, and summarized in Fig. 2.9. The mechanical response of unfilled EO at ambient temperature did not depend on strain rate in this range of strain rates. Changing the strain rate by two orders of magnitude also had little effect on the mechanical response of the composites. Regimes I and II in the resistivity-strain behavior were virtually strain-rate independent⁽⁶⁵⁾. This observation is of importance for certain applications such as strain gauges. Regime III, on the contrary, showed a strain-rate effect similar to that observed with vulcanized elastomers^(63;72). Specifically, the parameter that described the exponential dependence of the resistivity gradually increased with strain rate: $\beta' \approx 2.5 \times 10^{-3}$; 6×10^{-3} and 1.0×10^{-2} , for strain rates 1, 10, and 100% min^{-1} , respectively. Although the electrical response revealed strain-rate dependent changes in the microstructure of the conducting network, these changes did not significantly affect the mechanical response.

2.3.3 Model for EO filled with high-structure carbon black

The four regimes in resistivity of a composite with 20% (v/v) carbon black are shown in Fig. 2.9. Regime I is generally attributed to network breakage; in the present case, it can also be considered as an initiation phase for regime II. In regime II, the composite

is differentiated from others described in the literature by having virtually no strain rate dependency in the resistivity up to 30% strain. Moreover, in this regime the composite exhibited no permanent strain or irreversible electrical properties during mechanical cycling. These combined properties would make this composite useful as a strain gage. The primary characteristic of regime III was preservation of the conducting network during deformation to high strains. The properties were recoverable upon rest after straining to 100%. Above 200% strain, the composite did not recover completely upon rest; a Mullins effect also indicated that the composite was damaged. However, the properties were restored by annealing above the melting temperature of the matrix. The mechanistic explanation of regime IV emerged from the percolation curve (2.4). Regime IV, was thought to result from the breakdown of the percolating network, and therefore was called “depercolation”.

Using the concept of secondary aggregates⁽⁵¹⁾, regime II could possibly be explained as a reversible rearrangement within the weakly bonded secondary aggregates. In this case, the maximum in resistivity between regimes I and II would be interpreted as the yield strength of the secondary aggregate. Although this mechanism could not be definitively rejected, it is based on the controversial definition of secondary aggregates. Moreover, it assumes that aggregates that were not broken during the rather forceful mixing process could be reversibly deformed during the mild uniaxial extension. Furthermore, this mechanism would not be specific to the EO matrix, and regime II has yet to be reported for carbon black-filled elastomers with permanent cross-links. Finally, this mechanism cannot account for the characteristics of regime III that should, to some extent, be related to regime II.

The EO filled with high-structure carbon black exhibited a combination of properties not generally achievable with this type of filler in an elastomeric matrix, including a decrease in resistivity upon stretching that was reversible up to 20% strain (regime II) and low resistivity with good mechanical properties at high strains (regime III). Furthermore, these characteristics were specific to high-structure carbon black, as composites of the EO elastomer with low-structure carbon black or carbon fibers exhibited more conventional behavior⁽⁶⁴⁾. An explanation appears to require the unique features for both filler and matrix. A possible structural model is presented in Fig. 2.10, page 29.

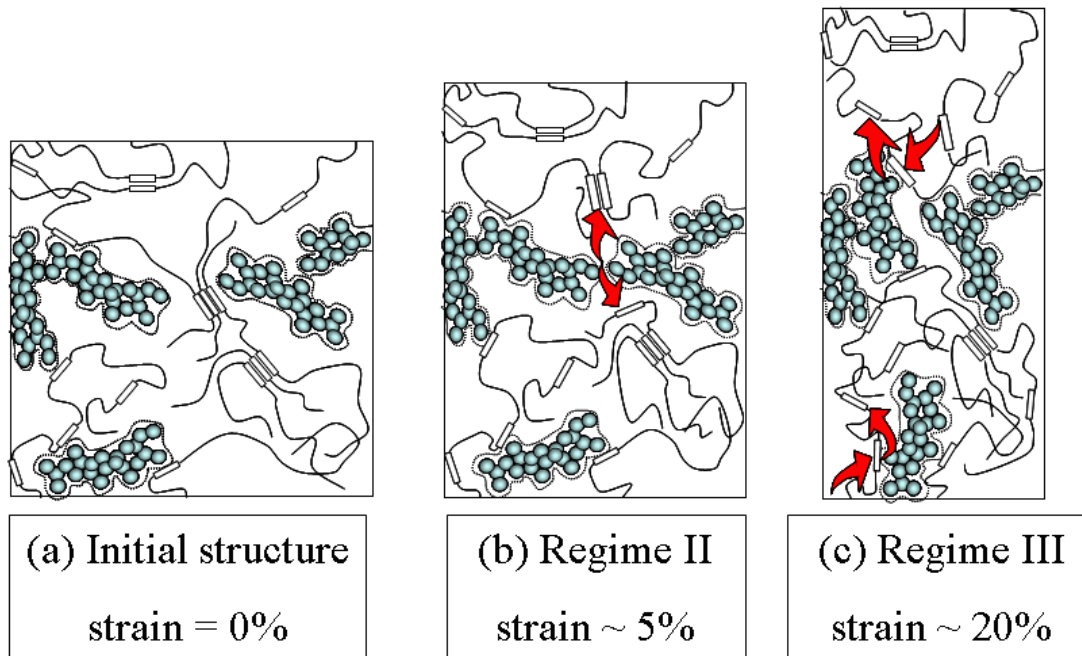


Figure 2.10 : Schematic representation of the proposed microstructural mechanisms for the changes in resistivity upon stretching [Source: (65)] .

In contrast to a vulcanized elastomer, the concept of a network of flexible chains with fringed micellar crystals serving as the multifunctional junctions provides the structural basis for EO elastomers. A single polymer molecule contains many segments that are long enough to crystallize; these can be incorporated into different crystals to form a network, Fig. 2.10a.

Upon stretching, the fringed micellar junctions of EO elastomers are not fixed, but are thought to provide a sliding topological constraint by a process of detachment-attachment, which can also be viewed as partial melting⁽⁵⁷⁾. As a result of local stress concentrations, the actual strain in the vicinity of the particle can be several times higher than the average macroscopic strain⁽⁷³⁾. Indeed, local strains in regime II may be high enough for crystalline junctions to “melt” and flow out from the space between nearby particles, Fig. 2.10b. A new electrical pathway is thus created or an existing pathway is improved. The effect should be particularly noticeable in the transverse direction, which contracts during straining due to Poisson’s effect. Recovery is driven by the elastic deformation of the surrounding network of fringed micellar crystals and entanglements. It would seem reasonable that a threshold strain should be observed. The maximum in resistivity between regimes I and II

is interpreted as this threshold. The good mechanical properties and low resistivity in regime III suggest that the system tolerates high strains with very little damage accumulation. It can be imagined that particles incorporated into a network of mobile junctions are less constrained during elongation than those in a network of fixed junctions, and this would facilitate rotation and translation of aggregates^(61;62). Additionally, at high strains it is necessary to consider the role of particle-matrix adhesion. The embedded carbon black particles adhere strongly to the matrix, as indicated by conformity to the Guth mechanical model. The mode of adhesion is suggested by analogy, to the bound rubber models proposed for vulcanized elastomers^(74;75;76). Linear chain segments, which are not part of a fringed micellar crystal, are ideal candidates for adsorption to the step-like edges of the carbon black particle, as illustrated in Fig. 2.11.

Additionally, it is suggested that the particle-matrix bond is dynamic. Although it is imagined that particle-matrix adhesion is not disrupted by the relatively low strains in regime II, higher local stresses in regime III may be sufficient to overcome the physical bond and allow the detached chain to relax closer to the Gaussian state, Fig. 2.10c. In the process, another chain segment can form a physical bond with the newly created adsorption site, and the damage

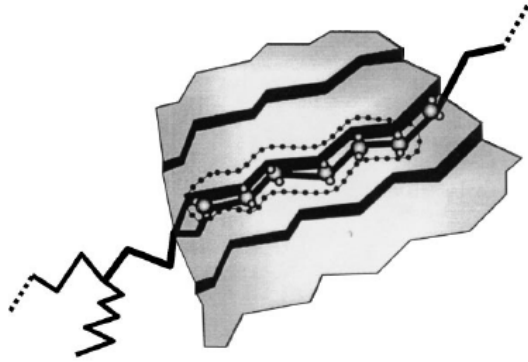


Figure 2.11 : Schematic representation showing adsorption of a linear EO chain segment to the steplike edges of a carbon black particle, to produce good adhesion, adaptation from^(74;75) [Source: (65)]

to the system is minimized. This constitutes a type of “selfhealing” mechanism that is unique to EO elastomers. The shortest or most strained chain segments are affected first, and reorganize to increase the connecting length between two particles (lower arrows in Fig. 2.10c). The dynamic nature of crystal junctions also permits chain segments to melt and adsorb to highenergy sites (upper arrows in Fig. 2.10c). These irreversible physical changes in particle-matrix adhesion are reflected in the Mullins effect, *i.e.* the modulus decrease on reloading. The higher set strain of the composite compared to the unfilled elastomer suggests that the restoring force of the network is not sufficient to completely reverse the physical changes. However, the entanglement network almost completely erases the permanent set if the temperature is raised above the crystalline melting point.

2.4 Conclusion

In summary, this study focused on a new elastomer that is a candidate matrix material for conducting composites. The fundamental difference in the network structure of EO elastomers compared to conventional vulcanized rubbers, *i.e.* multifunctional physical junctions compared to fixed chemical crosslinks, was manifest in the property spectrum achieved with EO composites. Examination of the stress-strain and concurrent resistivity-strain behavior of EO with a high-structure carbon black revealed characteristics that differentiated EO composites from those that

utilize more conventional vulcanized rubbers. Particularly interesting was a reversible and strain-rate independent decrease in resistivity up to 30% strain, which could qualify EO composites for strain gauge applications. The properties at higher strains were also impressive. The composites demonstrated modulus reinforcement in accordance with the Guth model for good particle-matrix adhesion. Typically, reinforcement even with high-structure carbon black is accompanied by a decrease in elongation to break. This was not the case with the EO composites, which retained the high elongation of the unfilled elastomer even with the maximum filler content of 25% (v/v). The good high-strain mechanical properties were accompanied by low resistivity. Filler contents of 20-25% (v/v) produced a composite in which the resistivity remained above the percolation threshold, *i.e.* less than $10^3 \Omega \cdot \text{cm}$, up to fracture at 800-900% strain. Synthesis of the results of various thermo-mechanical treatments led to a microstructural model based on a matrix network of mobile, multifunctional physical junctions, which incorporated a dynamic bond between EO chain segments and high-structure carbon black particles.

Chapter 3

Control of the *meso* structure

⊙ **Abstract** ⊙

This chapter describes developments of carbon-black epoxy composites with unique electrical properties. The influence of the volume fraction of carbon black was found in remarkable disagreement with the predictions of the statistical percolation theory for both real and imaginary parts of the conductivity. For both properties a dramatic variation at a given fraction of carbon black was evidenced. The evolution of these transport quantities with the volume fraction of carbon black could only be explained considering a phase transition from a dispersed to an agglomerated state of the conducting fillers. This transition was successfully verified by optical microscopy of thin polished sections of cured samples. A simple model based on electrostatic repulsion between the carbon-black particles was proposed to interpret such a singular insulator-to-conductor transition. This model assumes a permanent charge on the surface of the CB particles. To verify this permanent electrical dipoles, the influence of a static electric field applied on these composite during the curing process was thus investigated. Growth of dendrites from the anode was observed in situ by optical transmission microscopy indicating a negative charge on the surface of the CB. This forced percolation experiments also indicated a drastic reduction in the sample resistivity. The final resistance of the composites with a fixed CB content could indeed be tailored within about seven orders of magnitude by varying the applied voltage and the curing temperature of the mixture.

Contents

3.1	Percolation failed?	32
3.1.1	A 2^{nd} order phase transition...	32
3.1.2	Particle-particle interactions	32
3.1.3	Experimental	33
3.1.4	Results and discussion	33
3.1.5	Interpretation of the transitions	35
3.1.6	Verification through characterization at meso scale	36
3.2	Control at the <i>meso</i> scale	37
3.2.1	Introduction and goal	37
3.2.2	Evidence for agglomeration	37
3.2.3	Effect of applied voltage	39
3.2.4	Effect of temperature	39
3.3	Conclusion	40

3.1 Percolation failed?

3.1.1 A 2nd order phase transition...

For several decades, the electrical properties of insulator-conductor composite have been widely studied with both applied and fundamental interest^(6;77). The dc conductivity is related to the formation of a network of filler particles within the matrix; it increases sharply at a characteristic conducting particle concentration (V_c) known as the percolation threshold. The percolation transition does lead to strongly non-linear properties, but since Fortuin and Kasteleyn⁽⁷⁸⁾ demonstrated that it can be identified with a second-order phase transition, one knows that physical quantities like dc conductivity should exhibit a continuous behavior at this transition.

To describe the insulator-to-conductor transition a large variety of models have been proposed in the literature^(4;9). For several decades the statistical percolation model explained, at least qualitatively, all experimental data. However, as outlined by Carmona⁽⁵⁹⁾, a full understanding of the electrical and structural properties must involve the specific preparation conditions of the materials, namely, the occurrence of a colloidal phase. This author noticed, in the same review⁽⁵⁹⁾, that a better description for the structure formation would be useful for a complete and comprehensive understanding of these kinds of materials. The question of “the rules of the game” for the cluster formation has arisen, as well as the influence of the preparation method^(4;76) on the electrical properties of the composite materials. The percolation model proposed by Sumita and co-workers^(60;76) was the first attempt to answer this question by accounting for the filler-matrix interactions.

In this thermodynamic model it is assumed that the free interfacial energy of the system Δg cannot exceed a “universal value” Δg^* . Thus, the network formation results from the aggregation of the CB particles to prevent the free energy from rising above the Δg^* value. This Δg^* concept allows the authors to interpret correctly the measurement of different values for the percolation threshold varying the free interfacial energy between filler and matrix.

In a very popular review on the models to explain the electrical conductivity of binary mixtures, Lux⁽⁴⁾ pointed out the experiment performed by Harbour,

Walzak, and Veregin⁽⁷⁹⁾ showing that the mixing process may induce an electrical charging of the CB particles. Lux⁽⁴⁾ noticed that such permanent surface charges might stimulate interactions between CB particles and the polymeric host. After this review was published, Schueler *et al.*⁽⁸⁰⁾ assumed that the presence of such an electrical charge at the surface of their black induces particle-particle interactions that could be modified by addition of salt during the thermal curing.

3.1.2 Particle-particle interactions

Between two fillers in a medium an attractive London-Van der Waals potential has to be considered. This interaction is described by a $-1/r^6$ potential, where r is the distance between the particles. It is first assumed that the particles surfaces are negatively charged. Thus, as already postulated by Schueler *et al.*⁽⁸⁰⁾ and measured by Harbour *et al.*⁽⁷⁹⁾, the CB particles possess a permanent electrical charge which leads to a long-range Coulombic repulsion among each other. This Coulombic interaction, described by a $1/r$ potential, is comparable to the one commonly used in colloid science with the acronym DLVO¹,⁽⁸¹⁾ to obtain an electrostatic stabilization of dispersions. The total potential between two fillers Fig. 3.1, is thus the sum of two competitive potentials plus a repulsion term proportional to $1/r^{12}$, which accounts for the contact repulsion.

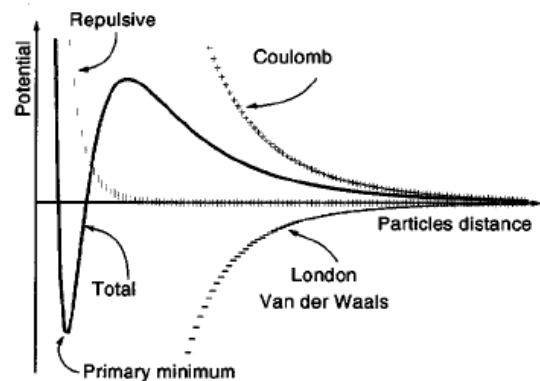


Figure 3.1 : Potential energy of interaction between two charged particles [Source: (23)] .

Due to thermal agitation the particles are moving in the medium. If the collisions created by this Brownian

¹DLVO stands for Derjaguin-Landau-Verwey-Overbeek (colloid chemistry theory)⁽⁸¹⁾

motion involve sufficient energy to overcome the electrostatic barrier, the pair of particles falls in a deep primary minimum of the total potential energy and becomes irreversibly aggregated. In the case of CB epoxy composites this can also be obtained by shearing the composite before curing^(80;82). The height of the barrier depends on the electric charge at the surface of the particles. It is also influenced by the ionic strength of the matrices, which can be altered by the addition of salt.

3.1.3 Experimental

The matrix used in this study was an epoxy polymer obtained from the reaction of a bisphenol-A resin (Araldit LY556, Ciba Geigy) with an aromatic amine hardener (Araldit HY932). The filler component was an extra conductive carbon black (Printex XE 2, Degussa AG) that consisted of aggregates composed of spherical particles with a mean diameter of 30nm. The details of the sample preparation have been described elsewhere^(38;80). The first step consists of mixing 500g of the resin with the desired amount of CB for one hour at 5000 rpm using a dissolver disk at room temperature. This step induced a good dispersion of the CB particles within the epoxy resin and reduced the size of the CB agglomerates. After this strong stirring the CB agglomerates have distributed sizes with a mean diameter in the order of 0.5 μm . Samples were cured after another stirring of one hour at 1000 rpm with the hardener at room temperature. Composites prepared this way will be referred to as "A".

In order to alter the interaction potential, the addition of salts is commonly utilized with colloids. Changes in the ionic strength of the matrix was also performed in the present study to test the hypothesis. Thus another preparation was performed in which CuCl_2 (Fluka) was added and mixed with the hardener. The salt concentration in the resin was adjusted to $3 \times 10^6 \text{ mol.g}^{-1}$. These samples prepared in the same conditions than samples A, but with an addition of CuCl_2 will be referred to as "B".

The curing process consisted of heating the mixtures under vacuum conditions for 3 hours at 80°C to reach the gel point and for 8 hours at 140°C to complete the polymerization of the matrix. Parallelepipedic samples were cut having dimensions of approximately $1 \times 1 \text{ cm}^2$ wide and 0.3 cm thick. Electrical contacts were made of silver paint on opposite sides. The

ac electrical measurements were carried out at room temperature with a *HP 4284A* impedance-analyzer with a four-point probe technique. A voltage of 5 V in amplitude was applied and the complex conductivity σ^* versus the frequency f was measured in the range of 100 Hz to 1 MHz. The complex dielectric constant ε^* is related to the conductivity by $\varepsilon^* = \sigma^*/i\omega\varepsilon_0$, where ω denotes the angular frequency and ε_0 the dielectric constant of the vacuum. The dc conductivity was measured with a *Keithley 617* electrometer. A minimum of three samples was tested to determine the electrical properties for each composition. Transmission Optical micrographs were obtained from thin polished sections of cured composites by using a *Leica Polyvar* microscope.

3.1.4 Results and discussion

This section describes first the electrical conductivity measured versus the frequency for different amounts of CB. Second, it will be shown that the evolution of real and imaginary parts of the conductivity versus filler content is in clear disagreement with the prediction of the statistical percolation theory. Third, an attempt to explain such a departure is proposed, which is based on the dramatic changes in the filler arrangement within the matrix. This assumption is finally verified with transmission optical micrographs of the cured sample.

3.1.4.1 Frequency dependence

Fig. 3.2 displays the frequency dependence of the electrical conductivity for the salt-agglomerated samples B.

These composites exhibited a typical dielectric behavior below the conduction threshold *i.e.* the conductivity increased linearly with the frequency while the phase angle was close to $\pi/2$. Above this threshold of 0.03% a finite conductivity led to a plateau at low frequency corresponding to the electrical response of the percolating network, Fig. 3.2. The conductivity increased at higher frequencies due to the growing importance of the polarization effects on the macroscopic conductivity.

Increasing the volume fraction of fillers increased the low-frequency conductivity and led to a broader plateau. Similar results have frequently been reported^(11;14;15) and related to the formation of a percolating network in the material. With composites B

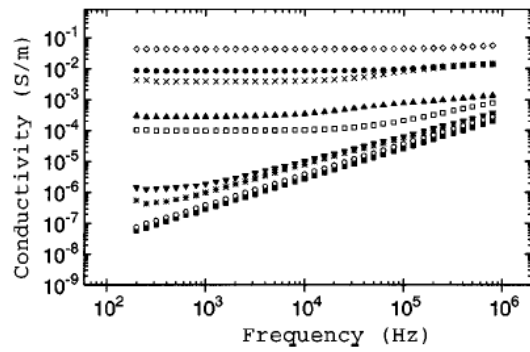


Figure 3.2 : Frequency dependence of the conductivity for 0 (■), 0.012 (O), 0.03 (*), 0.06 (▼), 0.12 (□), 0.3 (▲), 0.48 (x), 0.6 (●), and 0.9 (◇) volume percent of carbon black with addition of $CuCl_2$ [Source: (23)] .

each point of the conductivity frequency plane seemed reachable, choosing the right volume fraction of fillers. The insulator-to-conductor transition appeared continuous.

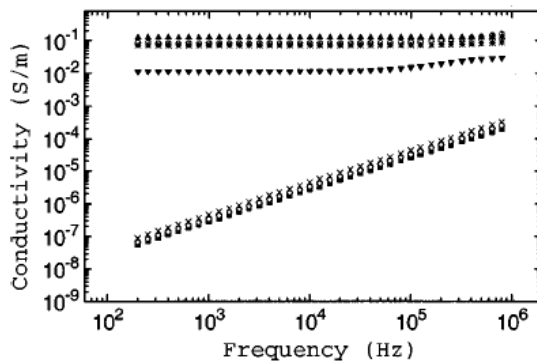


Figure 3.3 : Frequency dependence of the conductivity for 0 (■), 0.012 (O), 0.03 (*), 0.06 (▼), 0.12 (□), 0.3 (▲), 0.48 (x), 0.6 (●), and 0.9 (◇) volume percent of carbon black without addition of $CuCl_2$ [Source: (23)] .

On the contrary, in the case of samples *A* a jump in the conductivity at the conduction threshold of 0.9% was measured, Fig. 3.3. While a purely dielectric behavior was also observed below this threshold, the conductivity was almost independent of the frequency above this critical volume fraction where conduction took place. Moreover, there was a large gap between the conductivity measured on both sides of the transition. Nevertheless, for similar amounts of CB above 0.9%, the frequency dependencies of the conductivity for the samples *A* and *B* were comparable.

3.1.4.2 Real and imaginary part of the conductivity

Fig. 3.4 displays the real part of the conductivity measured at 1 kHz as well as the dc conductivity for both sets of samples². The values of the dc conductivity were found very close to that of the ac conductivity at 1kHz as already observed in the literature⁽⁸³⁾. As already mentioned, composites *B* exhibited a continuous increase in the conductivity with the CB content. The variation of the conductivity with the volume fraction of filler was in good agreement with the power law equation 2 and the critical exponent t was found to be 2.4 ± 0.2 , left inset of Fig. 3.4. Such a value is compatible with the predictions of the statistical percolation theory, even if non-universal. Samples *A* remained good insulators up to a volume fraction of 0.9%. This defined accurately the conduction threshold as an increase of the CB content as low as 0.03% led to a jump in the conductivity of about seven orders of magnitude. The conductivity reached values that were surprisingly close to those obtained for *B* composites. Increasing the volume fraction of CB above 0.93% induced but a minor changes in the conductivity. Such a behavior could not be fitted properly with Eq. 2 and gave anyway a value of 0.64 for t , right inset of Fig. 3.4. This very low values corresponds to an unrealistically strong transition, that could not be related to the statistical percolation theory.

The relative permittivity at low frequency (1 kHz) for these two sets of composites is depicted in Fig. 3.5. From this graph, it is evident that this quantity is, again, in disagreement with the percolation theory, which predicts (Eq. 1) a divergence in the permittivity close to the percolation threshold. Indeed, the dielectric constant in the case of composites *B* increased above the conduction threshold. As a matter of fact, for the composites “B”, the real, Fig. 3.4 and imaginary Fig. 3.5 changes in conductivity as a function of the filler content were quite comparable.

For samples *A* almost no change in the dielectric constant was measured by varying the volume fraction of CB below the conduction threshold. This observation is very important for the understanding of

²The real part of conductivity could not be measured accurately below the conduction threshold, as the phase angle was close to $\pi/2$. A value in the order of $10^{-9} S.m^{-1}$ overestimates the real conductivity of the matrix, which was found with another setup⁽⁸²⁾ to be close to $10^{-12} S.m^{-1}$. The main reason for this difference is the dielectric losses that takes place in ac field.

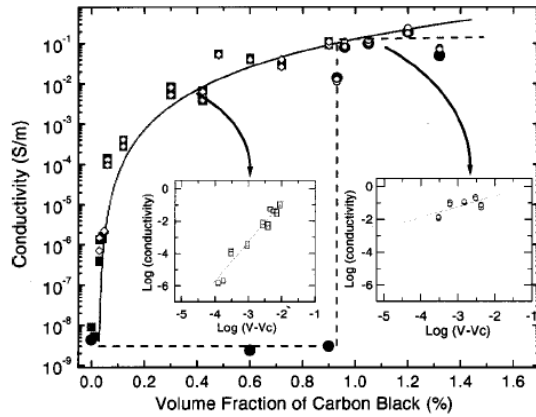


Figure 3.4 : Real part of the conductivity at 1 kHz with (p) and without (u) addition of $CuCl_2$. dc electrical properties with (F) and without (E) addition of $CuCl_2$. Insets: comparison with power law dependence [Source: (23)] .

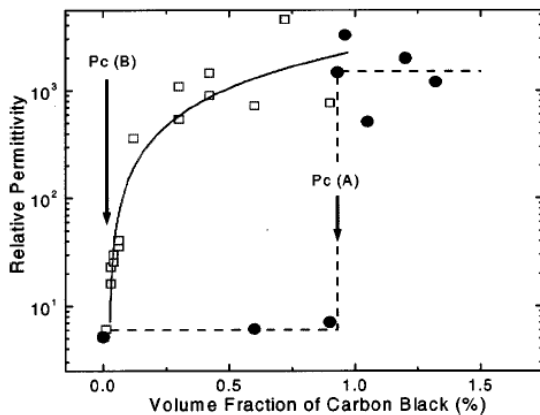


Figure 3.5 : Imaginary part of the conductivity at 1 kHz with (\square) and without (\bullet) or (\circ) addition of $CuCl_2$. dc electrical properties with and without addition of $CuCl_2$. Insets: comparison with power law dependencies [Source: (23)] .

the microstructure in the materials. Following scaling theory, the divergence of the permittivity is related to the divergence of the correlation length. A sharp increase in the latter with the volume fraction of filler is a quite normal behavior for a random composite material approaching the transition. The constant value for the permittivity was, in the present case, interpreted as due to the Coulombic filler-filler repulsion that disturbs the cluster formation. At the threshold, another discontinuity was evidenced concerning the permittivity. A change of 0.03% of the CB content induced a dramatic change of two orders in magnitude. As a result, ε that seemed to arise from the network formation.

3.1.5 Interpretation of the transitions

The increase in the relative permittivity slightly above the conduction thresholds for both sets of samples was contrary to the decrease predicted by the percolation theory for randomly dispersed composites. Moreover, samples B exhibited a continuous increase for the real part of the conductivity, but it was not possible to process samples of type A with an intermediate conductivity, because it was not possible to weigh CB and epoxy resin so as to obtain accurately 0.915% of CB content. It was evident anyway that this behavior could not be explained by the classical theory for binary insulator-conductor mixtures, but that the dynamics of the CB fillers in the polymer host had to be considered.

At the end of the processing i.e. after strong stirring, no conducting network exists in the composite, whatever the salt concentration. This has been shown in a previous study by measuring the conductivity versus the time of the curing process: the initial conductivity were always very low⁽⁸⁴⁾.

An increase in the ionic concentration of the epoxy resin lowers the potential barrier among the CB particles in samples B . Thus, the fillers will form easily clusters from this initial state, with the support of the Brownian motion. A three-dimensional network will be created and, accordingly, a finite conductivity. Because of this kind of cluster formation, a strongly agglomerated structure will be achieved and thereby a very low conduction threshold, compared with the standard percolation theory and most of the results proposed in the literature. The final microstructures of these composites are thus not random, Fig. 3.6, and

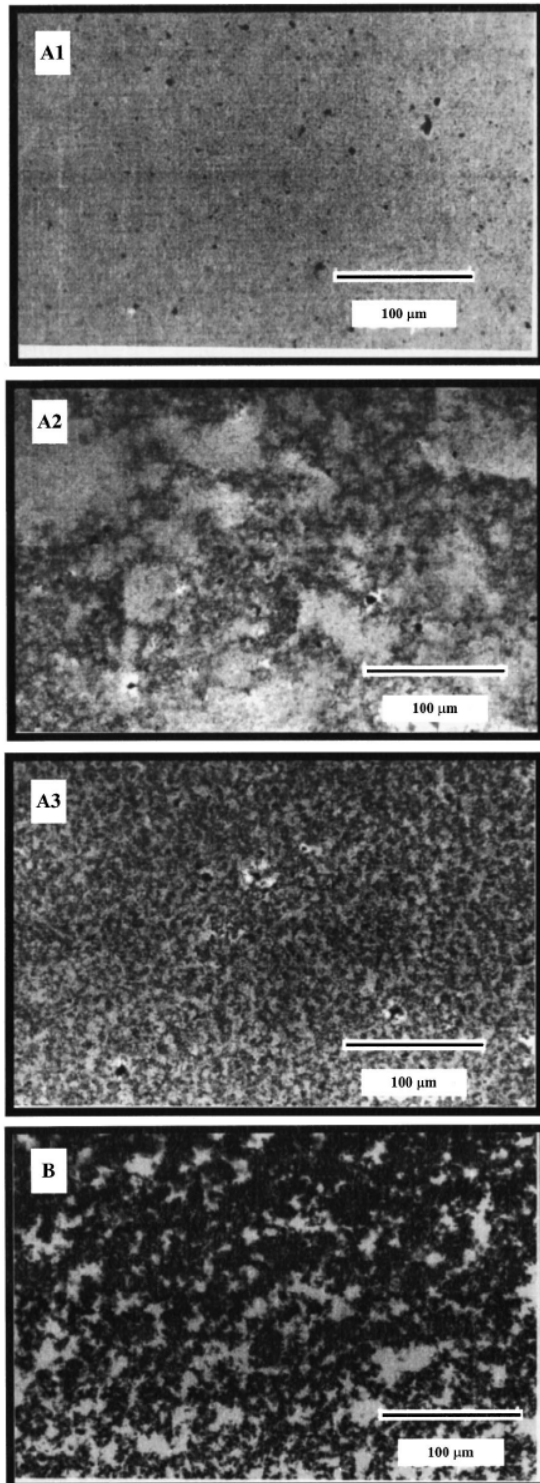


Figure 3.6 : Transmission optical micrographs of thin polished sections of cured material, (A1) 0.9%, (A2) 0.93%, and (A3) 0.96% without $CuCl_2$, and (B) 0.9% with $CuCl_2$ [Source: (23)] .

this is most likely the reason why the permittivity increases with the CB content.

More interesting are the *A* samples, prepared without the addition of salts. For a volume fraction of CB less than or equal to 0.9%, the particles repel each other and try to move as far away as possible to decrease their potential energy of interaction. This electrostatic stabilization prevents the formation of clusters and thereby leads to a small correlation length and to a low permittivity. Nevertheless, by increasing the volume fraction of CB, the particles must reach a closer position. Exceeding this critical value of CB content leads to composites with “high” conductivity. This high value is, in fact, comparable to the one obtained with a strongly agglomerated composite (type *B*) with an equivalent CB content indicating an analogous degree of formation for the percolating network.

In summary this material changes singularly, with a variation of CB content of only 0.03%, from a good insulating behavior with a low permittivity (comparable to that of the pure matrix) to a rather good conducting behavior equivalent to that of a totally agglomerated composite. It is evident that such an evolution should be related to an important modification in the filler arrangement within the polymer host. If true, this assumption should induce a strong variation in the microstructure of the composites.

3.1.6 Verification through characterization at meso scale

To verify the existence of an abrupt change in the microstructure of the material, optical micrographs on the edges of thin polished sections of the cured materials were taken.

The micrograph Fig. 3.6-B shows a sample with addition of salt, containing 0.9% of CB. In this case all the carbon particles are agglomerated leading to large particle free areas. This is in agreement with the previous study that showed that a strong agglomeration always occurred in the *B* samples, even for much lower CB contents. In fact, the microstructure of the *B* materials cannot be compared to the one obtained with a random occupation of sites of a given lattice, and therefore its behavior cannot be compared directly with a statistical percolation.

The second picture (A1) corresponds to the same volume fraction of 0.9% of CB, it reveals evenly distributed CB particles and, as expected, no visible clus-

ter formation took place in the composite. Examination of varied spots in the samples revealed a very homogeneous microstructure.

On the contrary, for a volume fraction of CB of 0.93% just above the measured conduction threshold, an aggregation phenomenon can be observed leading to an inhomogeneous distribution of the filler in the material. Indeed, particle-free areas and enriched zones, which favor the electrical conduction, can be seen on this picture. However, the hardening of the epoxy resin stopped the process before all particles where agglomerated and both aggregated and dispersed areas can be found in this sample by varying the observed area.

The last picture (A3), obtained for a volume fraction equal to 0.96% of CB, shows a highly structured network, similar to the one obtained for samples type *B* and thereby explaining the equivalent conductivity measured on these two kinds of samples. This agglomerated structure is found in the whole sample.

These observations were in very good agreement with the electrical measurements and largely confirmed that insulating composites are related to a dispersed state of the fillers while conducting composites should be associated with an agglomerated state of the fillers. These pictures contributed, thereby, to explain the abrupt conduction transition measured in the type-*A* composites.

3.2 Control at the meso scale

This section reports the changes induced on the above described composite (carbon black (CB) in epoxy resin) by application of a static electric field during the curing process. The primary goal was to validate the presence of electrical charges on the surface of the particles. The growth of dendrites from the anode into the material was observed in situ by optical transmission microscopy. In addition, a percolating network was seen to form, combined with a drastic reduction in the sample resistivity. This behavior could also be explained by taking into account the electrostatic interaction of the charged CB particles. It is further demonstrated that the final resistance of a composite with a given CB content can essentially be controlled within a range of about seven decades by varying the applied voltage and the curing temperature of the mixture.

3.2.1 Introduction and goal

The agglomeration process of carbon black (CB) dispersed in epoxy resin was described in the former section using a model based on the colloid theory⁽⁸¹⁾. It was assumed that the carbon black particles were charged during the preparation process. An electrostatic particle-particle interaction was held responsible for this singular percolation behavior. Two competitive forces, namely, the short-range van der Waals attraction and the long-range Coulomb repulsion presumably controlled the microstructure of the composite while curing. Below a critical volume fraction of 0.9% CB, the Coulomb repulsion prevented the formation of clusters. In other words, the dispersion forces overcome the van der Waals attractions, and the dispersion is electrostatically stabilized. We speculated that the particles repelled one another to reduce their interaction energy. For particle volume fractions above the critical value, a dramatic increase in the conductivity was evidenced.

The goal of the present section is to obtain direct evidence for the charge on the CB particles. Therefore, a microscopic observation method was developed for directly imaging the agglomeration process. To force the agglomeration, it is proposed to apply an electric field on the samples during the curing of the epoxy.

3.2.2 Evidence for agglomeration

In order to apply the electric field, the extremities of a Glass slides were sputtered with silver paint to act as electrodes, Fig. 3.7. The two electrodes were prepared by about $500\mu m$ which also permitted investigations with an optical microscope. The previously dispersed CB-epoxy mixture was placed on the glass slides and observed in between the electrodes, Fig. 3.7.

To monitor the resistance during the curing process, the voltage was applied by means of polished brass parallel plates dipped into the dispersion.

Fig. 3.9 shows the plot of the current versus time during curing of the 0.12% CB-epoxy dispersion used for the optical microscopy. A voltage of 30V was applied between the strip electrodes. This voltage resulted in an electric field close to $60 V/cm$.

At the beginning of the curing process the CB was evenly distributed, and no cluster formation was noticeable. After about 5 *min* the first clusters started

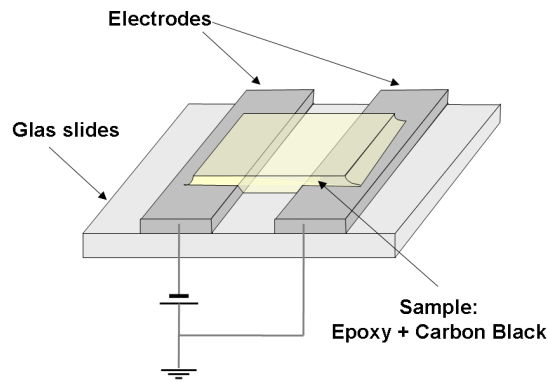


Figure 3.7 : Schematic representation of the experimental procedure

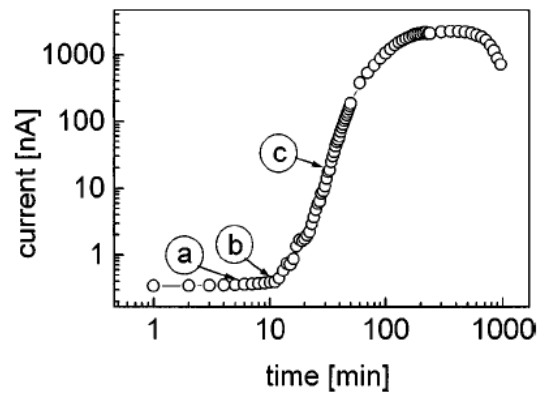


Figure 3.9 : Electric current versus time for a CB content of 0.12% and an applied voltage of 30 V [Source: (84)] .

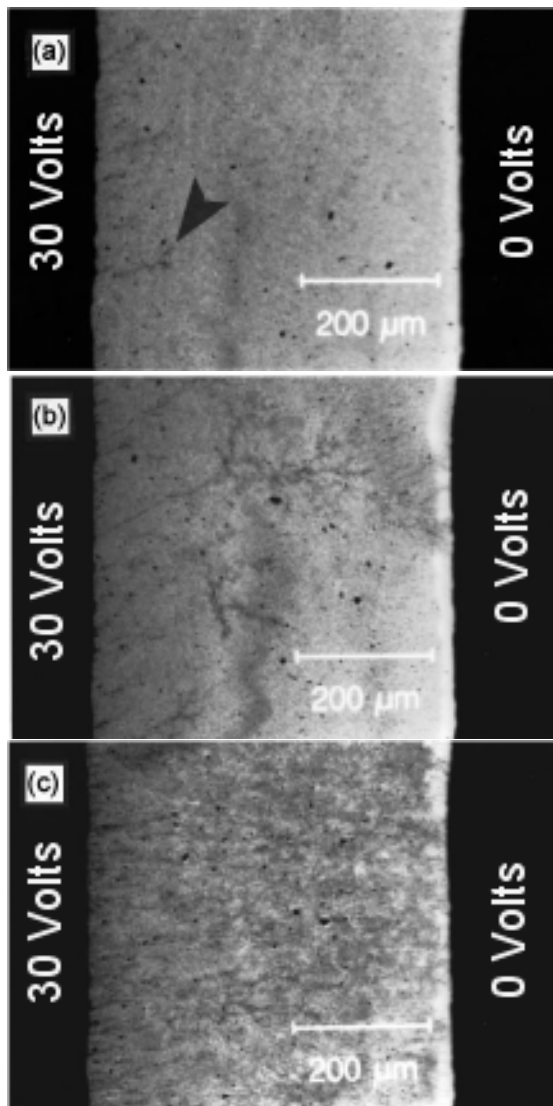


Figure 3.8 : Transmission optical micrographs taken after 5, 12, and 40 min corresponding to the positions denoted by a, b, c [Source: (84)]

to appear at the anode (left side of Fig. 3.8a), indicating a negative charge on the CB. At this stage, the current remained however at its initial value. A percolating cluster formed after about 12 min, Fig. 3.8-b. At the same time, a sharp increase in the measured current was observed, Fig. 3.9. Fig. 3.8-c shows the network after 40 min. At this stage, the network formation was still ongoing and the current through the sample was increasing. After about 100 min of curing the viscosity of the epoxy resin increased and the structure became frozen with the current reaching its maximum which was about four orders of magnitude higher than the initial value.

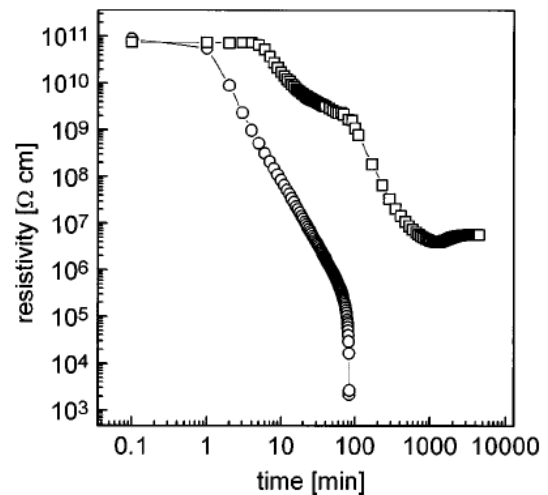


Figure 3.10 : Electrical resistivity for a CB content of 0.6% and applied voltages of 30 V (\square) and 60 V (\circ) [Source: (84)]

3.2.3 Effect of applied voltage

Fig. 3.10 shows the time dependence of the sample resistivity at room temperature with the same amount of CB, 0.6%. Two different Voltages of 30 and 60 V were applied, and the corresponding electric field reached 50 and 100 V.cm⁻¹, respectively. The initial resistance of the samples can be attributed to the residual conductivity of the epoxy resin⁽⁸²⁾. With 30 V, the resistance remained constant up to 5 min after applying the voltage. Then a sharp drop was due to the formation of a percolating network of CB particles. This again was consistent with the microscopical observations. After about 300 min, the sample hardened and the resistivity reached its minimum value.

The initial resistance with 60V was similar, but after just one minute the resistivity began to decrease indicating a faster formation of the percolating network. After about 60 min the current reached a value of 2 mA which was sufficient to heat the sample by Joules effect. The temperature increased reducing the viscosity of the epoxy resin. The lower viscosity permitted the CB particles to move and aggregate further, decreasing the resistivity. This positive feedback of this process induced an “avalanche” behavior, and the experiment had to be stopped after 100 min. A comparison of the conductivity with the results indicated in the previous section (about 2000 Ω.cm) indicated that virtually all the CB particles had aggregated onto the network. The application of the electric field was thus as efficient as the addition of salt to alter the interactions between the particles.

3.2.4 Effect of temperature

Fig. 3.11 shows the effect of temperature on this resistivity-time measurements, for a given voltage of 30V. Two temperatures were chosen 28 and 38°C. CIBA GEIGY⁽³⁸⁾ reports a large decrease in the viscosity of this materials in this temperature range before curing. The 28°C sample was similar to the one described above in Fig. 3.10, the results were quite comparable.

At 38°C a lower initial resistivity of the epoxy resin was evidenced. Furthermore, the decrease in the resistivity took place in the very beginning of the experiment indicating a rapid formation of a percolating network. This illustrated the considerable influence

of temperature and thus the viscosity on the agglomeration dynamics of the CB particles.

Hardening obviously occurred earlier at 38°C than at 28°C. Nevertheless, the 38°C curve reached a resistance which was about 100 times smaller than that measured at the lower temperature. In both cases the agglomeration process, and thus the final resistivity, were limited by the onset of the hardening process. The later comment becomes evident by comparing the final resistivities with those obtained with 60V Fig. 3.10.

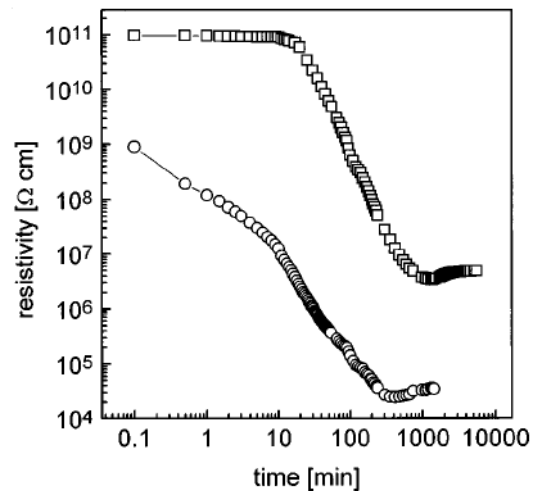


Figure 3.11 : Electrical resistivity for a CB content of 0.6% and applied voltages of 30 V(□) and 60 V(○). [Source: (84)]

Overview

The experimental results can be explained by considering the interaction between the charged particles and the external electric field. Assuming a CB concentration below the critical value of 0.9% due to the electrostatic repulsion of the particles, no cluster formation took place without the electric voltage.

The application of a voltage made the particles move toward the anode. This proved that the CB particles were indeed charged, with an overall negative value. It is speculated that the “charging” took place during the sample preparation and that the particles lost their permanent charges when agglomerated on a cluster linked to the anode. The next particles on the growing network drained off their charge directly at the tips of the CB clusters, where the electric field is most important. Dendrites-like structures

grew within the volume of the material. With the formation of the first percolating cluster a characteristic increase in the measured electronic current occurred. When the process was fast enough, no curing restrictions took place and all CB particles are incorporated in the network.

The dynamics of the agglomeration process can be described as a sensitive balance which depends on the electrostatic interaction of the particles with the external electric field and the viscosity of the epoxy matrix. This process was considerably influenced by the sample preparation, the value of the applied voltage and the curing temperature.

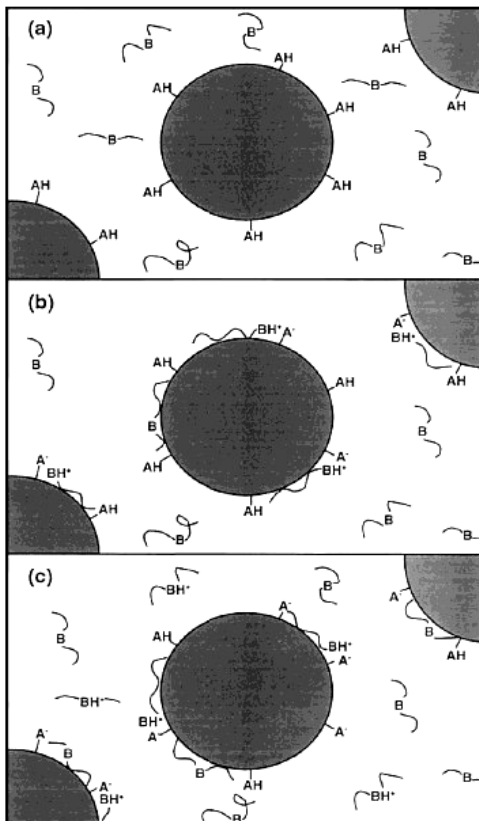


Figure 3.12 : Proposed mechanism of electrostatic charging of the CB particles (with acidic sites AH) by polymeric dispersants (with basic sites B), from Prasse *et al.* (85)

3.3 Conclusion

This work has dealt with ac and dc electrical properties of strongly contrasted binary mixtures made of an epoxy resin and CB particles. The experimental results showed a marked difference with the predictions of the statistical percolation theory describing randomly dispersed fillers. The measurements

could, however, clearly be related to a non random microstructure observed by transmission optical microscopy. The dynamics of the filler in the epoxy resin during the curing process, responsible for these microstructures, could be qualitatively explained with the help of the concepts of colloids.

The low dielectric constant in the vicinity (but below) the conduction threshold in the case of the composites *A* indicates clearly that no cluster formation takes place just before the transition. This can be understood by the electrostatic stabilization of the particles. An abrupt phase transition at a critical volume fraction of 0.9% could be explained as a consequence of a transition in the filler arrangement within the matrix. The critical value of CB content separates, in fact, a dispersed and an agglomerated state and can therefore not be compared with the one obtained through a purely random geometrical process.

This work confirms the necessity of accounting for the structure formation for the understanding of the percolative behavior of such binary mixtures. In the present study the CB particles have permanent electrical charges at their surfaces. It is, however, not certain that this phenomenon, particularly striking with the present composites, does not exist in other kinds of heterogeneous materials.

In addition, a new method for preparation of conductive CB-epoxy composites with a low CB content of 0.12% was reported. The method allowed adjustment of the final resistivity of composites with a given CB volume fraction within a range of about seven decades by varying the applied voltage. The growth process of the CB clusters was verified in situ by optical microscopy. In addition, we point out the possibility of preparing a material with a spatial inhomogeneous conductivity by applying the voltage to patterned electrodes during the curing process. The later method has since been patented (86;87).

Finally, it should be emphasized that, although the present results seemed in disagreement with the statistical percolation theory, the reason for the “failure” is not related to the theory itself. On the contrary, the understanding of the agglomeration process was related to the theory. In one word, the answer to the question “Percolation failed?” is **NO**.

Part II

Insulating fillers

Macroscopic description of the dielectric breakdown

The safe operation of high voltage electrical energy transmission grids depends on the reliability of its components, as switchgears, power transformers and gas insulating lines. Their reliability primarily depends on the performance of the insulating structures they contain. Nowadays, the dimensions of these equipments are tentatively being reduced, mainly for economic reasons. The size reduction also implies changes in the heat density and actual electric field for a given voltage. The insulating materials should thus have the best possible initial properties including a high dielectric strength and required thermo-mechanical properties.

These properties should limit some short-term breakdown mechanisms, distinguished in three main types:

1. Electrical breakdown: this is a very fast mechanism which is not preceded by a raise in temperature⁽⁸⁸⁾. The changes in the structure results directly from the action of the constraints due to the electric field. Two theories have been proposed to explain the electrical breakdown. The first one (called “intrinsic breakdown”) considers that the breakdown occurs when instability of the electronic current appears in the dielectric^(88;89). According to the second theory (called “breakdown by avalanches”), the breakdown criterion is assumed to be the electric field for which the electronic multiplication process reach inadmissible proportions. The material ceases to be a dielectric and becomes conducting.
2. Thermal breakdown⁽⁹⁰⁾: it is due to a thermal imbalance. It is connected with the energetic losses resulting from the mobility of the polar systems^(88;89;90;91). When an electric field is applied, the existence of charge carriers in the insulating material induces the appearance of a conducting current which can lead to the heating

of this insulator by Joule effect. However, this current is not the unique source of the heat. The relaxation phenomena that occur with composite submitted to an alternative field can also engender losses (called dielectric losses) which further contribute to the heating. If the heat is not evacuated as fast as it is produced, the temperature in the insulating sample increases at a rate that depends on the amplitude and frequency of the applied voltage. This thermal instability, induces structural changes within the dielectrics and favors its destruction.

3. Electromechanical breakdown: it results from the conjugation of two types of constraints: electric and mechanics. When the insulator is submitted to an electrical field, the electrostatic pressure due to the mutual attractions between the electrodes can reduce its thickness by a mechanical deformation^(92;93). If this electrostatic pressure is sufficient to produce a considerable deformation, the electrical field will be reinforced. It results in a reduction of the dielectric strength and can lead to breakdown.

Among the insulating materials, epoxy based composites⁽⁸⁸⁾ are widely used for these very demanding applications because of their ability to withstand high electric fields, which limits short-terms breakdown. Nevertheless, the resulting multiple stresses (electrical⁽⁹⁴⁾, mechanical and thermal but also environmental) in operating conditions might result in large modifications of the insulator over time^(88;95;96;97).

The later might lead to the initiation of partial discharges and electrical trees resulting in the breakdown of the insulator. The partial discharges result from local enhancements of the electric field within the inclusions or gaseous cavities which can be present in the material. They appear when the applied voltage reaches a threshold value corresponding to the

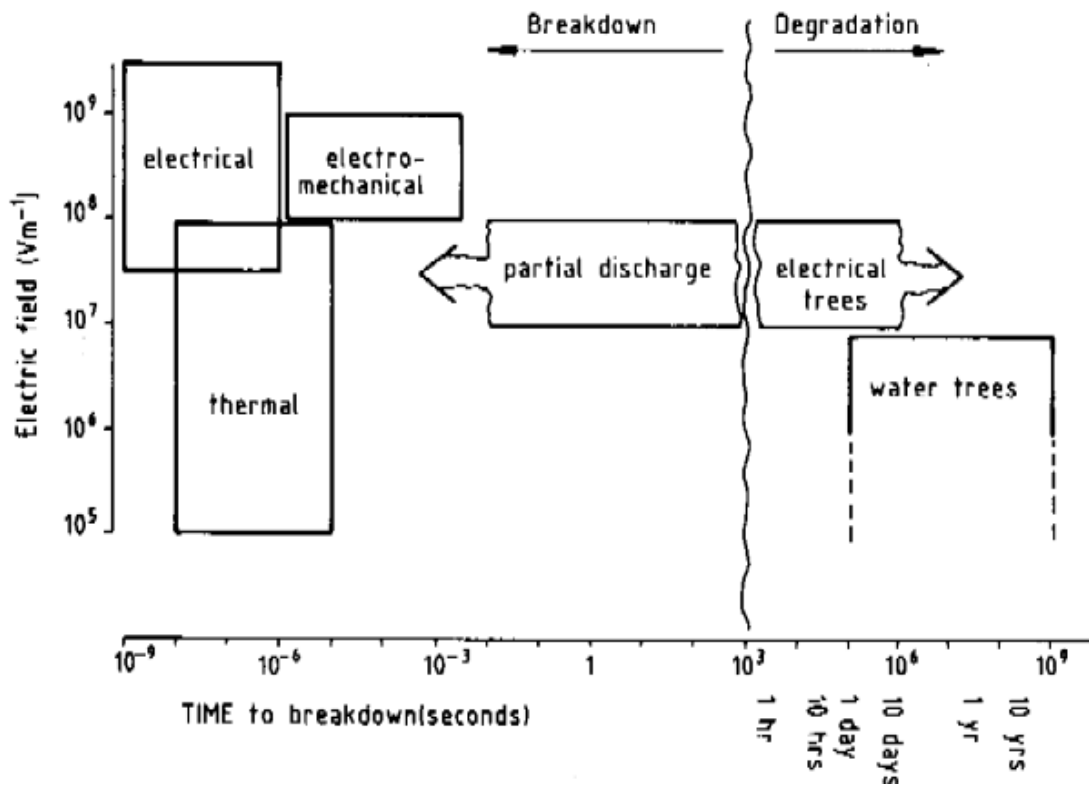


Figure 3.13 : Degradation and breakdown mechanisms as a function of time and electric field⁽⁸⁸⁾.

Paschen minimum of the gas in presence (air or others). Their action can lead to chemical and radical transformations (*i.e.* scission of the molecular bonds under the electronic and ionic bombardment, local heating or creation of radicals) leading to the failure of the material in consequence of mechanisms such as the propagation through the material of microscopic channels, the cumulative heating due to the discharges. The partial discharges lead to the initiation of electrical treeing. Each irregularity (protrusion) at the insulating wall (interface) of a cavity (void) favors the fast propagation of treeing and lead to the breakdown.

Loffelmacher⁽⁹⁸⁾, in 1976, linked the partial discharges to the electrical breakdown of epoxy composites. In this description of the electrical tree growing, the initiation is done in front of the needle electrode by partial discharges, leading to the creation of a channel. The gaseous decomposition products of the destroyed material raise the pressure and the density of the channel. It was noticed that the gas pressure in the partial discharges channel can exceed 1.2×10^7 Pa (120 bars). Then the combination of electrical and thermo-mechanical stresses allows the tree to grow, up to breakdown.

It is then of a major interest to understand and to predict the structural changes of these kinds of materials when submitted to tough conditions for long periods of time and, more specifically, the influence of these changes on the dielectric strength.

In operating conditions, because of the low thermal conductivity of polymer network in epoxy based composites, the application of high electric field induces temperature overshoots leading to thermal aging^(88;99). Two cases have to be considered depending on the temperature reached:

1. If the temperature T remains below the glass transition temperature T_g ($T < T_g$) over a long time, the so-called physical aging of the amorphous phase occurs, resulting in a densification of the polymer network⁽¹⁰⁰⁾. Beyer *et al.*⁽¹⁰¹⁾ and then Dissado *et al.*⁽⁸⁸⁾ suggested that this phenomenon could also be induced by the electric field.
2. If the temperature goes beyond the T_g of polymer, chemical degradations such as chains scissions, formations of radicals and polar groups, recombination of chain segments^(95;102;103;104)

will most likely happen within the polymeric network. Under electric field, these free radicals or dipoles could induce both (i) a conduction current leading to further overheating of the insulator by Joule effect. The insulator could this way, following a cumulative process, reach critical temperatures locally and prematurely undergo breakdown by the thermal mechanism⁽⁸⁸⁾. A gradual ionization (ii) of the material could also occur, accelerated by ions resulting from the degradation and leading to breakdown by an avalanche mechanism⁽⁸⁸⁾.

It is worth noticing that “rejuvenated” samples refers to sample that first underwent a physical aging before being heated above the glass transition temperature. The latter treatment permits the polymer to reorganize back to a thermodynamic equilibrium. With the composites under investigation, this also induced a chemical rearrangement of the degraded species.

Few investigations have been reported on the influence of the physical aging on the breakdown field or dielectric endurance of composites. Under high electric field, Dissado⁽⁸⁸⁾ mentioned that the increase in local density accompanying the physical aging could lead to strains generated formation of microvoids that should act as flaws. This author forecasted that the physical aging could hence facilitate the electrical degradations in the form of partial discharges similar in nature to those observed in semi-crystalline polyethylene. On the contrary, Champion and Dodd⁽⁹⁶⁾ have studied the effect of this physical aging on the tree growth of unfilled epoxy anhydride networks. These authors have, in particular, established that the fractal dimension of trees increased with the materials age. For a large variation in aging times, they even observed a transition from filamentary-like to a bush-like structure of the damage tree. The authors concluded that the density increase associated with a reduction of internal stresses during the structural-aging process modified the electrical properties of epoxy networks. This interpretation has been confirmed by Auckland *et al.*⁽¹⁰⁵⁾.

Chapter 4

Simulation of the Breakdown at a mesoscopic scale

⊙ **Abstract** ⊙

Observations of damage patterns resulting from dielectric breakdown experiments of insulating materials show a large variety of breakdown trees. In the case of heterogenous systems, the damage structures are even expected to be more complicated. To understand the interdependence between tree morphologies and geometrical arrangements of the two phases, several numerical methods, based on the resistor-short breakdown model, can be found in the literature. Nowadays, these models are being developed to understand the influence of the fillers on the dielectric breakdown, including, for instance, the so-called “barrier effect”. It is also the aim of the present section which is specifically devoted to linear breakdown. However the general approach presented might involve numerous extensions namely description of interfacial polarization effect and non-linear resistive or capacitive elements. These future developments could concern both homogenization and breakdown issues.

Contents

4.1	Introduction	48
4.2	Case of isopotential particles	48
4.2.1	-Approach	48
4.2.2	- Results with a single short per step	49
4.2.3	-Distribution in Breakdown criteria	50
4.3	Case of non - isopotential particles	51
4.3.1	Mesh generation	51
4.3.2	From continuous to discrete values	51
4.3.3	Results	52
4.4	Conclusion	52

4.1 Introduction

The present chapter is specifically devoted to the modeling of dielectric breakdown in epoxy based heterogeneous systems. The dielectric breakdown of these materials occurs by means of narrow discharge channels that exhibit a strong tendency to branch into complicated patterns (88;106). The damaged structure might present a variety of shapes that depend, for instance, on the nature of the electrical field(96).

In the case of homogeneous solids, several statistical models have been developed to describe the breakdown patterns(107).

The case of heterogeneous systems is, however, more complicated because of the field enhancement which develops between phases with contrasted permittivity or conductivity. When a classical epoxy based composite material is subjected to an electric field a quite large enhancement might occur, especially on surfaces nearly tangent to the field or on sharp angles. These singularities might lead to the initiation or the ease of propagation of breakdown trees.

Because the damaged tree (with epoxy matrices) presents a much lower resistivity than the initial undamaged material, the propagation is a cumulative process in which each step strongly depends on the former ones. This particularity makes beneficial the use of a voltage controlled resistor-short breakdown model(108). In this model, the composite structure is described by a resistor network where the center of mass of each particle is a node connected to its closest neighbors by a resistor. These resistors are then supposed to irreversibly short to good conductors when the current reaches a threshold value. The strong positive feedback of this model gives roughly one-dimensional breakdown trees(108).

4.2 Case of isopotential particles

4.2.1 -Approach

For this first simulation an arbitrary Ohm unit was defined for a unit of length. Each particle was connected to its 18 closest neighbors with a purely ohmic resistor. Before the electrical response of the circuit could be determined, measurement elements were added to the equivalent circuit, namely (i) an electrode linking the bottom nodes, (ii) a tension source between the earth and the top middle particle and (iii) a short

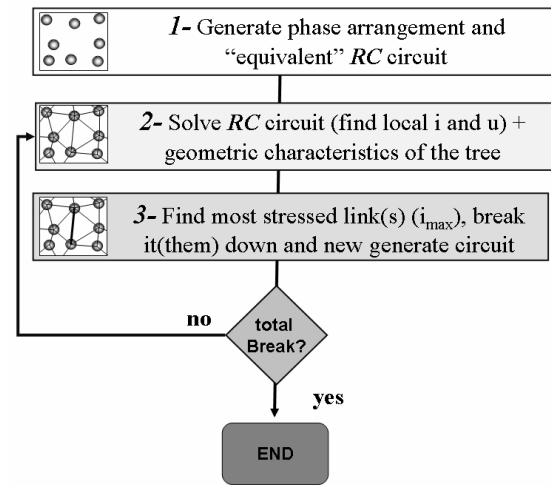


Figure 4.1 : Methodology utilized to determine the breakdown field [Source: (109)]

between the earth and the bottom electrode. This method is thus very similar to that employed in the Chapter 1, see Fig. 1.2. The electrodes consist of resistors with very low values ($10^{-15}\Omega$). The left and right side of the network were affected with a high value of resistivity corresponding to Von Neumann boundary conditions¹.

Two combinations of elements can then be employed, namely: (1) with both bottom and top electrode added to the mesh, this boundary conditions representing a macroscopic homogeneous electric field and (2) with only one of the two electrodes giving a pin-plane configuration comparable to the standard experimental measurements in divergent field.

The simulation is performed using a sequence of calculations with spice 3f5(42) and in-house codes. A unit voltage is applied to the network and Kirshoff's laws are solved to find each node's potential. The current flowing in every link is then determined and the most stressed link is registered and considered as definitively short. This maximum current is then divided by the short current, giving a meso-macro enhancement ratio. The applied voltage then is divided by this factor to establish the applied voltage V_s at which the most stressed resistor will short. This hypothesis obviously corresponds to the particular case of linear (ohmic) resistors. Once the most stressed resistor has been shorted, the new equilibrium potential is computed, the "hottest" node(108) found, shorted,

¹The von Neumann conditions basically mean that no current can either enter or get out the edges.

etc. until a conducting path has gone through the entire simulated composite. It is worth pointing out that the dielectric breakdown simulations are entirely deterministic in nature and that no random number generator was employed for the calculations.

4.2.2 - Results with a single short per step

A honeycomb structure was primarily chosen, because it reflects a particular case in which each particle is placed at a constant distance from its neighbors. As the resistor value between two nodes, i and j , was taken proportional to the distance, D_{ij} , between the two centers of mass⁽³⁹⁾, this first case leads to a network with initial equal value for all resistors. The upper potential initially applied to a single particle induced a very strong field enhancement, which outlines the boundary conditions chosen in the Y direction (pin-plane), Fig. 4.2.

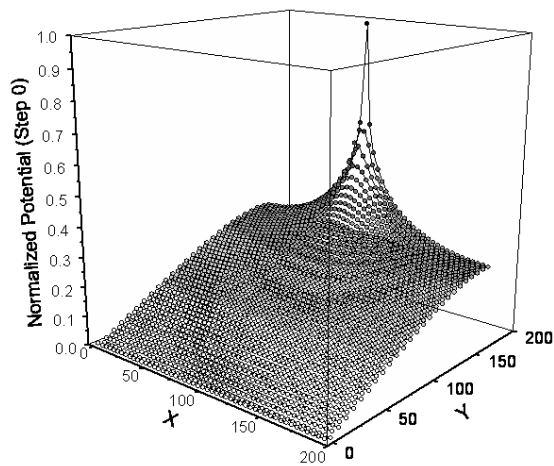


Figure 4.2 : Potential distribution on a regular mesh before any breakdown occurred. The units are arbitrary on every axis.

The subsequent large field enhancement induces an initially low voltage to short the first link. Once a few shorts have broken, the field enhancement decreased and V_s raised accordingly, Fig. 4.3. As a function of the number of steps, the macroscopic voltage to breakdown presented an inverted U-shaped curve that separated three regions. As already noticed by Martin *et al.*⁽¹⁰⁸⁾ this graph essentially separates on the one hand a region with a stable behavior, where the voltage has to be increased to maintain the propagation, and, on the other hand, an unstable tree where a given voltage would conduct to the final failure of the material, Fig. 4.3.

In the case of a plane-plan electrode configuration, the electric field is initially homogeneous and the opposite phenomena takes place. In the first step the development of a conducting tree within the sample induces a field enhancement and is beneficial to the growth of the electric tree. As a result, the beginning of the degradation directly leads to the entire breakdown Fig. 4.3.

Since the growing tree is assumed to be conducting² the macroscopic resistance of the samples tends to decrease with the cumulative damage taking place in the material.

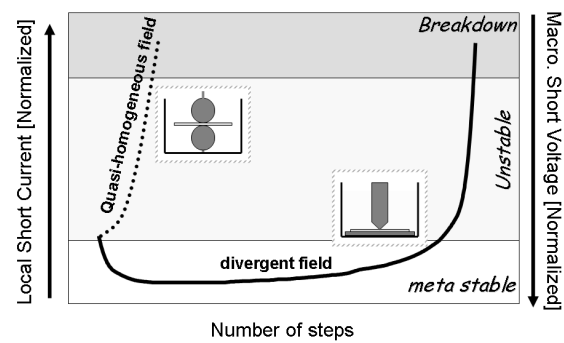


Figure 4.3 : Schematic representation of the macroscopic voltage (or local electric field) required to continue the breakdown propagation at each step of the simulation.

The field enhancement even became quite large when the tree had gone almost through the entire simulated structure, leading to the final breakdown, Fig. 4.3. It thus appears that this particular case, though trivial, already gave some physical hints. This simulation leads however to a straight-line breakdown tree (not shown) once the breakdown has gone through the entire structure. This could obviously not be considered as a representative description of a real system for, at least, two reasons. Firstly, a regular mesh represents a perfect arrangement of the reinforcing filler. Secondly, the field enhancement is supposed to produce a single short at the most stimulated link that leads to only one-dimensional trees in disagreement with the fractal structures generally observed on damaged samples.

²The damage tree was proved to be conducting in the case of epoxy matrix⁽¹¹⁰⁾. This is probably *not* the case for all polymers.

4.2.3 -Distribution in Breakdown criteria

Considering the previous results, the next step consisted in damaging an array with a disordered particle arrangement (whose coordinates were determined using a Monte-Carlo simulation⁽¹⁰⁸⁾). Moreover the short was not only applied to the “hottest” link but also to a given amount of the following ones. This hypothesis relates to the fact that even homogeneous materials exhibit short current fluctuation being held responsible for fractal breakdown structures^(107;111;112).

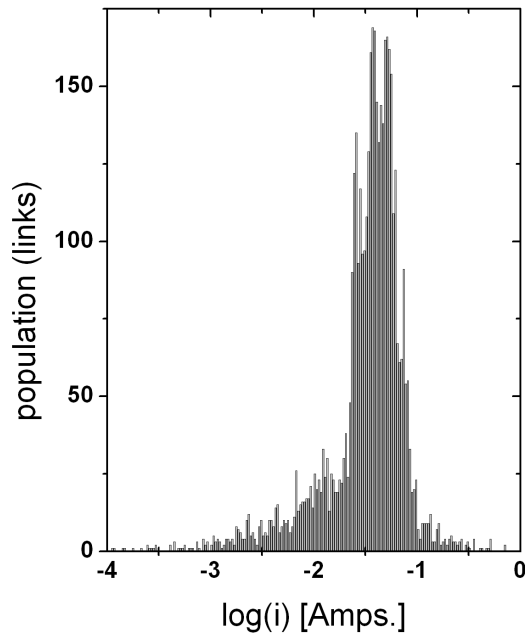


Figure 4.4 : Distribution in current in the links during the breakdown process.

This feature was introduced into the simulation through a parameter δi , which describes a distribution in short current. If i_{max} denotes the current through the hottest link, each link subjected to a current greater than $i_{max} * (1 - i)$ was then supposed to short, Fig. 4.4. Following this definition, the first case described in this section corresponded to $\delta i=0$, and increasing δi increases the number of new shorts at each step. This parameter induces a tree with a more branched pattern but the simulation does remain entirely deterministic and based only on the phases' topology.

It appears now of interest to describe the influence of this parameter δi on the shape of breakdown tree.

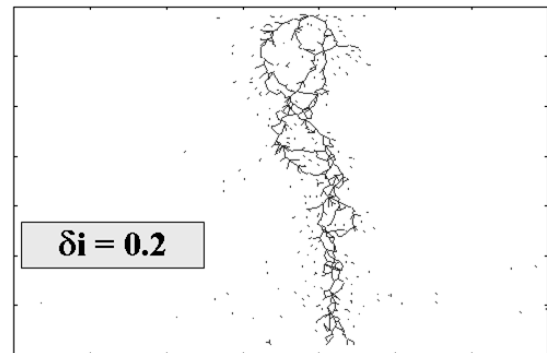
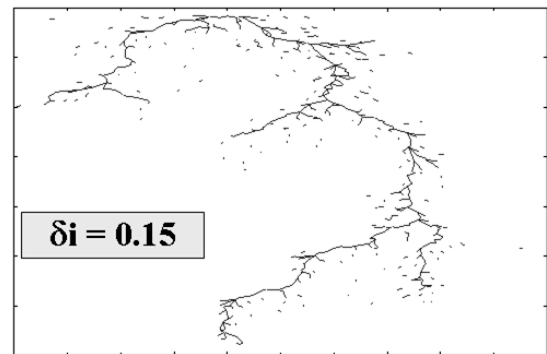
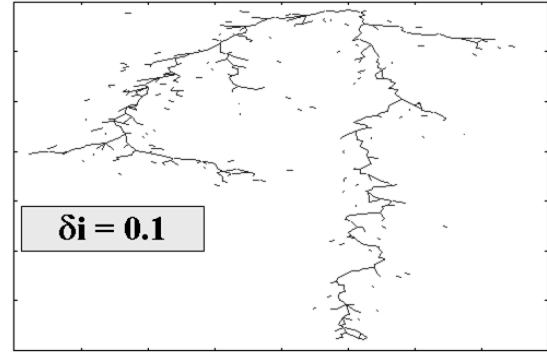
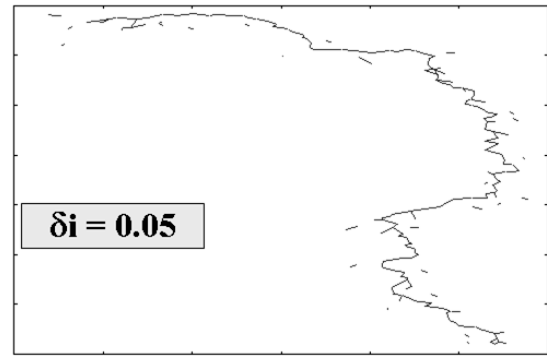


Figure 4.5 : Influence of δi on the breakdown pattern (see text for details) [Source: (113)] .

These simulations illustrated a progressive transformation from a tortuous to a straight pattern⁽¹¹⁴⁾ that

is comparable in nature to the tree-to-bush transition described in the literature⁽¹¹⁵⁾, Fig. 4.5. This second type of modeling was thus an improvement as compared to the former one. It still exhibits, however, three strong intrinsic drawbacks:

1. it does not account for any geometrical feature within the material, including the real distance between particles,
2. each particle is reduced to its center of mass, which forbids any dependency upon volume fraction of inorganic filler, and,
3. each particle is assumed to be isopotential

Statement (3) is obviously the most severe because the real field enhancement between two particles strongly depends on geometrical features between the neighbors as well as physicochemical property of the matrix in-between. Moreover, assuming isopotential particles contradicts experimental features like MWS effect. For these reasons, it appeared manifest that the simulation had to be run with non-isopotential particles. In other words, the mesh had to be refined.

4.3 Case of non - isopotential particles

4.3.1 Mesh generation

In order to develop a more realistic simulation, a finer mesh had thus to be defined that did not assume the particles were iso-potential. This was performed with the help of the ImageJ⁽¹¹⁶⁾ image analysis software. The required steps to achieve this are schematically depicted in Fig. 4.6:

1. The image was first binarised and the coordinates of the contours were then saved for each particle.
2. An unstructured mesh was created that contained the contours points.
3. The electrical properties were assigned to each phase using rigorous finite element discretization methods. This point is described below, 4.3.2).
4. Within this mesh it seemed reasonable to set two kinds of triangles representing either the matrix

or the filler, depending on their geometrical positions. These triangles were accordingly given different physical properties.

—— the procedure is then as in Fig. 4.1 ——

5. The boundary conditions (electrodes and Von Neumann) are added to this collection of resistors, a voltage difference is applied, and the system is solved.
6. the most stressed linked are assumed to be electrically shorted, the mesh is changed accordingly, etc.

This methodology thus allows, in few steps, getting an unambiguous set of resistors that closely relates the initial image.

4.3.2 From continuous to discrete values

Fig. 4.7 depicts the issue one faces when willing to determine the set of three discrete resistors that are electrically equivalent to a continuous triangle. This geometrical problem can be solved analytically (see appendix A in ⁽¹¹⁷⁾ for details)

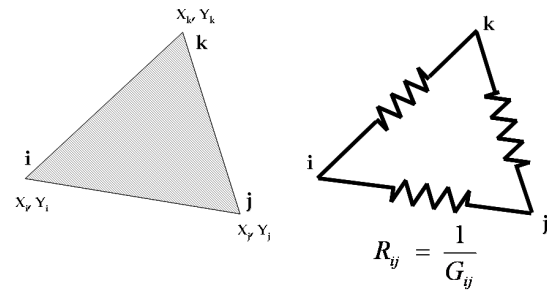


Figure 4.7 : Elementary method for construction of equivalent network⁽¹¹⁸⁾.

$$\begin{aligned}
 G_{ij} &= \frac{\sigma}{4A} \cdot (x_j x_k + x_i x_k + x_k^2 - x_i x_j \\
 &\quad + y_j y_k + y_i y_k - y_k^2 - y_i y_j) \\
 G_{ik} &= \frac{\sigma}{4A} \cdot (x_i x_j + x_j x_k + x_j^2 - x_i x_k \\
 &\quad + y_i y_j + y_j y_k - y_j^2 - y_i y_k) \\
 G_{jk} &= \frac{\sigma}{4A} \cdot (x_i x_j + x_i x_k + x_i^2 - x_j x_k \\
 &\quad + y_i y_j + y_i y_k - y_j^2 - y_j y_k) \quad (4.1)
 \end{aligned}$$

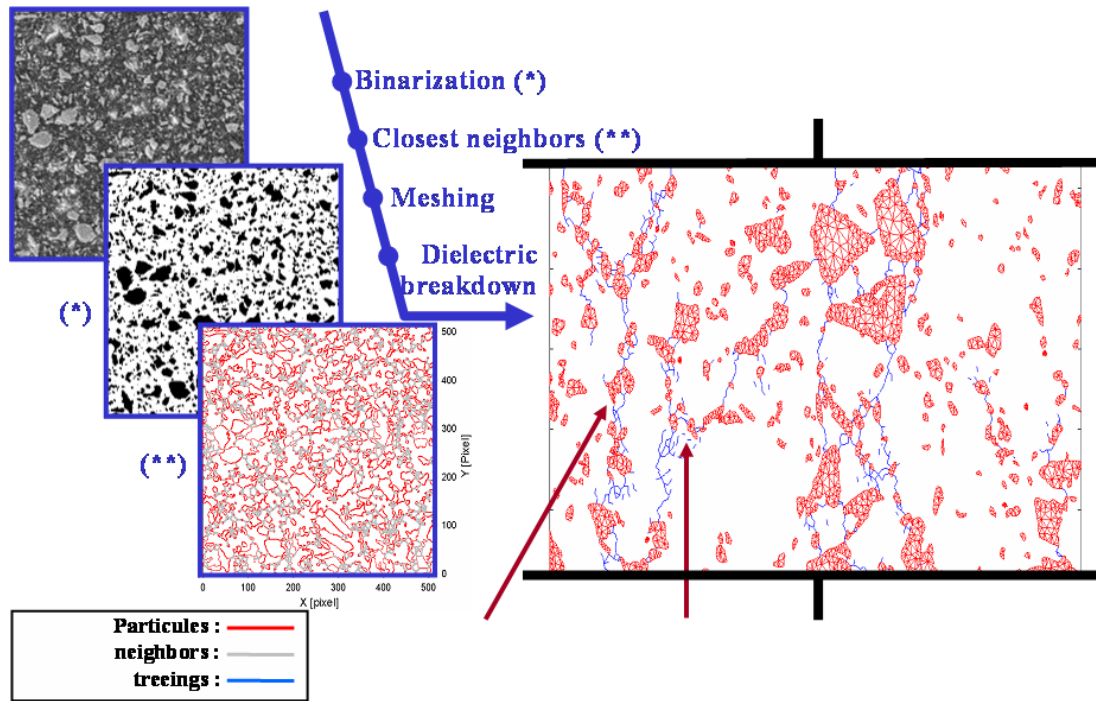


Figure 4.6 : The steps of simulation of breakdown trees in heterogeneous materials (case of a composite in a homogeneous field). Photomicrograph 2D, segmented picture, equivalent network (the elements corresponding to the matrix have not been plotted to improve clarity) and dielectric breakdown simulation [Source: (109; 114)] .

These parameters have the units of conductance; the finite element defined by nodes i, j, k can be replaced by three discrete resistors with values $1/G_1$, $1/G_2$, and $1/G_3$. The matrix for the entire system is thus equivalent to the discrete resistor network defined by the finite elements.

In the present case, the mesh was performed with “high quality” conditions, meaning that the angles of each triangle was greater than 28° . This condition, prevents biased results during the finite element analysis. As depicted on Fig. 4.8 the technique allows a good control of the mesh to fulfill various needs.

4.3.3 Results

A small example of the potential distribution is shown on Fig. 4.9. The difference in resistivity between the two phases was clearly identified on the potential graph, where the fillers appeared as pseudo-horizontal flakes inducing a strong field enhancement among particles, Fig. 4.9 and 4.10.

An example of a breakdown tree is described in Fig. 6 for the case of plane - plane electrodes arrangement, where the field enhancement is only due to the presence of the particles. This configuration showed a

strong correlation between the presence of the fillers and the propagation of the tree which mainly took place close to the interface. The asperity, even away from the main breakdown tree also showed a strong tendency to develop shorts that remained localized in this simulation (particles were supposed to have an infinite breakdown tree in this simulation).

The segments corresponding to the minimum distance between two neighboring surfaces were also plotted on this graph. It is interesting to note that the breakdown tree very often follows these segments, especially those oriented in the direction of the electric field (vertically). This consideration is of interest because it shows that a well-defined quantitative image analysis could be used as a tool to predict weak locations within a composite.

4.4 Conclusion

This chapter was related to the development of a numerical simulation well-suited for modeling the initiation and development of a breakdown tree. A deterministic model was developed that took care of the organization within real composites. The main features described in the literature both experimentally

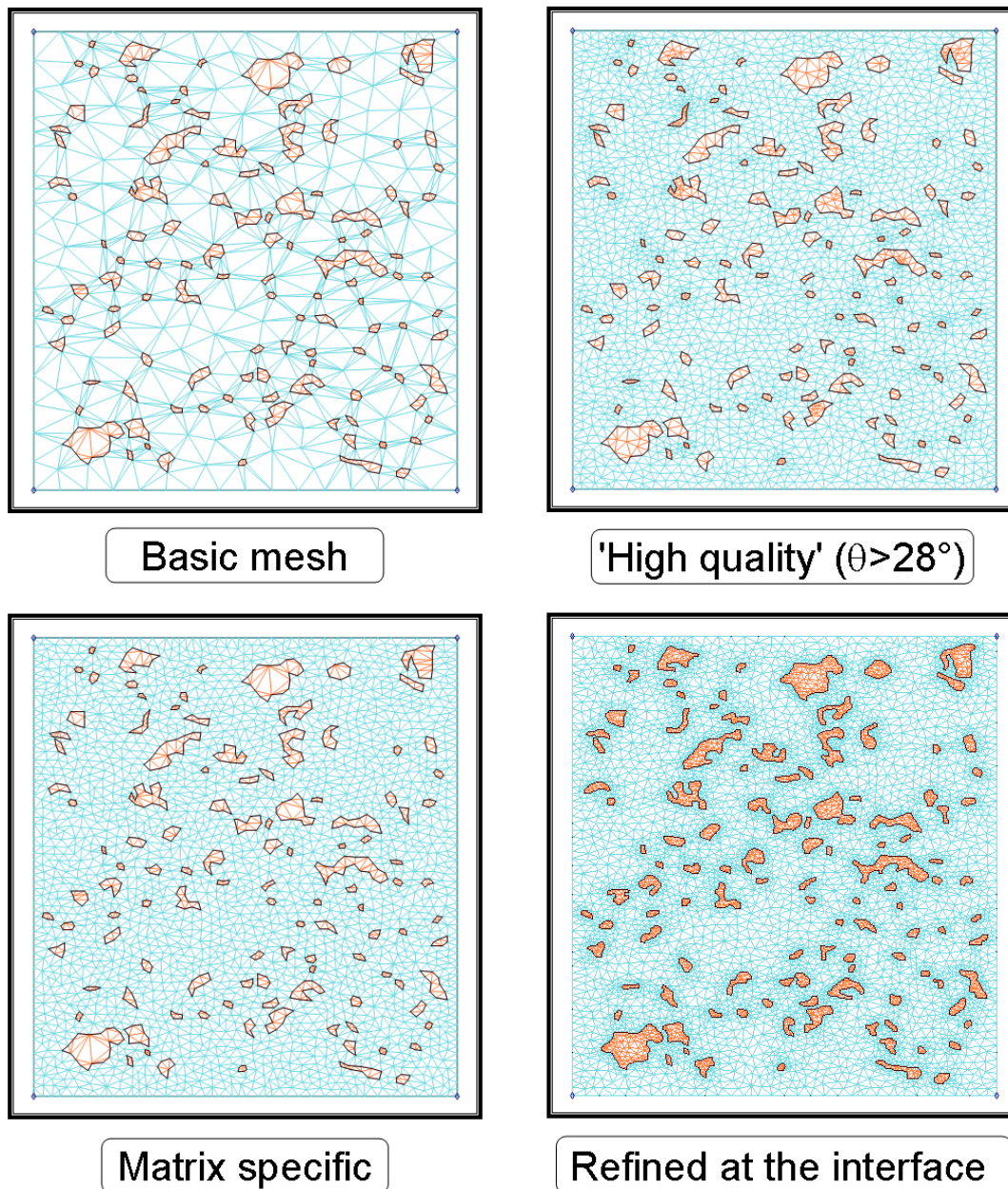


Figure 4.8 : Example of possible meshing conditions: rough mesh | mesh specific to the matrix | “High quality” mesh, useful for breakdown simulation | Interface refined mesh, suited for homogeneization purposes.

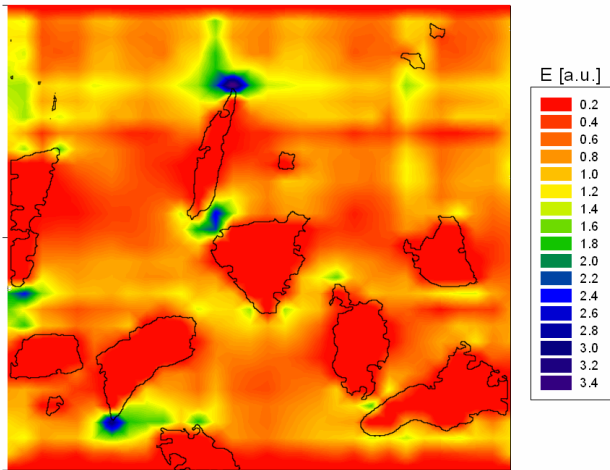


Figure 4.9 : Initial field distribution, case of a two-phase composite with a ratio of ten in their intrinsic conductivities in a macroscopic homogeneous field, before any breakdown. (109)

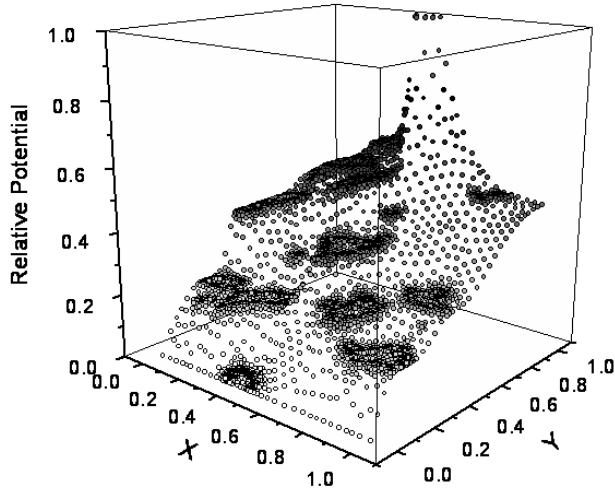


Figure 4.10 : Potential distribution after few breakdown steps, case similar similar to Fig. 4.9, but in divergent field after 5 breakdown steps. [Source: (109)]

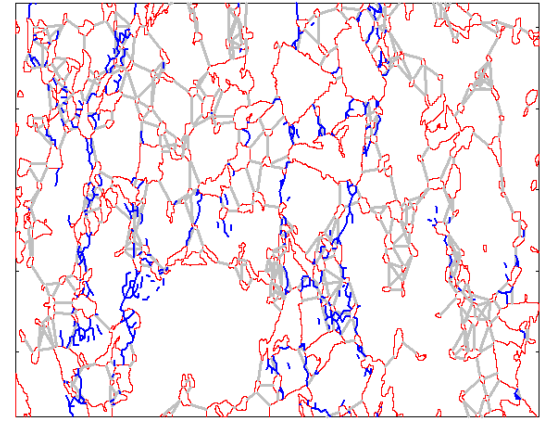


Figure 4.11 : Interrelation between minimum particle distance and breakdown tree (plane - plane electrode arrangement). [Source: (109)]

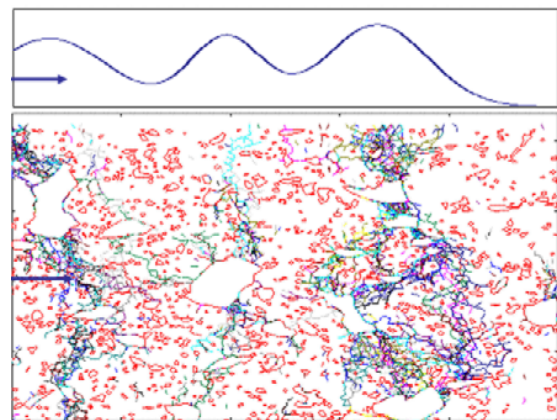


Figure 4.12 : Example of semi local parameter: the smoothed amount of particle enhancing the electric field (curve on top) correlates to the weakest point in a composite revealed by 20 independent calculations.

and numerically were primarily recomputed to validate the methodology. In addition a model directly based on real pictures of the sample was utilized. The present targets are now to develop codes that take care of other electrical features observed in polymers and composites. In particular, more representative physical conduction mechanisms and breakdown conditions for each phase (including interface and other phase like porosity, etc.) will be presented in the future. In addition the code will be modified by comparison to experimental results to better describe the scale at which damage really occurs. It seems thus possible to understand the polarization effects that develop at the interface and to compare it to experimental measurements under low electric field. The most important point seems however to raise from a comparison between quantitative image analysis and position of the breakdown tree. Our long term goal is to develop a tool that predicts the geometrical position of the weakest part of a composite with the help of (i) local parameters, like radius of curvature of the particles (ii) semi local parameters (see Fig. 4.12), like distance between particles and (iii) macroscopic parameters like the intrinsic properties of each phase.

Chapter 5

Process/structure/high voltage property relationships

⊙ **Abstract** ⊙

This chapter describes both an experimental study and the application of the above described numerical investigation of the breakdown field in particle reinforced thermosets. On the same given industrial piece, DSC experiments revealed a large dispersion in T_g , ΔT_g , and ΔC_p . The thermal parameters were, however strongly correlated in the statistical point of view. It is shown that the apparent dispersion in data was actually related to a sample's position with respect to the injection point in the mold. The resulting series of samples with different extent of cure were further tested for breakdown properties. A linear increase in dielectric strength was evidenced with increasing the conversion degree (α) of the epoxy matrix. In addition, it was observed that the presence of the second phase (mineral filler) dispersed within the polymeric host led to apparently contradictory results depending on the nature of the electric field. The neat matrix exhibited a higher field to breakdown than that of the composite in a quasi-homogeneous field configuration whereas the opposite behavior was evidenced in a point-plane configuration. It thus appeared that the filler can either increase or decrease the breakdown voltage, depending on the nature of the electrode configuration. The simulation described in Chap. 4 furnished the explanation for the apparent disagreement, showing that the inorganic particles protect the composite in divergent fields through a mechanism similar in nature to the so-called "barrier effect", whereas the same fillers were responsible for a local intensification of the electric field and thereby a reduction of the dielectric strength in a quasi-homogeneous field.

Contents

5.1	Introduction	58
5.2	Influence of the processing on completion of curing	59
5.2.1	Experimental	60
5.2.2	Results and discussion	62
5.2.3	Results overview	64
5.2.4	Conclusion	65
5.3	Influence of the micro and meso scales on high voltage properties	65
5.3.1	Experimental	66
5.3.2	Results and discussion	67
5.3.3	Concluding remarks	75

5.1 Introduction

When an organic insulator is submitted to an intense electric field, it is susceptible to undergo different kinds of degradation, occurring at different scales⁽⁸⁸⁾. This can occur through various mechanisms including, internal cavities parallel and perpendicular to the electric field, spherical cavities or via treeing⁽¹¹⁹⁾. These partial discharges can significantly damage the materials and are even susceptible, given enough time, to cause the insulator to snap and fall down. The degradations may result from the formation of field gradients, locally disruptive.

In the literature^(96;97;105;106;120;121;122), numerous macroscopic factors, such as temperature^(96;123), pressure⁽¹²¹⁾ and voltage frequency^(106;122) or amplitude^(96;97) have been identified as susceptible to induce changes in the formation of the dielectric trees. More precisely, these parameters might alter the shape and the size of trees as well as their propagation velocity. The qualitative and sometimes quantitative influence of each of these parameters taken separately on the damage of common insulating materials is thus rather well-understood nowadays⁽⁸⁸⁾.

Besides these “external factors”, different studies have been carried out on the influence, on dielectric breakdown, of more intrinsic properties of the materials such as their chemical nature. Most of these investigations focused on the impact of the amount and/or the nature of the second phase (generally mineral particles). Holboll *et al.*⁽¹²⁴⁾ and Wong *et al.*⁽¹²⁵⁾ have, for instance, demonstrated that for a similar fraction, alumina fillers induced a better prevention to the degradations generated by an AC electric field than the silica counterparts. This result was attributed to the higher thermal conductivity of alumina as compared to silica. Cho *et al.*⁽¹²⁶⁾ have analyzed the influence of the amount of alumina dispersed in epoxy matrix composites on dielectric breakdown in a point-plane configuration. They observed that the dielectric breakdown reaches a maximum for a fraction of alumina of about 5 phr (per hundred resin). The increase in dielectric breakdown when the fraction of alumina was varied from 0 to 5 phr was attributed to a “barrier effect”^(111;127;128;129;130) that is often invoked in the literature for diffusion and damage propagation phenomena. Further increase in volume fraction above 5 phr, penalized nevertheless the breakdown field presumably because of the increase in electric field at the polymer/fillers interfaces. The presence of

an optimum in the breakdown field clearly illustrates that at least two mechanisms are competing namely the barrier effect beneficial to the material and the “interface effect” which facilitates degradation.

Other studies were concerned with the influence of the fillers size on dielectric breakdown. For example, Fujita *et al.* and Henk *et al.* have shown that, the decrease in average inorganic filler size largely modified the electric behavior of epoxy matrix composites. Here again apparent contradictions were evidenced that seemed to originate from the damage mode. Using ramp-mode tests, Fujita *et al.*⁽¹³¹⁾ showed (with 40 phr alumina epoxy composites), that the dielectric breakdown increased when the size of the reinforcing particles decreased from 250 to 5 μm . With filler volume fractions above 100 parts, the opposite tendency was observed on the same composites. The author proposed that for an amount of 100 phr and with 5 μm fillers, the average inter-particle distance takes a value of 3.1 μm that becomes critical for the field gradients. Henk *et al.*⁽¹³²⁾ studied the influence of the fillers’ size on the electric endurance of epoxy matrix composites. They showed that an addition of nano-sized particles to a composite initially filled with micrometric particles, led to a surprisingly large improvement of the materials electric endurance. These authors proposed that the improvement was related to a better dissipation of the heat generated by the applied electric field, through Joule effect. Although the dielectric breakdown of solid state materials have been the subject of numerous investigations, surprisingly few studies were concerned with the influence of matrix characteristics on the dielectric damage of composites. The completion of curing of the matrix seemed, however, to be quite an important parameter. More specifically, it was demonstrated⁽¹⁰⁵⁾ that the post cure temperature and cooling rate notably alters the initiation and growth of damaged tree in unsaturated polyesters networks.

In summary, it is overall striking, when reading the literature on the dielectric breakdown of composites, that numerous contradictions arose from experimental results. These disagreements reflect the complexity and competition among the individual phenomena responsible for the macroscopic behavior. Some authors noticed and explained the apparent inconsistencies, but they also originated from different reports without further investigations.

The present study covers overall the separate influences of each phase (polymer matrix and mineral

filler) on the macroscopic behavior of an epoxy based composite. The large influence on dielectric breakdown of minor variations in conversion degree ($0.95 < \alpha < 0.99$) of the epoxy matrix in a heterogeneous material is first related. In a second step, differences in dielectric breakdown depending on the nature of the electric field (divergent or quasi homogenous configuration) are revealed. This study was performed both on the unfilled matrix and with a composite system based on the same matrix but filled with inorganic particle. It was observed that the presence of the second phase (mineral filler) dispersed within the polymeric host led, here again, to apparently contradictory results depending on the nature of the electric field. It indeed appeared that the filler can either prevent or ease the breakdown phenomena, depending on the nature of the measurement. In order to further understand the later result, a numerical simulation of the dielectric breakdown was adapted to the present problem. A deterministic model was developed that faithfully relates the actual organization within real composites. This numerical tool is mainly determinist in nature and based on simple, well accepted, physical assumptions. Few parameters are necessary, each of which presenting a straightforward physical meaning. The simulation furnished a clear explanation to the above described apparent disagreement.

5.2 Influence of the processing on completion of curing

In this section, Differential Scanning Calorimetry analysis was employed to investigate interrelationships between several thermal parameters and the processing conditions of particle-filled thermosetting resins. On the same piece, obtained by injection molding, the epoxy based composites exhibited sensible differences within a set of measurements of glass transition temperatures (T_g) and width of the transition (ΔT_g), as well as differences in heat capacity (ΔC_p) and conversion degree (α). A statistical analysis showed a strong inter-correlation between these thermal parameters but it could not provide any explanation for the disparities. The dispersion of the measured properties could, in a second step, be directly related to the sample's position as compared to injection point in the mold. It was additionally observed that even the post-curing stage could not erase

this topological effect. As a result, a phenomenological model is proposed that fairly describes the experimental trends. This simple polynomial approach can subsequently be used either to determine the thermal parameters of any point of the molded piece or to shed some light on phenomena responsible for the large variations of the measured quantities.

Introduction

The electric industry commonly employs epoxy-based composites as insulators for their ability to withstand large electric fields and mechanical stresses over long period of time. Besides imparting better mechanical properties and decreasing the price of the final product, the addition of mineral fillers to thermosetting resins is an old but efficient way to prevent the thermal degradation. Common inorganic fillers indeed reduces the epoxy overheat during curing by a dilution effect and because of the larger heat capacity and thermal conductivity of the fillers as compared to the neat resin⁽¹³³⁾. According to the literature, the performances of these materials seem to strongly vary depending on the nature of the constituents⁽⁸⁸⁾ and even within a given class of composites. The nature of the second phase (often a mineral filler)⁽¹²⁴⁾ and its topological arrangement are often invoked to explain variations in macroscopic physical properties^(126;132). It is furthermore well known and understood that the thermal history⁽¹³⁴⁾, the water adsorption⁽¹³⁵⁾ and the interface's quality^(136;137) strongly alter the glass transition temperature of these composites. The reason for the large variations within thermal parameters that can even affect apparently very similar samples remains, however, an opened question. Because it induces huge variations within the material's structure, the process could plausibly be held responsible for at least a part of this phenomenon. More specifically the curing stage in the hot mold, characterized by the irreversible formation of a three-dimensional dense molecular network by means of an exothermic reaction that promotes extensive cross-links⁽¹³⁸⁾, could induce variations from sample to sample. In particular, the large temperature rise produced during the curing stage might induce uneven thermal degradation⁽¹³⁹⁾. This degradation is a well-known phenomenon⁽¹³⁸⁾ naturally attributed to the low thermal conductivity of the material that induces significant temperature gradients in thick parts.

The present study was carried out on composites based on epoxy anhydride matrices reinforced by mineral particles. It appeared of interest to characterize the structural variations of the matrix originating from samples taken out from industrial pieces. These samples were obtained by pseudo-random withdrawal all over the piece. Despite considerable care in operation to ensure the reliability of the results, surprisingly broad distributions within measured thermal quantities (like T_g) were obtained, pointing out that the composites possess intrinsically inhomogeneous properties at a centimeter-scale. The literature on the relationship between process and thermal parameters of this type of composite is however not abundant⁽¹³⁸⁾. It was then of interest to understand why some zones appeared to achieve a higher degree of completion in the reticulation process than others. A representation of the thermal parameters as a function of the sample's distance from the injection point in the mold clearly revealed that the topological characteristics were the relevant parameter. The overall thermal parameters indeed appeared much less "noisy" when depicted versus the z-coordinate of the withdrawal position within the vertical mold. The new representation conducted to a phenomenological model of the thermal properties that fairly fits the whole set of measured data. Taking into account the topological position of the samples could thus, by interpolation, conduct to the values of the thermal quantities at any point of the global part with an excellent statistical confidence. More interestingly the phenomenological model proposed can, in return, serve as a tool for giving hints on the mechanisms occurring during the process of this type of complex composites. A difference in thermal history during at the very first stage of the process is believed to be the ground reason for the final scatter in experimental data. It is furthermore demonstrated that the post-curing stage decreases the width of the distribution but did not erase the topological effect.

5.2.1 Experimental

5.2.1.1 Materials and curing procedures

Several systems of particle-filled composites were studied differing by the chemical nature of the hardener, but with similar DiGlycidyl Ether of Bisphenol A (DGEBA) as prepolymer⁽¹⁴⁰⁾. Only the so-called C2 material will be presented in this section,

it was obtained with an anhydride hardener which, once reticulated, is of aliphatic type. The inorganic fillers (whose nature cannot be revealed) were dried by placing them into an oven at 60°C for 48 hours to reduce as much as possible the influence of water. The resin, the hardener and the filler were then mixed and stirred at 56°C and degassed under vacuum. The mixtures were then injected under pressure at the bottom of a vertical mold and underwent the cure process at 150°C for 15 minutes. The composites were then post-cured 8h at 140°C and 12 hours at 60°C to fulfill the reticulation process. The thermal analyses were carried out at several positions of the piece according to their topological situation as compared to the injection point. For each material, twelve zones were analyzed which actually solely differ by the injection time of the corresponding sample within the mold. The different sizes of the squares on Fig. 5.1 represent a result of a calculation with a CAD-software with the help of the exact shape of the piece (not shown). These twelve zones permit to explore every time domain associated to the process, Fig. 5.1.

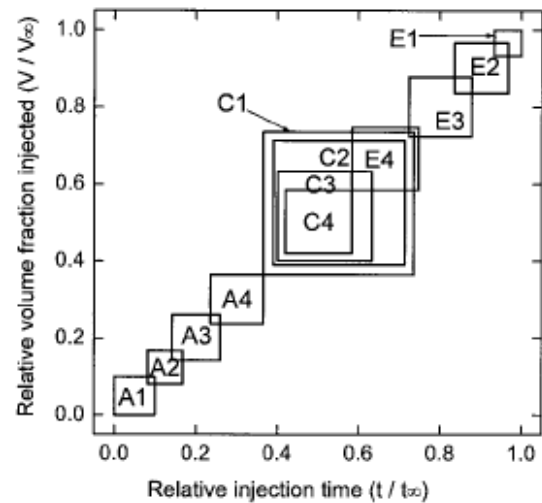


Figure 5.1 : Representation of the relative volume fraction as a function of the relative injection time (t_{rel}) for the 12 analyzed zones. from [Source:(140)]

For both systems the amount of filler was verified by TGA as a function of the above-defined zones⁽¹⁴⁰⁾. The volume fraction of filler was rather homogenous overall. A minor decantation process (less than 0.5 w%) could nevertheless be detected that induced a slightly larger amount of filler in the bottom part of

the pieces *i.e.* close to the injection point. Similar results were obtained using loss on ignition technique.

5.2.1.2 Differential Scanning Calorimetry analysis

Differential scanning calorimetry (DSC) analysis was carried out in a DSC 7 Perkin Elmer device. The calorimeter had previously been calibrated with the indium standard. The baseline was accepted when, after several iterations, the amplitude of the heat flow without samples and reference was below 0.5 mW in the considered range of temperature. The analysis was then carried out with samples containing 10 ± 1 mg of polymer. DSC thermograms were recorded under nitrogen atmosphere from 40°C to 170°C. Measurements of heat flow were conducted at a heating rate of $10^\circ\text{C}\cdot\text{min}^{-1}$. For each sample, two successive temperature ramps with a 5 minutes hold stage at 170°C between each ramp were carried out, in order to confer each sample with a similar thermal history. The data presented in the present section corresponds to rejuvenated samples¹ (second heating ramp) to prevent aging effects.

5.2.1.3 Definition of the extracted parameters

T_g is usually defined three different ways⁽¹⁴¹⁾, Fig. 5.2. In the present manuscript a fourth definition was chosen which corresponds to the actual onset of the glass transition. It was accordingly defined as the temperature at which the DSC thermogram splits from the base line. T_g endset was similarly defined as the temperature at which the thermogram returned to the thermodynamic equilibrium state. These definitions were chosen because they brought robust parameters with evident physical meanings. To further improve the stability and reproducibility of the parameters, a numerical method was developed based on the calculation of the first derivative of the thermograms. Overall three independent parameters were eventually extracted from each thermogram that clearly characterized the structural state of the polymer within the composite:

¹The samples were tested shortly after being processed anyway.

- T_g : Actual beginning of molecular mobility induced by the glass transition (temperature corresponding to the “takeoff” from the base line²).
- ΔT_g : Width of the glass transition (= T_g endset - T_g).
- ΔC_p : Difference in heat capacity between rubbery and glassy states.

An example of such a determination is proposed in Fig. 5.2-b, corresponding to the raw data of a C2 composite.

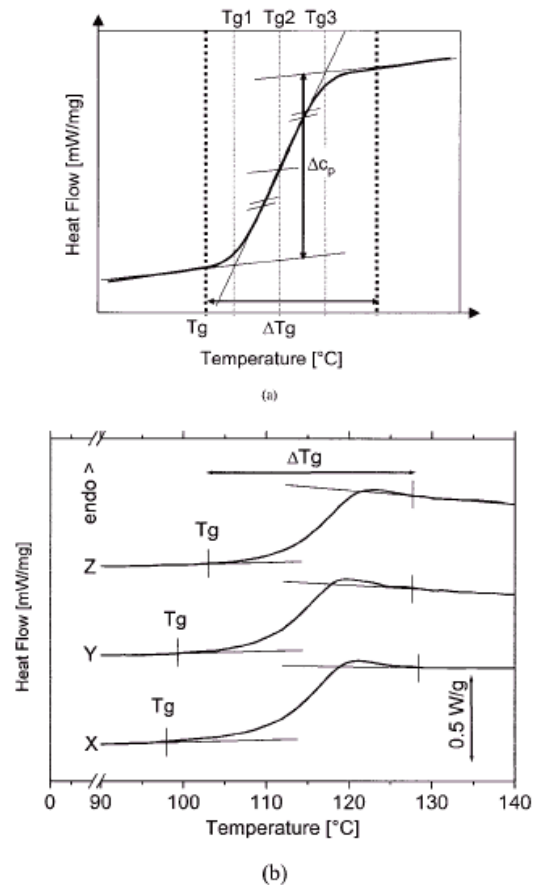


Figure 5.2 : Definition of the three independent parameters extracted from the thermograms: T_g , ΔT_g , and ΔC_p . from [Source:(140)]

For stoichiometric blend, low T_g generally result from an incomplete reaction, it thus seemed pertinent to utilize a fourth dependant parameter, with a clear physical meaning: the extent of cure, α . The DiBenedetto equation, as modified by Pascault and

²Note that this definition is also different from the regular definition of T_g onset

Williams⁽¹⁴²⁾ is a well-accepted equation to interrelate T_g and α . It takes the form:

$$\frac{T_g - T_{g0}}{T_{g\infty} - T_{g0}} = \frac{\lambda\alpha}{1 - [1 - \lambda]\alpha} \quad (5.1)$$

- T_{g0} represents the glass transition temperature of the initial un-reacted mixture.
- $T_{g\infty}$ is the maximal glass transition temperature reached with an isothermal curing.
- λ is an adjustable parameter between 0 and 1, which represents the ratio of segmental mobility for crosslinked and uncrosslinked polymer.

Montserrat^(143;144;145;146) determined the different parameters ($T_{g\infty} = 109^\circ\text{C}$, $T_{g0} = -23.2^\circ\text{C}$, $\lambda = 0.69$) for a system chemically similar to *C2*. Though these parameters were determined experimentally on the neat resin, it seemed reasonable to assume that they are not much altered by the presence of the filler (C_p is indeed not involved in the formula). A fit of the $T_{g\infty}$ parameter was nevertheless necessary to adapt the numerical values to the different definition of T_g . The extend of cure (α) utilized in the present manuscript was hence determined through Eq. 5.1 using $T_{g\infty} = 104^\circ\text{C}$; $T_{g0} = -23.2^\circ\text{C}$; $\lambda = 0.69$.

5.2.2 Results and discussion

Although the random sample withdrawal method has shortcomings it is commonly and successfully used for characterization of the properties of massive composite parts, it was therefore the starting point of the present study. The three independent parameters were first analyzed for all materials using a pseudo-random sample withdrawal method, meaning without taking into account the samples positions in the mold. Fig. 5.2.b depicts, as an example, three raw thermograms for *C2*, showing the magnitude of the measured differences in T_g values.

5.2.2.1 Dispersion of the thermal parameters

The histograms of T_g , ΔT_g and ΔC_p populations can not be fitted to Gaussian curves, because sampling was not totally random, each zone of each material being represented, Fig. 5.3.

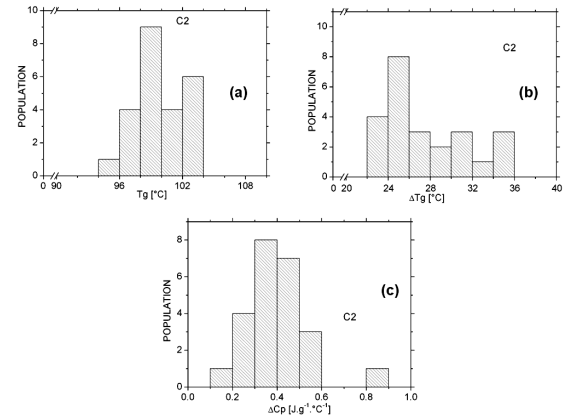


Figure 5.3 : Histograms of populations of the three independent parameters: (a) T_g , (b) ΔT_g , and (c) ΔC_p (the experimental data are represented without accounting for the withdrawal position). from [Source: (140)]

5.2.2.2 Transition width

ΔT_g and ΔC_p Fig. 5.3.b and 5.3.c. displays respectively the ΔT_g and ΔC_p dispersion for all the studied composites. The T_g , ΔC_p presented a rather dispersed behavior suggesting that the random sample withdrawal used to determine thermal parameters failed to give a reasonable characterization of the measured properties. In fact the dispersion in measured data was so broad that the uncertainty on thermal parameters could not faithfully express the materials properties. It was then assumed that this dispersion in measured data was due to “bad data points” that should be removed by a statistical analysis. This approach was done by removing points too far away from the mean value (using the “jackknife” technique⁽¹⁴⁷⁾), but it appeared that most of the physical information was lost. In particular, the very good correlation between T_g and ΔT_g seemed to reveal that the entire set of data had to be considered, and that the apparent “noise” within the experimental points was actually related to the fact that an important parameter was missing in the representation.

5.2.2.3 Thermal parameters represented as a function of the samples’ positions.

An exploratory analysis was realized in order to decrease the apparent noise in these broad distributions. Regarding the rather straightforward processing conditions, the sole issue that differentiates between the samples appeared to be their position in the mold. It

was first assumed that the thermal quantities should, to some extent, follow a regular variation within the global piece. To better reveal this continuity T_g , ΔT_g and ΔC_p were thus labeled as a function of the topological location of the corresponding samples in the mold. More precisely the twelve zones were differentiated by the relative time of injection of the resin during the injection process $t_{rel} = t/t_\infty$. Assuming that gravity was the leading parameter, the zones close to the injection point received fresh resin until the end of the injection process and thus came up with the shortest curing times (zone X, Fig. 5.1). On the contrary the top of the mold is eventually filled with the material that first came into the mold and thus obtained the longest curing time. Fig. 5.4 depict the same experimental T_g values as Fig. 5.3, but as a function of t_{rel} .

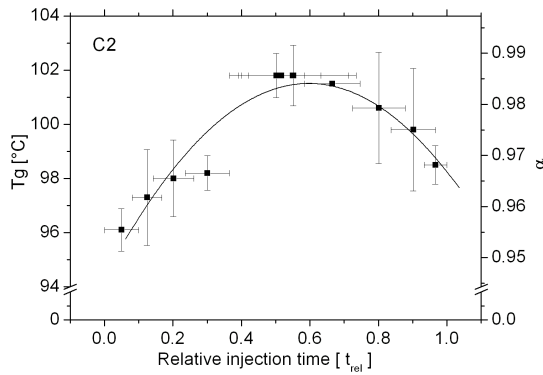


Figure 5.4 : T_g as a function of the relative injection time t_{rel} from [Source: (140)]

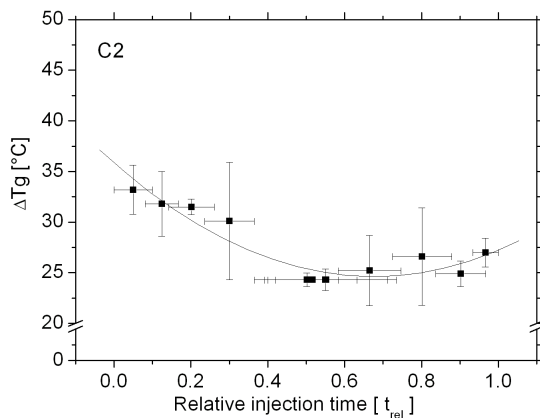


Figure 5.5 : ΔT_g as a function of the relative injection time t_{rel} from [Source: (140)]

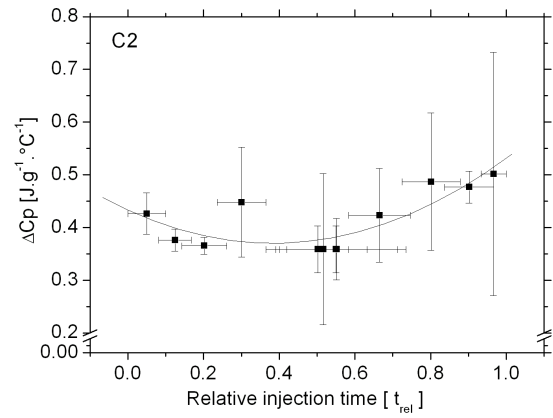


Figure 5.6 : ΔC_p as a function of the relative injection time t_{rel} . [Source: (140)]

	Coeff. determination	p-value
T_g/T_{rel}	0.8198	9.51×10^{-7}
$\Delta T_g/t_{rel}$	0.8036	2.26×10^{-6}
$\Delta C_p/t_{rel}$	0.5160	9.84×10^{-3}

Table 5.1 : Coefficients of Determination and p – values Between T_g , ΔT_g , ΔC_p , and t_{rel} [Source: (140)]

The parabolic behavior that this new representation brought out emerged with much less apparent noise on the experimental data. A statistical analysis with the entire set of data confirmed the dependence with an excellent correlation between these two variables (T_g and t_{rel}). Other similar materials also follows a similar tendency which comforted the analysis (140). The representation of T_g as a function of the relative injection time hence appeared to be fruitful. The same method was thus applied to ΔT_g and ΔC_p . The ΔT_g , when represented against t_{rel} , also fairly follows a parabolic law, as shown in Fig. 5.4. For the two materials for which this parameter could be determined, ΔT_g and t_{rel} were significantly correlated with a confidence interval of 97% (Table 5.1). The last determined parameter ΔC_p again tends to follow a parabolic behavior in the new representation (Fig. 5.6).

	Coeff. determination	p-value
T_g/T_{rel}	0.8198	9.51×10^{-7}
$\Delta T_g/t_{rel}$	0.7573	1.80×10^{-5}
$\Delta C_p/t_{rel}$	0.1045	6.27×10^{-1}

Table 5.2 : Coefficients of Determination and p – values Between T_g , ΔT_g , ΔC_p , and α [Source: (140)]

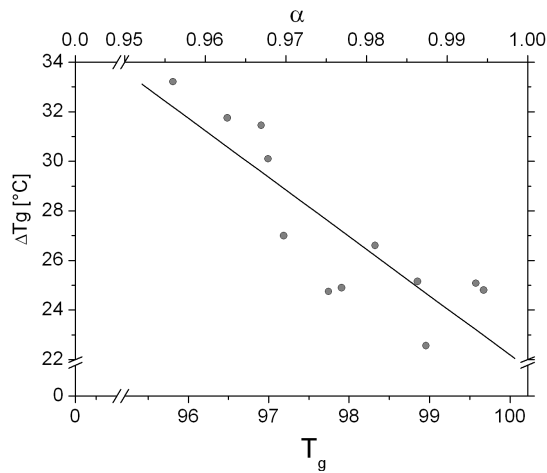


Figure 5.7 : ΔT_g versus α for the C2 composites. [Source: (140)]

From the above described results it is worth noticing that although they both follow a parabolic tendency, T_g (or α) and ΔT_g exhibit inversed behaviors. In other words, the coefficients corresponding to t_{rel}^2 had opposite signs. A statistical analysis confirmed that ΔT_g was significantly correlated to the extent of cure as shown in Table 5.2 and Fig. 5.7. In addition, ΔT_g can be considered as a pertinent parameter to estimate the homogeneity of a cured epoxy system. The relationship between ΔT_g and T_g indeed takes the linear form:

$$\Delta T_g = a - b.T_g \quad (5.2)$$

where $a = 258^\circ\text{C}$ and $b = 2.36$ represent experimentally estimated constants. Eq. 5.2 actually provides a rationalization to the fact that with the studied polymer (a thermosetting matrix in a composite with an incomplete reticulation) contains heterogeneities that increase the width of the glass transition temperature, besides reducing its absolute value.

5.2.3 Results overview

In summary, the thermal parameters of the composites appeared, at a first glance, to present a stochastic distribution. By using a new representation of the experimental data versus the relative time of injection, the entire set of data could, actually, be defined with a much better resolution. A parabolic behavior was systematically obtained for the three independent parameters T_g , ΔT_g and ΔC_p without eliminating

any data even if statistically considered as “not significant”.

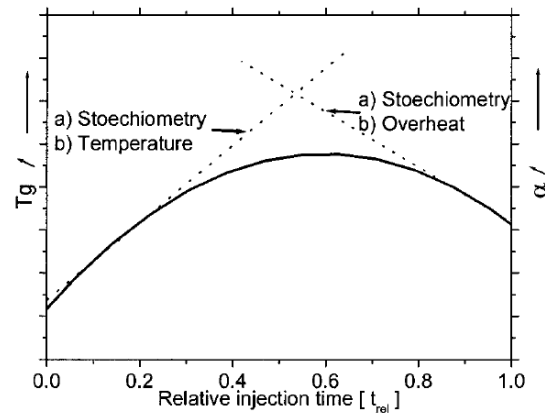


Figure 5.8 : Schematic representation of T_g as a function of t_{rel} . from [Source: (140)]

An explanation of the bell-shape of the curves of T_g as a function of t_{rel} can be proposed, Fig. 5.8. For the zones far away from the injection point (bottom of the mold), relatively lower T_g can be interpreted through:

a) A stoichiometric defect which could result from the slight decantation of the filler during the process, as observed by TGA,⁽¹⁴⁰⁾. The decantation process could indeed induce a decantation of the pre-polymer which has a better affinity with the mineral filler, and thereby modify the stoichiometry and decrease T_g ⁽¹⁴⁸⁾.

b) An overheat of the composite that caused a chemical degradation of the polymer⁽¹⁴⁹⁾. The overheat could obviously be the direct consequence of the longer curing time. This hypothesis is also supported by the fact that the top zones are eventually filled with the materials that went through the hot mold all the way (corresponding to the hot front). In addition, overheat could be magnified by the lower amount of fillers measured on the top zones of the mold. The fillers are indeed acting as heat dissipaters due to their high heat conductivity and specific heat as compared to the polymer. The later interpretation is however not likely because of the very low amplitude of the decantation observed⁽¹⁴⁰⁾.

For the zones close to the injection point a symmetric thought process can be applied to describe the relatively lower T_g :

a) The stoichiometric effect⁽¹⁴⁸⁾ similar to the one described above and induced by the filler decantation during the process.

b) A thermal effect⁽¹⁵⁰⁾ induced by the shorter curing time⁽¹⁵¹⁾, lower temperature (as compared to the top zone) and slightly lower amount of reinforcing particles.

The first explanation, which would require at least a partial phase separation and diffusion between the very compatible two components of the polymer, does not seem to be likely. The second possibility could, on the contrary, arise from realistic events and seemed accordingly reasonable for these composites.

5.2.4 Conclusion

The processing of epoxy based composites induced a broad dispersion in DSC measured of independent thermal parameters Tg, ΔTg , ΔCp at the molded piece scale. These distributions, that first appeared to be stochastic, could actually be directly related to the withdrawal zone of the analyzed sample. A new parameter was defined, the relative time of injection in the mold, (t_{rel}) that enables to describe the entire set of data by parabolic curves. These parabolic behaviors revealed that Tg (or α) as linked by the DiBenedetto equation) possessed lower values in the vicinity of the injection point and at the top of the vertical mold. ΔTg and ΔCp also exhibit a parabolic behavior when displayed against t_{rel} , but the extreme zones (close and far from the injection point) lead to the highest values. This inversed behavior was confirmed by the statistical study.

Because ΔTg was defined as the temperature difference between the very beginning of the molecular mobility associated with Tg and the temperature at which the system goes back to the thermodynamic equilibrium, it seemed to be the pertinent parameter to assess the network heterogeneity. This work thus indicates that epoxies anhydride in under-reticulation state posses a rather heterogeneous network. In particular the post-curing step not only contributes to higher the absolute values of Tg, but also favors the network homogenization.

Even with a very well controlled process some variability remains. With the condition of taking precautions and with a large set of data, it was possible to extract physico-chemical information thanks to this variability, without any intervention on the process itself.

Although no definitive interpretation can be given for this topological dependence of the thermal parameters, a difference in thermal history during the very first step of the process is believed to be the ground reason for the final scatter in experimental data. It was additionally observed that even a post-curing stage performed much above the glass transition temperature could not erase this topological effect. It could now be of interest to confirm the correlation with samples presenting a wider range of reticulation states in order to obtain even more sensitive data. The linear relationship in the studied domain between α and Tg limited the study of the new relationship that links up Tg (or α) to ΔTg . It would consequently be of particular interest to reveal which of the α or Tg parameter would be related to the ΔTg over a broader range of variation.

5.3 Influence of the micro and meso scales on high voltage properties

This section relates both an experimental study and a numerical investigation of the breakdown field in particle reinforced thermo-sets. The experimental study revealed that the increase of the conversion degree (α) of the epoxy matrix improved the field to breakdown both in divergent and quasi-homogeneous fields. It was also observed that the presence of the second phase (mineral filler) dispersed within the polymeric host led to apparently contradictory results depending on the nature of the electric field. The neat matrix indeed exhibited a higher field to breakdown than that of the composite in a quasi homogeneous field configuration whereas the opposite behavior was evidenced in a point-plane configuration. It thus appeared that the filler can either prevent or ease the breakdown phenomena, depending on the nature of the electrodes configuration.

In order to further understand this statement, a numerical simulation of the dielectric breakdown was proposed. A deterministic model that accounts for the organization within real composites was developed. This numerical method, based on the resistor-short breakdown model was improved to directly account for the real phase arrangement within the samples through SEM pictures. The simulation furnished the

explanation for the apparent disagreement, evidencing that the inorganic particles protect the composite in divergent fields through a mechanism close to the so-called barrier effect, whereas the same fillers were responsible for a local intensification of the electric field and thereby a reduction of the dielectric strength in a quasi homogeneous field.

In this section the breakdown phenomena are first studied from the local point of view through SEM characterizations of the damaged trees and with the above described meso-macro finite element simulation. This approach revealed that apparent contradictions within a series of macroscopic measurements presented actually a rather straightforward explanation when regarded in terms of mechanisms at a microscopic scale.

5.3.1 Experimental

5.3.1.1 Materials and specimen preparation

The composite under investigation is basically the same as the one described in the previous section. In order to also investigate the effect of the filler on the electric properties, a pure unfilled epoxy was also prepared and denominated "M2". For the M2 material the curing temperature was reduced to 100°C to prevent degradation due to the exothermic reticulation reaction. All the samples were eventually post-cured 8h at 140°C and 12h at 60°C in order to supplement the reticulation process.

For *C2* composite, a sampling of materials was carried out with various conversion degrees close to the optimal reticulation state^(140;152). The resulting set of samples however presented slightly different curing times and temperatures, which led, with the help of the Di Benedetto equation⁽¹⁴²⁾ to six conversion degrees ranging from 0.95 to 0.995, Fig. 5.9.

All samples were then cut by an accurate cut-off wheel to obtain a constant width in close to 0.5 ± 0.1 mm, they were grinded and polished a specific way⁽¹⁵²⁾ to obtain a mirror polished surface.

5.3.1.2 Breakdown voltage measurements

The voltage transformer for dielectric breakdown measurements provided an AC voltage at industrial frequencies (50Hz). The specimens were immersed in silicon oil to prevent the surface discharge (flashover). An AC voltage ramp was applied to the specimen in

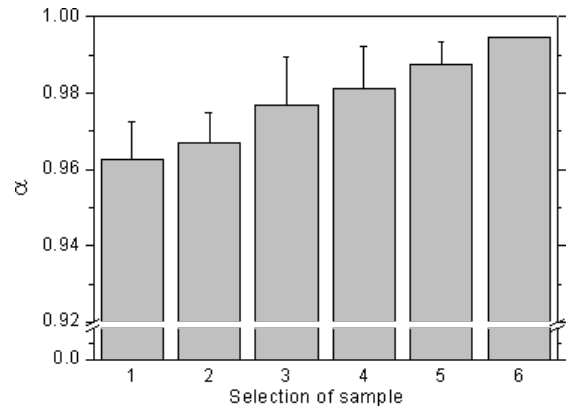


Figure 5.9 : Sampling of *C2*-composite with various conversion degrees (α) [Source: (109)] .

contact mode until dielectric breakdown, after which the experiment was rapidly stopped. Breakdown occurred between 10 and 20 seconds with a ramp rate of about $1 \text{ kV}\cdot\text{s}^{-1}$. The field to breakdown was measured at 20°C as the result of the average of 4 samples measurements. Breakdown measurements were performed both under divergent and quasi homogeneous field, using respectively point-plane (Fig. 5.10-a.) and sphere-sphere (Fig. 5.10-b.) electrode configurations. The point electrodes were made of tungsten with a tip head radius of curvature close to $30 \mu\text{m}$, whereas the copper plane electrode was a flat disk with 77.5 mm in radius. The sphere electrodes were made of stainless steel with a diameter of 15 mm.

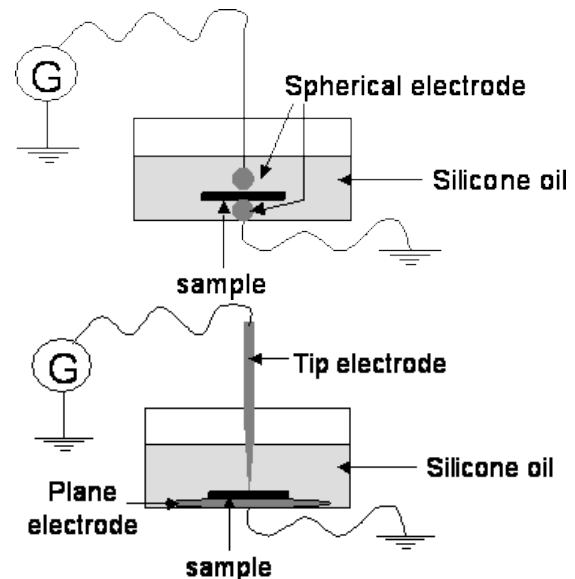


Figure 5.10 : Test specimens used to measure dielectric breakdown (a) point-plane electrodes and (b) spherical electrodes [Source: (109)] .

The breakdown field in quasi-homogeneous configuration mainly depends on the maximum voltage and the electrodes gap, *i.e.* the sample width in contact mode.

$$E = \beta \times E_m \quad (5.3)$$

where $E_m = V/d$ and β the non-uniformity coefficient of the electric field; it depends on the geometry of the electrodes and the thickness of the sample, and it is very close to 1 (about 1.02) in the present case. The dielectric breakdown strength (kV/mm) was in consequence measured in sphere-sphere configuration simply by dividing the voltage to breakdown by the samples' thicknesses.

Under divergent field, the electrical field to breakdown was quantified at the tip of the sharp electrode according to the following relationship⁽¹⁵³⁾.

$$E = \frac{2V}{r \ln(1 + 4d/r)}$$

where V is the maximum applied electrical voltage, d is the electrode gap (*i.e.*, the sample width), and r is the tip radius of the point electrode.

5.3.1.3 SEM characterization

Observations of the breakdown tree paths and composite morphology were performed by means of a scanning electron microscope Stereoscan 440 LEICA. In order to obtain a good observation of the treeing, a technique similar to that generally used to cut the glass was performed. A straight line was first scored in one time on either sides of the perforation hole, purposely avoiding the vicinity of the hole, Fig. 5.11. The sample was then broken at room temperature using breaking pliers. The surface of the samples were finally metallized by cathode vaporization treatment, which covered the surface by a thin gold layer (≈ 50 nm).

A topologic analysis using the secondary electrons diffusion showed up being well-suited to reveal the breakdown trees. In the point-plane configuration, many trials were necessary to obtain a sample that mechanically broke following a surface that included dielectric breakdown trees. Cold breakage in liquid nitrogen did not seem to increase the odds of this *rare* event.

In addition to this procedure photomicrographs of mirror polished surfaces with retro-diffused electrons

(sensitive to chemical nature) produced good pictures with a high contrast between the filler and the matrix and were subsequently employed as an input of the numerical simulation (see §4.4 for details).

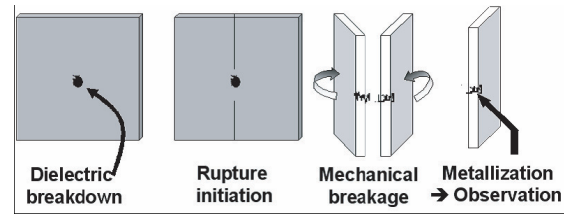


Figure 5.11 : Sample preparation for SEM treeing characterization [Source: (109)] .

In order to restrain possible moisture differences, all the studied samples were first conditioned under vacuum at 60°C for a week prior to testing.

5.3.1.4 Simulation of the dielectric breakdown

Several methods can be found in the literature to describe the electrical properties of heterogeneous systems⁽¹⁵⁴⁾. This problem can be regarded an analytic way or a numerical way. Analytical models were rejected from the present study, because they generally poorly account for the composite morphologies. The chosen model was therefore based on the equivalent-circuits model or, in other words, FEA calculations. The successive steps required for the simulation will be described below. The model is an in-house iterative resistor-short breakdown simulation, developed by Flandin *et al.*^(114;155). This code was developed with a help of three freeware available on the internet (i) ImageJ⁽¹¹⁶⁾ for image analysis, (ii) Triangle⁽⁴¹⁾ a fast and robust mesh generator generously shared by Dr. Shewchuk of the University of California at Berkeley and (iii) spice 3f5 a general-purpose circuit simulation program, initially developed at the University of California, Berkeley. A version called Spice+ was utilized⁽⁴³⁾ in this study.

5.3.2 Results and discussion

The breakdown trees are first regarded from the local point of view through SEM characterizations in order to get an appreciation of their behaviors at a microscopic scale. The breakdown fields will be also analyzed afterwards based on the previous analysis.

5.3.2.1 Morphological analysis of the damaged area

Point–plane configuration To obtain a reliable representation of the dielectric breakdown process in the composite; SEM pictures were taken on samples after dielectric breakdown occurred. With the point–plane electrodes configuration an almost one–dimensional, filamentary–like structure was observed with about $1\mu\text{m}$ in diameter. This tree was similar in nature to that generally observed in a point–plane configuration^(88;120) with unfilled epoxy. Because this channel went all the way from one electrode to the other (Fig. 5.12-a.), it was assumed to represent at least one of the conducting paths responsible for the final breakdown of the whole composite. Due to the large field enhancement around the point electrode^(88;101), it seemed reasonable that the tree started on it and grew in direction of the plane electrode (see arrow on the picture). Looking closely to the damaged structure, it is striking to observe that the conducting tree bypassed around inorganic fillers (Fig. 5.12–b) evidencing that the treeing took preferably place within the polymeric host. This result, forecasted by CHO *et al.*⁽¹²⁶⁾ is, to the authors’ knowledge, first time evidenced in the present work. A direct consequence of the mandatory bypass of the fillers is also visible on the Fig. 5.12. DIS-SADO *et al.*^(107;112) indeed noticed that the tree increments were at least $5\mu\text{m}$ in length within a neat epoxy. In the present case, the tree increments could be much shorter, when stopped by minerals particles. This later observation is nothing but a reformulation of the so–called “barrier effect” that can be played by the mineral fillers.

Sphere–sphere configuration For comparison the same SEM analysis was performed in the sphere–sphere configuration (quasi–homogeneous field). It was however not possible in this case to obtain similar pictures. Instead of getting channel with $1\mu\text{m}$ in diameter from one electrode to the other, a much larger degradation took place leading to a “damaged crater” with few hundreds microns width and even larger extremities, Fig. 5.13. It was in consequence not possible, in this symmetric electrode configuration, to describe a starting point and an end to the damage propagation. It was then concluded that the much lower field localization in this case was responsible for a more global breakdown of the structure.

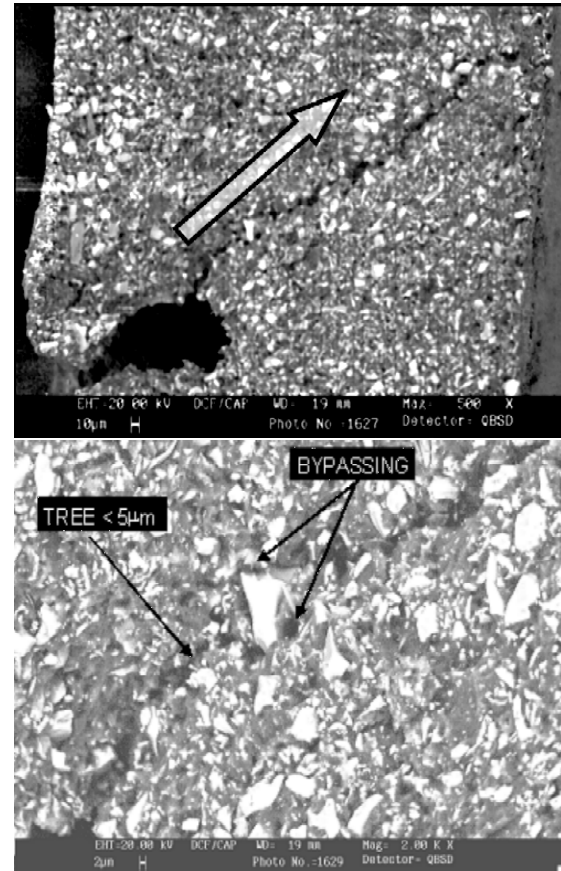


Figure 5.12 : SEM picture of electrical tree in the composite under divergent field [Source:(109)] .

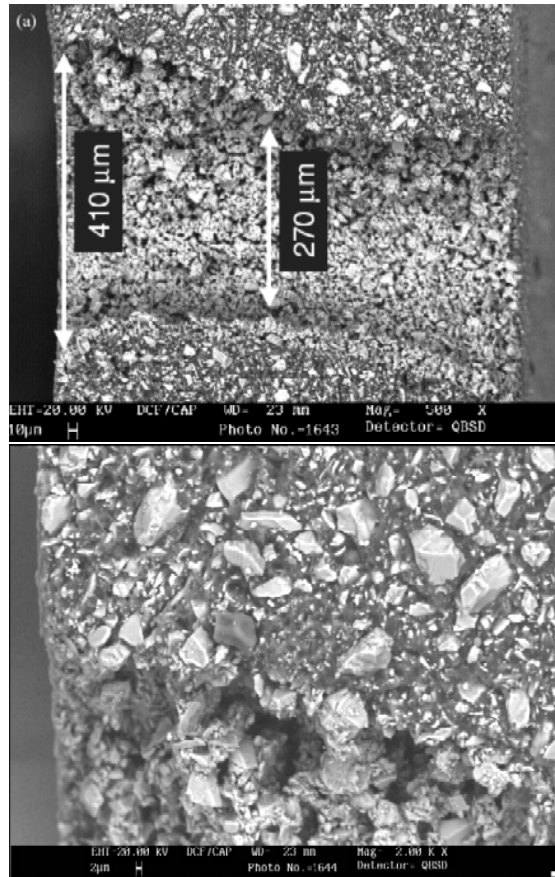


Figure 5.13 : SEM picture of electrical tree in the composite under quasi-homogenous field [Source:(109)] .

Conclusions for SEM observations A schematic drawing of the above analysis both in quasi-homogeneous and divergent fields is proposed in Fig. 5.14. The main difference between these two configurations can be summarized by the scale at which the damage might be initialized.

1. In sphere-sphere configuration, a quasi-homogeneous field is perceived all over the piece. The damage could thus equally initiate anywhere within the structure, and should hence first take place in the vicinity of the major flaws. The quasi-homogeneous configuration should as a consequence correspond to a “Global Weakest Link” (*GWL*) at the whole sample scale.
2. On the contrary, in the point-plane configuration, the divergent field is largely enhanced around the tip of the point electrode. The damage tree should thus start in the vicinity of this electrode, almost independently from the flaws too far away from it. The divergent configuration should thus correspond to a “Local Weakest Link” (*LWL*) accompanied by a major cumulative process.

This difference between these two types of solicitations can thus, at this point, be summarized by the initiation process. The “nucleation” is believed to be spatially restricted to the point electrode in one case and possible anywhere in the other case. This difference originates from the geometry of the electrodes and led on the one hand in a filamentary-like structure of the tree (divergent field) and on the other hand in a global fall down (quasi-homogeneous field). This schematic approach is corroborated by the relative values of the breakdown voltage and electric field in both configurations. The breakdown voltage of samples with similar thicknesses was indeed much lower in the case of the point-plane configuration as compared to the sphere-sphere one. This is generally explained by the field enhancement surrounding the tip of the point electrode. When corrected by Masson equation⁽¹⁵³⁾ the actual field at the tip is however much higher in the point-plane configuration than in the sphere-sphere one. The difference (almost an order of magnitude, see experimental results), might be related to the complexity in calculating the actual field, experimental uncertainties, etc. It is also believed that the higher field to breakdown measured in

the divergent field results from the search in the vicinity of the point electrode for the *LWL* that might be much stronger to overcome than the *GWL* to achieve in a quasi-homogeneous field.

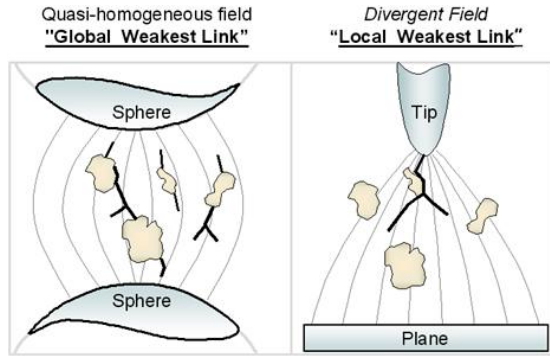


Figure 5.14 : Schematic representation of the proposed tree propagation in sphere-sphere (Global Weakest Link, left) and point-plane (Local Weakest Link, right) configurations [Source: (109)] .

5.3.2.2 Influence of conversion degree on the dielectric breakdown

The influence of the degree of curing on dielectric breakdown was evaluated by measuring the field to breakdown on the sampling of *C2* composite.

Fig. 5.15-a shows the variations of the field to breakdown in a divergent configuration, as a function of the conversion degree (α ranging from 0.96 to 0.995). Within this range of α -values, the field to breakdown obeys an almost linear increase of about 30% with α . A statistical study even revealed that α and the field to breakdown were significantly correlated, 5.3.2.2.

In quasi-homogeneous field (Fig. 5.15-b) configuration the dielectric strength similarly increased linearly with α . A statistical study showed nevertheless that dielectric breakdown was not, in this case, significantly correlated to the conversion degree (P value $> 5 \times 10^{-1}$, see 5.3.2.2). The relative variation in dielectric strength was, in addition, much lower with only 3% increase in the same conditions.

For a given filler state (amount, chemistry, dispersion, but also size and shape), the enhancement of the completion of curing of the thermo-set matrix largely improved the field to breakdown of the composite: 5% increase in the degree of curing induced a 28% increase in the breakdown field. The macroscopic field to breakdown thus turned up to be quite sensitive to the local structure of the polymeric host.

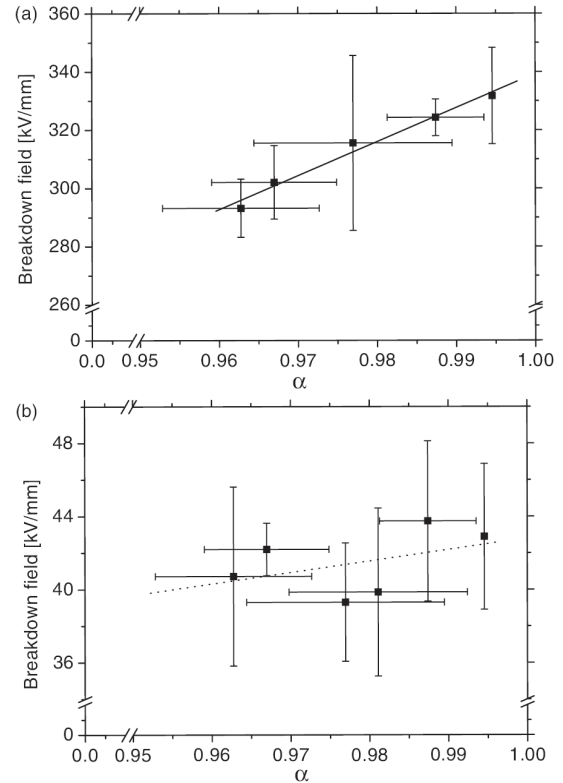


Figure 5.15 : Dielectric Breakdown as a function of conversion degree under divergent (a) and quasi-uniform (b) fields [Source: (109)] .

	R2	P-value	Changes
QHF	0.9896	1.3×10^{-3}	28 %
DF	0.6688	8.5×10^{-1}	3 %

Table 5.3 : Coefficient of determination and P value between field to breakdown and α . QHF and DF stand for Quasi Homogeneous Field and Divergent Field, respectively [Source: (109)] .

Increasing the α value directly decreases the amount of dead ends within the structure that might present a polar nature⁽⁸⁸⁾ and favor the initiation/propagation of the dielectric tree. This reduction of flaws in polymer network thus improved the field to breakdown. It also came out, however, that the divergent field experiments presented a much higher sensitivity to structural variations than the quasi-homogeneous counterparts. This later result seemed to directly arise from the initiation of the damage process schematically described in Fig. 5.15 and summarized by the above described *GWL* versus *LWL* concept. In a quasi-homogeneous field configuration, the breakdown is controlled by the presence of major flaws found anywhere within the structure, as described in the *GWL*. The filler with about $6\mu\text{m}$ in diameter obviously materialize this major heterogeneity in a composite. As a result, an improvement of the intrinsic properties of the polymeric host only slightly influences the macroscopic behavior that remains controlled by the presence of the fillers. On the contrary, in a divergent field configuration, the damage first occurs at the surface of the needle tip and should directly overcome the improvement of the polymer without being strongly helped by the fillers. The search for only the *LWL* induces a stronger increase in the field to breakdown.

From the above description, it seemed that the fillers should play a major role on dielectric breakdown of these composites in a quasi-homogeneous field. The same fillers appear, on the contrary, to much less alter the macroscopic behavior in a point-plane configuration. It was thus of interest to compare the breakdown voltage of these composites to that of the neat matrix in both configurations. The results will be described in the next section.

5.3.2.3 Influence of inorganic fillers on the dielectric breakdown

In the particular case of a composite, the difference in electric properties between the two phases induces a large field enhancement^(88;131) around the fillers that can be viewed as the largest flaws within the structure. The purpose of this section is to estimate the quantitative influence of this heterogeneity on the macroscopic behavior of the material.

Divergent field Fig. 5.16-a shows the average-field to breakdown for both the neat epoxy matrix and the *C2* corresponding composite with similar degrees of curing. The field to breakdown was significantly increased by the presence of the fillers. According to the literature, this result could be explained two ways:

1. Either the barrier effect due to the fillers: the trees within the insulator have to bypass the mineral particles, as schematically depicted Fig. 5.16-b.
2. Or the thermal effect: under the direct influence of the electric field, insulators experience overheating by Joule effect as a result of the high electrical conductivity of the damaged tree. This very local overheats naturally lead to temperature gradients that might favor the propagation of the conductive paths⁽¹⁵⁶⁾. The inorganic-fillers, with their much higher heat capacity and conductivity might reduce overheat and thus disfavor the thermal breakdown.

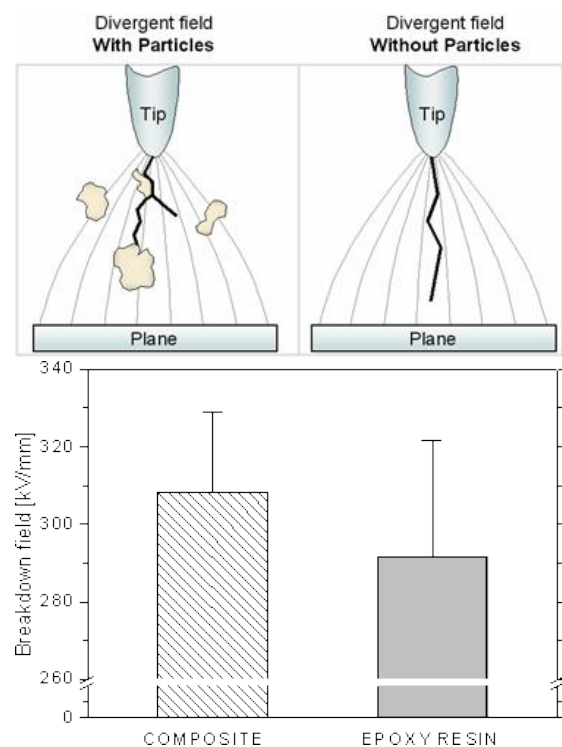


Figure 5.16 : Dielectric Breakdown, measured in a point/plane configuration for both systems M2 and *C2* (a) and schematic interpretation of the reinforcing influence (b) [Source: (109)] .

Quasi-homogeneous field Fig. 5.17-a shows the average-dielectric strength for both the neat epoxy matrix and the C2 corresponding composite with similar degrees of curing. In contrast to the results obtained in a divergent field, the dielectric strength was, in the quasi-homogeneous configuration, significantly reduced by the presence of the fillers. This result can qualitatively be associated with the field gradients induced by the mineral particles which possess a higher electrical conductivity and permittivity. Moreover, these intensifications of the electrical field could be aggravated by the presence of asperities on the fillers. For the neat matrix, in contrast, the electrical field should be homogeneous and the dielectric strength possessed hence a higher value.

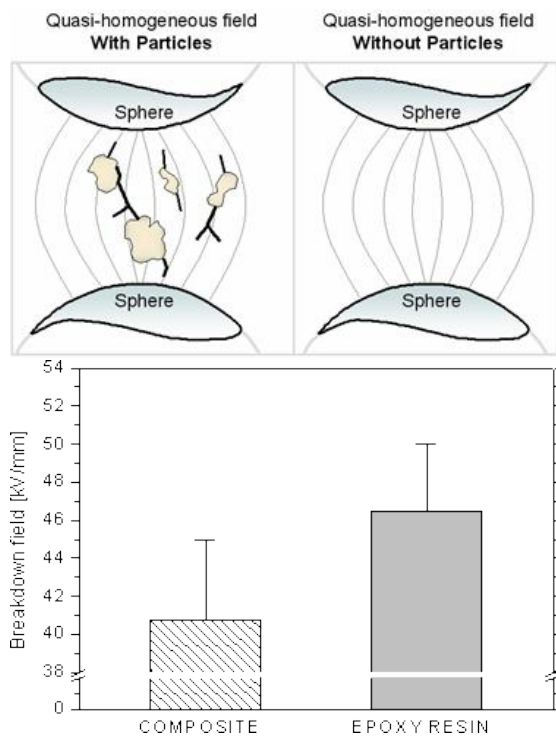


Figure 5.17 : Measured dielectric breakdown in sphere-sphere configuration for both systems M2 and C2 (a) and schematic interpretation of the influence of the filler (b) [Source: (109)] .

An interesting ‘composite effect’ has been evidence which depends on the nature of the electric field: in a quasi-homogeneous field the reinforcing particles behave as flaws and decrease the dielectric strength of the considered epoxy whereas the same particles seem to prevent the degradation of the polymer network when placed in a divergent field. It is thus of particular interest to model the dielectric breakdown of the neat matrix and of the composite both in divergent

and quasi-homogeneous fields to estimate the relative influence of the electric and thermal effects.

5.3.2.4 Simulation of the dielectric breakdown

The simulation simulation is the same as the one presented in chapter 4, page 47. The goal is to use it to determine if a purely electric effect might explain the complex ‘composite effect’ described above.

In the case of homogeneous solids, several statistical models have been developed to describe the breakdown patterns⁽¹⁰⁷⁾. The case of heterogeneous systems is, however, more complicated^(128;157) because of the field enhancement which develops between phases with contrasted physical properties⁽¹⁵⁴⁾. In addition the field distribution is dynamically modified by the growth of a low resistive tree. As a result the propagation is an intrinsically cumulative process which should be modeled a dynamic way. This particularity makes beneficial the use of a voltage controlled resistor-short breakdown model. Martin *et al.*^(108;158;159) proposed to view the composite as a resistor network where the center of mass of each particle was a node connected to its closest neighbors by a resistor. These resistors were supposed to irreversibly short to ‘perfect conductors’ when the current reached a threshold value. The strong positive feedback of this model gave roughly one-dimensional breakdown trees. The only drawback of this attractive methodology is to represent each particle by only one node, hence assuming they are isopotential⁽¹¹⁴⁾.

A more realistic simulation, based on the resistors network approach, was then developed with the help of SEM pictures. The image (Fig. 5.18-a) was first binarised (Fig. 5.18-b) and the coordinates of the contours were then saved for each particle. The next step, an unstructured mesh was created that contained the contours points (Fig. 5.18-c). The mesh was performed with angles greater than 30° to prevent biased results during the electrical calculation. Within this mesh it seemed reasonable to set two kinds of nodes representing either the matrix or the filler, depending on their geometrical positions. The electrical properties were then assigned to each phase using rigorous finite element discretization methods⁽¹¹⁷⁾.

The simulation was run using a sequence of calculations performed with the spice 3f5 software and in-house codes. A unit voltage is applied to the network

and Kirshoff's laws (or equivalently the Laplace equations) are solved to find each node's potential. The current flowing in every link is then determined and the most stressed link is registered and considered as definitively shorted. This maximum current is then divided by the short current and the applied voltage is multiplied by this factor to determine the applied voltage V_s at which the resistor will short. This hypothesis obviously corresponds to the particular case of linear (ohmic) resistors. Once the most stressed resistor has been shorted, the new equilibrium potential is computed, the "hottest" node⁽¹⁰⁸⁾ found, shorted, etc. (Fig. 5.18-d) until a conducting path had gone through the entire simulated composite (Fig. 5.18-e).

The dielectric breakdown simulations presented are entirely deterministic in nature; no random number generator was employed for the breakdown calculations. The resulting breakdown voltage was obtained for each set of nodes with the method developed by Martin *et al.*⁽¹⁰⁸⁾. Because the damaged tree mandatory followed the defined mesh, various meshes were calculated from the same initial image and a Weibull (Fig. 5.18-f) analysis was performed on the resulting fields to breakdown.

5.3.2.5 Evidence for GWL concept

An example of a breakdown tree is described in Fig. 5.20 for a plane-plane electrodes arrangement. In this macroscopically homogeneous field configuration, field gradients solely result from the presence of the particles. As a result, a strong correlation emerged between the presence of the fillers and the nucleation of damaged trees. The shorts indeed mainly took place close to the particles-matrix interfaces. The asperities on particles, even away from the main breakdown trees also showed a tendency to develop shorts that remained localized in this simulation, which was stopped to analyze the position of the shorts. The purely geometric segments corresponding to the minimum distance between two neighboring surfaces were also plotted on this graph. It clearly appeared that the breakdown tree very often followed these segments, especially those oriented in the direction of the electric field (vertically). In summary, the analysis of the simulated breakdown trees in the quasi-homogeneous field corroborated (i) the large influence of the particles on the initiation of the breakdown and (ii) the resulting even distribution of the damage. The particles thus qualitatively favor the initiation of

breakdown trees in plane-plane configuration. As a result, the field to breakdown is found with the simulation to be lowered for the composite as compared to the neat matrix, Fig. 5.21.

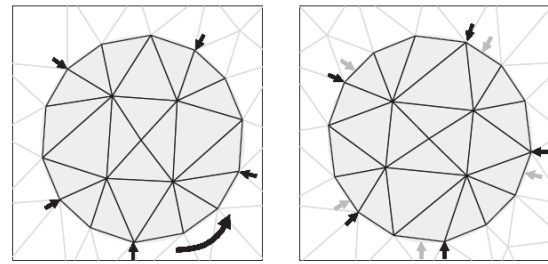


Figure 5.19 : Schematic representation of the method proposed to obtain various meshes from a single image: initial mesh obtained from the particle's geometry (left) and another mesh for the exact same particle (right). (The arrows are added to guide the eyes.) [Source: (109)]

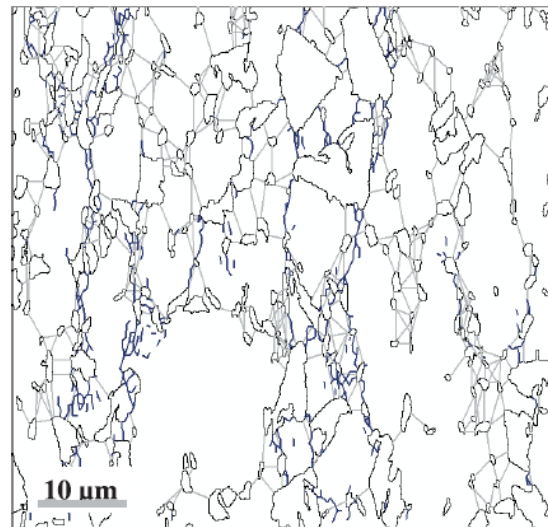


Figure 5.20 : Interrelation between minimum particle distance (light gray) and breakdown tree (dark gray) in a plane-plane electrode arrangement. [Source: (109)]

As already mentioned above, in the case of divergent configuration, the electric field is initially localized at the tip of the needle electrode. The final structure of the tree (roughly one dimensional channel) clearly shows that a strong localization is kept during the whole breakdown process. This statement was also found in the simulation, thanks to the high conductivity of the damaged tree as compared to both filler and matrix. It was however also evidenced that the field localization was largely reduced whenever the tree reached a particle (which was assumed to be 10

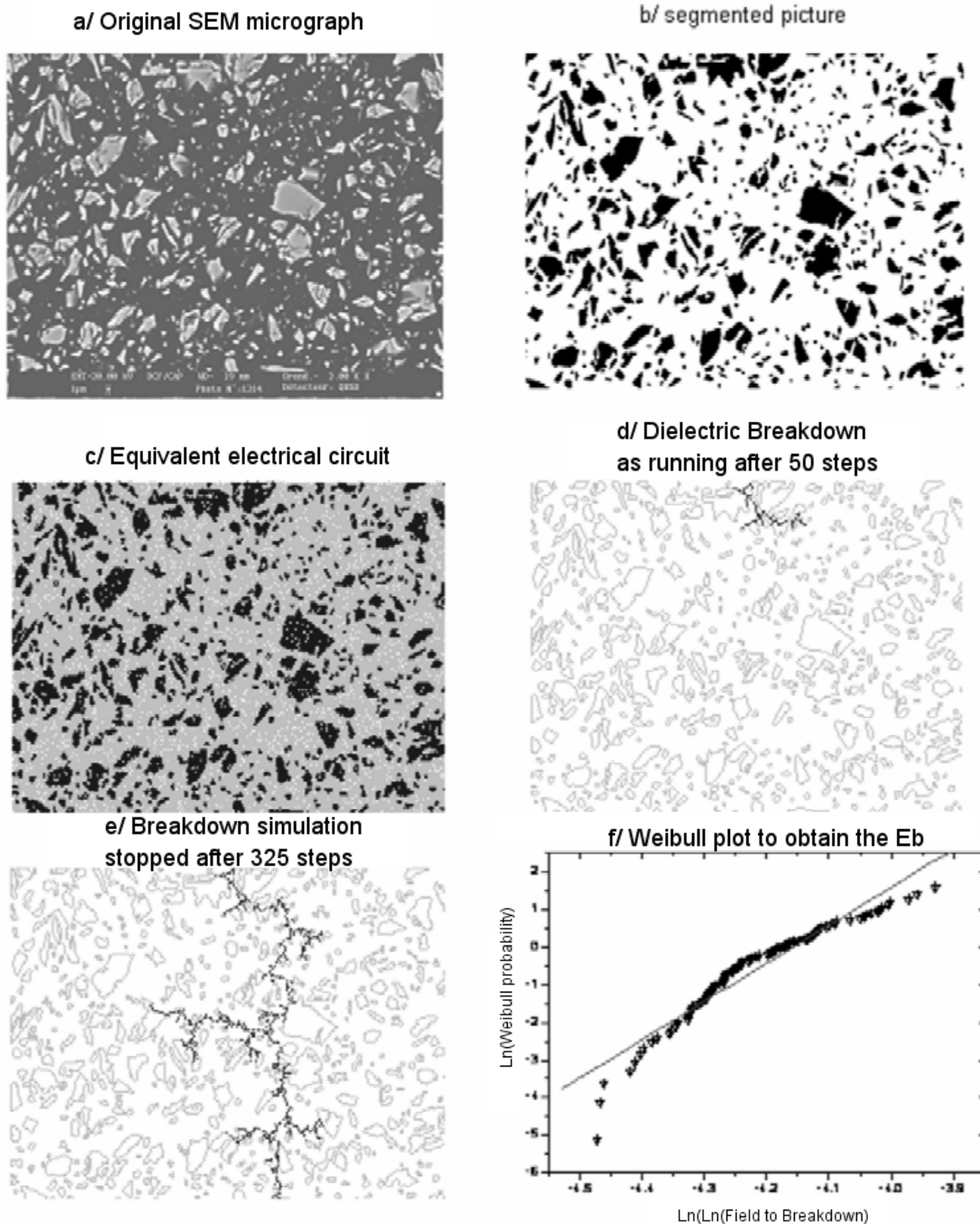


Figure 5.18 : The steps of simulation of breakdown trees in heterogeneous materials (case of composite $C2$ in point-plane configuration). (a) SEM original Photomicrograph, (b) segmented picture, (c) equivalent network, (d) dielectric breakdown simulation (as continued after 50 steps), (e) dielectric breakdown simulation (as stopped after 325 stages) and (f) Weibull plot to obtain the field to breakdown [Source: (109)] .

times more conducting than the matrix). The growing tree thus presented overall two opposite behaviors toward the fillers; on the one hand a strong attraction due to their high conductivity which induce field gradients and, on the other hand a repulsion when touched related to the decreases in field enhancement. This lead to complex pattern and branching displayed on Fig. 5.18-e. Moreover this “attract-then-barrier” phenomenon resulted in a higher field to breakdown of the composite, as compared the pure polymer in the simulation, Fig. 5.21. Here again, the intrinsic electrical properties of the two phases was sufficient to semi-quantitatively explain the macroscopic field to breakdown measured experimentally. It was in particular striking that neither the thermal effect had nor gradients in physical properties had to be considered.

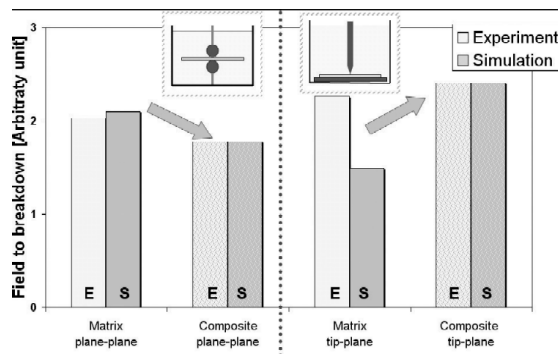


Figure 5.21 : Dielectric breakdown field obtained from experiments (E) and simulation (S) for both systems M2 and C2 systems in both quasi-homogeneous and divergent fields. [Source: (109)]

5.3.3 Concluding remarks

This study was first concerned with the influence of the degree of curing (α) on the field to breakdown of epoxy-mineral filler composites. By studying a set of sample with α ranging from 0.95 to 0.995, an almost linear increase in the breakdown field was evidenced in both divergent and quasi-homogeneous field. A much larger sensitivity was however measured in the divergent configuration.

In a second step, an innovative SEM study of the structure of the conducting tree revealed that under divergent configuration, the field initially enhanced at the point electrode remained localized at the tip of the growing tree during the whole breakdown process. As a result, a pseudo-linear tree was observed similar in nature to that evidenced for a neat epoxy⁽⁹⁶⁾. On

the contrary a more global breakdown of the structure was observed in a quasi-homogeneous field configuration that most likely resulted from much lower field localization. From these statements it was proposed that the pertinent parameter was the scale at which the breakdown nucleates in the two configurations:

1. In sphere-sphere configuration, a quasi-homogeneous field is perceived all over the piece. The damage may thus equally initiate at any place within the structure, and hence first take place in the vicinity of the major flaws. The quasi-homogeneous configuration should as a consequence correspond to a “Global Weakest Link” (*GWL*) at the whole sample scale.
2. On the contrary, in point-plane configuration, a divergent field is largely enhanced around the tip of the point electrode. The damage tree thus preferentially starts in the vicinity of this electrode, almost independently from the flaws too far away from it. The divergent configuration should thus correspond to a “Local Weakest Link” (*LWL*) accompanied by a major cumulative process.

It is thus striking that the fillers play a major role on dielectric breakdown of these composites that depends on the electrode configuration. It was then decided to compare the breakdown properties of these composites to that of the neat matrix in both configurations. An interesting ‘composite effect’ was evidence which depend on the nature of the electric field: in a quasi-homogeneous field the reinforcing particles behave as flaws and decrease the dielectric strength of the considered epoxy whereas the same particles seem to prevent the degradation of the polymer network when placed in a divergent field.

To further understand this composite effect, a purely electric model of the breakdown was developed. The analysis of the simulated breakdown trees in the quasi-homogeneous field corroborated (i) the large influence of the particles on the initiation of the breakdown and (ii) the resulting even distribution of the damage. The particles thus qualitatively favoured the initiation of breakdown trees in plane-plane configuration and the field to breakdown was found to be lowered for the composite as compared

to the neat matrix. Moreover in the divergent configuration, an “attract–then–barrier” phenomenon resulted in a higher field to breakdown of the composite, as compared the pure polymer in the simulation. The intrinsic electrical properties of the two phases, when properly combined with their relative arrangements, were thus sufficient to semi–quantitatively explain the macroscopic fields to breakdown measured for the whole set of data.

In this type of experiments it seems that bigger particles with higher electrical conductivity would be required to further improve the field to breakdown in a point–plane configuration. This later statement obviously presents some limitations and it could be of peculiar interest to investigate its range of validity and the influence of the particles geometry and volume fraction on the breakdown behavior of these useful composites.

Chapter 6

Relative influence of the physical and chemical aging on high voltage properties

⊙ **Abstract** ⊙

Aging of epoxy based composite used as insulators in the industry are investigated. Two sets of samples were investigated: (i) a rare sample that aged 20 years in service and faced numerous constraints (environmental, electrical, thermal, mechanical, etc.) and (ii) composites aged in laboratory with the sole influence of the temperature. First, a detailed analysis of the changes in properties during aging is proposed. Then, the series of well characterized samples is tested for dielectric breakdown. During the characterization of the physico-chemical properties, it was essentially concluded that the insulator aged twenty years in actual service conditions underwent both a severe chemical degradation and a large structural recovery of the polymer network (“physical aging”). This composite exhibited however a breakdown field comparable to that of a fresh sample with the same formulation. The sole physical aging showed proved to largely increase the voltage to breakdown of the newly processes composite over time. This improvement was attributed to a densification of the thermoset resin, which prevented the tree initiation and/or growth. It was additionally observed that the choice of the electrode geometry greatly altered the measurements. In a quasi-homogeneous field configuration, the breakdown was mainly governed by the major flaws at the sample scale, namely the reinforcing particles. On the contrary, under a divergent field (with a point –plane electrode arrangement), the field was essentially localized at the point electrode tip, and the major flaws might not be reachable by the damage tree. It hence appeared that the measurements performed in a quasi-homogeneous field are not very sensitive to the variations within the polymeric matrix as are the measurements under a divergent field. In conclusion a quantitative analytic model is proposed that summarizes all the experiments performed in High Field.

Contents

6.1	Structural changes induced by aging	78
6.1.1	Introduction	78
6.1.2	Experimental	79
6.1.3	Results and discussion	80
6.1.4	Conclusion	87
6.2	Consequences on high voltage properties	88
6.2.1	Results and Discussion	89
6.2.2	Conclusion	94

6.1 Structural changes induced by aging

6.1.1 Introduction

Epoxy based composites are commonly used as insulator in demanding applications because of their ability to withstand high electric field over long periods of time⁽⁸⁸⁾. The multi-stress constraints in service is however likely to generate structural modifications after long-term in service. The aging of these composites may reduce their reliability and jeopardize the whole structure. It seemed thus of interest to understand and try to predict the structural changes of these composites when submitted to high electric field over long periods.

The aging procedure may not solely consider the effect of temperature. For example, Ollier-Dureault *et al.*⁽¹⁰²⁾ showed that the superimposition of both electric stress and UV irradiations of epoxy based composites result in generation of carbonyl functions through a decarbonylation of the product stemming from photo-oxidation. However, the thermal degradation is crucial in the aging process of these composites and will be an important part of the present study.

Because of the low thermal conductivity of polymer network, the application of high electric field induces local temperature raises by Joule effect⁽⁹⁹⁾. Depending on the magnitude of these temperature increases, two kinds of structural modifications of the polymer network might be considered:

(i) when the temperature T reached is higher than the glass transition temperature T_g of the polymer, chemical degradations of the polymer might occur such as chains scissions, formations of polar groups or recombination of chain segments^(102;103;104;160;161).

(ii) for $T < T_g$, the so-called physical aging of the amorphous phase occurs over time, resulting in a densification of the polymer network. The physical aging originates from the metastable state of amorphous materials below T_g . Vitreous materials indeed exhibit enthalpy, entropy and specific volume excesses with respect to their respective values at the thermodynamic equilibrium for a given temperature. Accordingly, vitreous materials kept at temperatures below T_g , tend to reach the thermodynamic

equilibrium over time. As a result, all thermodynamic parameters (enthalpy, entropy and specific volume) exhibit a non-linear decrease as a function of time^(162;163). This evolution is the well-known structural recovery. From a microstructural point of view, the physical aging results in a network densification over time and leads to an increase of the brittleness of the material⁽¹⁶⁴⁾. Because of the difficulty to accurately evaluate changes in specific volume, the physical aging is usually quantified by calorimetric measurements. On the first heating run performed after aging, aged polymers exhibit an endothermic peak near but above T_g . The amplitude of this endothermic peak is generally used as the right parameter to quantify the structural relaxation. Montserrat *et al.*^(100;143;144;145;146;165;166;167;168) studied the influence of the aging temperature ($T < T_g$) on kinetics and magnitude of the enthalpy relaxation phenomenon.

If the polymer is cooled below its T_g , the relaxation process is fast, but its amplitude is small because. For aging temperatures much lower than T_g the molecular mobility becomes the limiting factor and the relaxation may take months, years or even never complete. There is thus an optimum temperature for isothermal aging, with the present sample it was in the literature that the “fasted aging” temperature was close to $T_g - 18^\circ\text{C}$ ⁽¹⁰⁰⁾.

Few investigations⁽⁸⁸⁾ are reported in literature concerning the influence of the physical aging on the dielectric properties of composite materials. Beyer⁽¹⁰¹⁾ investigated the dielectric behavior of filled and unfilled epoxy first submitted to high electric field. According to this author, the dielectric losses increase with the amplitude of the electrical field. This effect is magnified with the unfilled materials. The author did not propose a definitive explanation to this evolution, but it seems reasonable that this effect originated from the formation of polar groups resulting from chemical degradations of the polymer. However the possible contribution of physical aging to the changes in material behavior cannot be excluded.

In this chapter, it is first proposed to investigate the microstructure and electrical properties of a composite used as an insulator in actual service conditions for 20 years and which was submitted over this long time to various stresses. Then, in order to separate the relative contributions of chemical and physical aging on both microstructure and dielectric behavior, physical

aging tests are performed under laboratory conditions on composites with similar compositions.

6.1.2 Experimental

6.1.2.1 Materials

As received materials: The resin and the hardener in this study were respectively a DiGlycidyl Ether of Bisphenol A (DGEBA) and an anhydride. Two systems of particle-filled composites were studied (Table 6.1). The so-called *C1* and *C2* materials were reinforced with $58.0 \pm 0.5\text{wt.}\%$ and $67.0 \pm 0.5\text{wt.}\%$ mineral particles, respectively. *C2* is the same as the one presented in the former chapter. The two composite were processed with different mineral filler, similar in chemical nature, but with noticeably different shapes. The somewhat difference in chemical nature of the two matrices also lead to slightly different T_g 's.

Despite the different components (resin, hardener and fillers), both systems were basically processed by the same way. The inorganic fillers were dried by placing them into an oven at 60°C for 48 h to reduce as much as possible the influence of water. The resin, the hardener and inorganic materials were then mixed and stirred at 56°C and degasified under vacuum. The mixture was then injected under pressure at the bottom of a vertical mold and underwent the cure process at 140°C for 15 minutes for both composites *C1* and *C2*. The composites were then post cured 8 hours at 140°C and 12 hours at 60°C in order to fulfill the cross-linking reaction.

Composite aged in actual service A composite similar to *C1*, but aged 20 years in actual service, was supplied by Areva T&D. This material, referred to as *C1** (Table 6.1) has experienced multi-stresses (electrical, thermal and mechanical as well as environmental constraints) over this long service period.

6.1.2.2 Laboratory aging

Physical aging was carried out on the as received materials, i.e. the *C1* and *C2* composites. The aging temperature was chosen to be $T_g - 18^\circ\text{C}$ ⁽¹⁰⁰⁾ in order to induce significant physical aging within a limited period of time. Aging was performed in an oven under nitrogen atmosphere to reduce the risk of chemical modifications. For each material, aging periods

ranged from 9 hours to 6 months. Seven samplings were taken out during these 6 months (Fig 6.1).

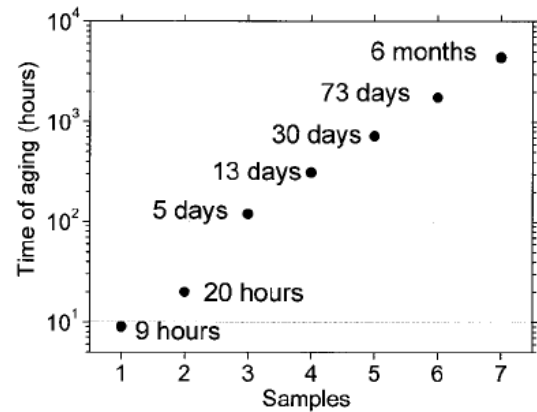


Figure 6.1 : Samples for aging times ranging from 9 hours to 6 months [Source: (169)] .

6.1.2.3 Methods

Differential Scanning Calorimetry Differential Scanning Calorimetry (DSC) analysis was carried out by using a DSC 7 Perkin Elmer device. The calorimeter had previously been calibrated with the indium standard. The analysis was then carried out with samples containing 10 ± 1 mg of polymer. Thermograms were recorded under nitrogen atmosphere from 40°C to 170°C . Heat flows were measured at a heating rate of $10^\circ\text{C}/\text{min}$. For each sample, two successive heating runs were carried out with a 5 minutes hold stage at 170°C between each scan in order to erase the previous thermal history. From the thermogram recorded on the first heating run, the enthalpy excess related to the magnitude of the previous physical aging was determined. A second heating run was performed at a heating rate of $10^\circ\text{C}/\text{min}$, in order to verify that the first heating run followed by the hold stage at 170°C did not induce any chemical degradation. The DSC experiments were carried out twice on each sample ($n=2$). With these composites, T_g is taken as the onset value at which the thermogram splits from the base line, as defined in 5.2.1.3, page 61.

The exact polymer-filler weight ratios were corrected a posteriori thanks to Thermogravimetric Analysis (TGA) measurements performed on the samples used in DSC. Several trials to directly reveal the increase in density due to physical aging of polymer were performed. The estimation of the actual density

		<i>C1</i> and <i>C1*</i>	<i>C2</i>
Polymer		Matrix M1	Matrix M2
	Granulometry	2-40 μm	3-30 μm
Filler	D50	6 μm	6.6 μm
	Shape	lenthgened	irregular
	%w	58 \pm 0.5	67 \pm 0.5

Table 6.1 : Main characteristics of the epoxy-based composites utilized in this study.

of the polymer remained however too sensitive to the amount of inorganic filler. The Fig. 6.2 does however guaranty the best quantification of the physical aging process.

The Tg values measured on the second DSC scans (rejuvenated samples) remained constant for the entire set of aging times and for a given composite. It was thus concluded that no significant chemical modification of the polymer was imparted by the laboratory aging (see ⁽¹⁶⁹⁾ for details)

Dielectric thermal analysis Dielectric measurements were performed on parallelepipedic samples (25x25x3mm³) under low electric field by using a dielectric spectrometer (4284A Hewlett Packard). The principle is to apply a 1V AC voltage to the sample and to record the dielectric permittivity (real (ϵ') and imaginary (ϵ'') parts and the loss angle $\delta = \epsilon''/\epsilon'$) as a function of temperature and/or frequency. ϵ' will be reported here as a function of temperature and/or frequency.

Analyses were carried out in a frequency range from 100 Hz to 1MHz and for temperatures ranging from 30 to 300°C. For each sample, two successive isochronal scans were performed. Uncertainties in permittivity values mainly result from sample dimension measurements. In order to avoid surface problems the sample were metallized by a thin aluminum layer of 1.0 ± 0.2 μm thick by using cathode vaporization treatment.

Scanning Electron Microscopy Morphology analysis was performed with the help of a scanning electron microscope Stereoscan 440 Leica. Samples were broken and the surface fracture was covered with a thin gold layer by cathode vaporization. This technique allows detecting some particle debonding tendency from polymer matrix that could be related to the strength of interactions at the polymer/particle interface.

Dynamic mechanical analysis The dynamic mechanical analysis was carried out on both the 20 years aged material, *C1**, and on the corresponding unaged composite material, *C1*, in order to characterize the structural changes that could occur on heating at temperatures higher than Tg.

By using the Rheometric Scientific DMTA MK III analyzer, the viscoelastic spectra were recorded from 30 to 300°C, with a heating rate of 1°C/min under nitrogen atmosphere. The device was used in a three point bending mode under isochronal conditions at frequencies of 0.3, 1, 3, and 10 Hz. The samples were 1.5 mm thick, 5 mm wide and 45 mm long. In this paper, only the evolution of the real part of the Young's modulus vs. temperature at 10Hz recorded for both materials will be reported.

6.1.3 Results and discussion

First, in order to analyze the resulting effects of multistresses undergone by an insulator experienced under actual service conditions over a long time, microstructure and subsequent properties of a composite material aged for 20 years under actual service conditions are investigated.

6.1.3.1 20 years aged insulator

Microstructure investigated by DSC Fig. 6.2 shows the thermograms of the 20 years aged material (*C1**) recorded on two successive heating runs. For comparison, the thermogram displayed by the as received material *C1* was also plotted.

Aging in actual service conditions leads to the two following effects:

(i) on the first heating run, the aged material exhibits a large endothermic peak attributed to the

physical aging undergone by the insulator over 20 years,

(ii) comparing the thermogram displayed by the aged material on the second heating (rejuvenated sample) to that of recorded in the same conditions for the as-received material, it can be observed that Tg of $C1^*$ is significantly shifted towards the lower temperatures. This behavior can be attributed to some chemical degradations of the polymer network, as for example, chain scissions or uncrosslinking effects.

In order to identify the nature of these molecular structure modifications induced by aging, FTIR analyses^(103;104) have been carried out on these samples. Unfortunately, recorded spectra show low signal magnitude because of the high amount of inorganic particles. Accordingly, it was not possible to accurately evaluate the exact nature of the chemical modifications.

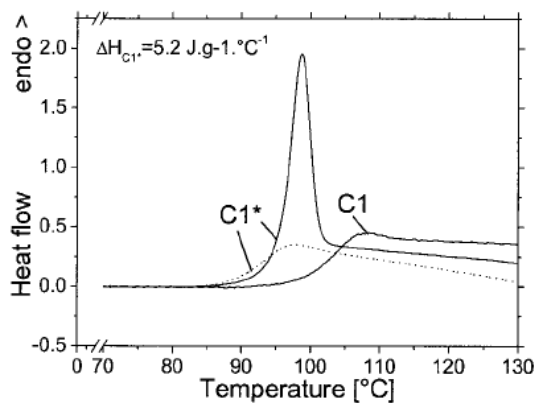


Figure 6.2 : Thermograms recorded for the as received material, $C1$ (second heating run), and for the 20-years-aged material, $C1^*$,—first (solid lines) and second (dashed line) ramp of temperature [Source: (169)] .

To confirm the above-described structural changes, the microstructure of the epoxy matrix will now be analyzed in terms of molecular mobility with dynamic mechanical analysis.

Microstructure investigated by DMTA

Fig. 6.3 shows the plots of the normalized real parts of the Young's modulus $E'/E'0$ (where $E'0$ is the modulus at 50°C) vs. the temperature at 10Hz displayed by the $C1$ and $C1^*$ materials.

The following features can be pointed out:

(i) the drop in the modulus characteristic of the main relaxation related to Tg exhibited by the aged

composite is shifted towards the lower temperatures with respect to that displayed by the as-received material. This is consistent with DSC data, i.e. Tg of aged material is located at a lower temperature than the Tg of fresh composite because of some chemical degradations made of chain scissions, for example, have occurred on aging in service conditions.

(ii) for temperatures higher than 190°C, a significant raise in the Young's modulus was observed on the aged material whilst the fresh one only showed a slight increase in its stiffness. This is consistent with additional chain cross linking effects such as chain recombination that can occur on heating, and involving non-reacted groups and molecular species issued from the chemical degradations.

Dynamic mechanical features were thus consistent with DSC results and pointed out the chemical degradations that occurred in service. No influence of the physical aging on the molecular mobility could be detected by dynamic mechanical analysis because of the expected decrease in molecular mobility due to structural aging are counterbalanced by the increase in molecular motion related to chain scissions.

Morphology analysis In order to complete these microstructure investigations, scanning electron microscopy observations were performed on fracture surfaces of both $C1$ and $C1^*$ materials (Fig. 6.4).

It can be observed that fracture surfaces displayed by the aged material exhibit particle debonding tendency from the polymer matrix, in contrast to that exhibited by the as-received material.¹ This could indicate relatively weak interactions at the inorganic filler/polymer network interface. The poor adhesion between polymer and fillers might result from the physical and/or chemical changes induced by multi-stresses undergone by the insulator over a long time period.

Dielectric behavior The dielectric behavior of this aged material is now analyzed in order to determine the influence of the changes in microstructure (including the interface modifications) on the permittivity.

Fig. 6.5 shows the evolutions of the real part of the permittivity (ϵ') vs. temperature at 1kHz recorded

¹ These observations were obviously difficult to quantify, however a "blind test" performed with people unaware of the study confirmed a noticeable difference. Everyone could differentiate between the pictures.

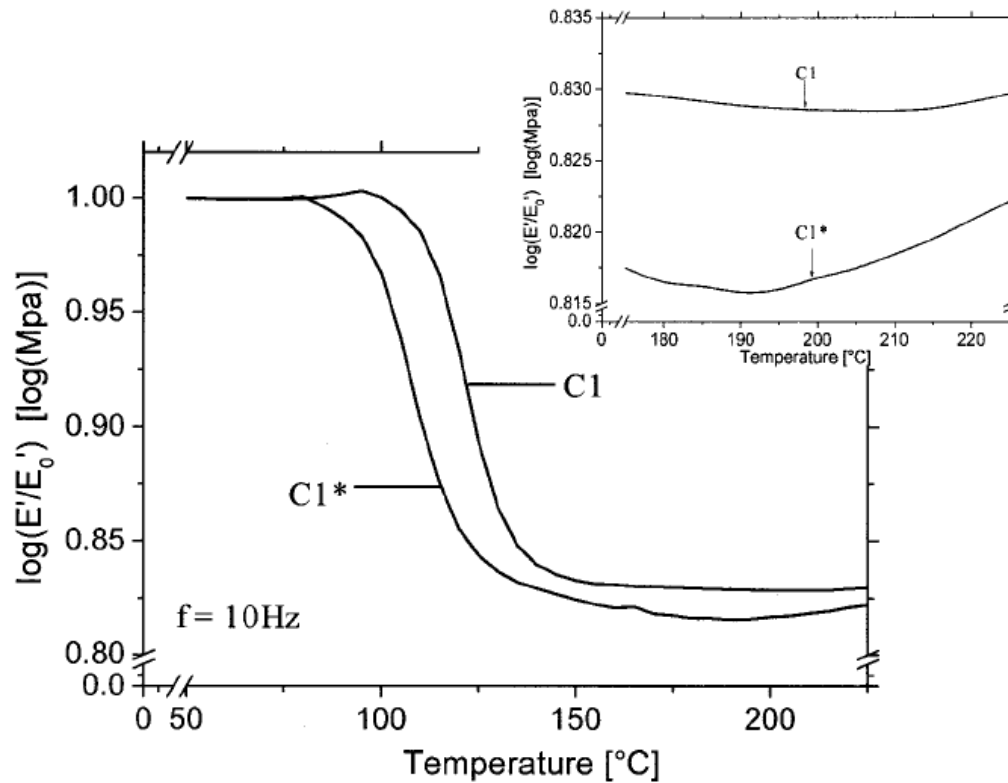


Figure 6.3 : Real part of the dynamic mechanical modulus(E') vs. temperature shown by the $C1$ and $C1^*$ samples at 10Hz [Source: (169)] .

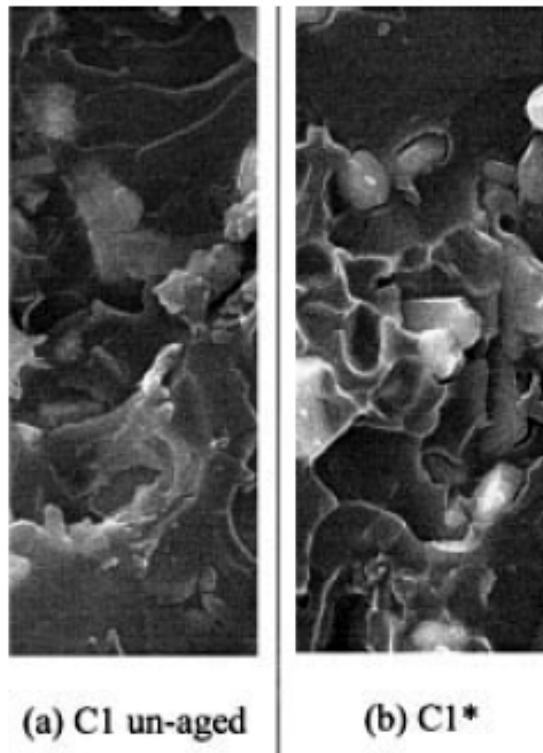


Figure 6.4 : SEM observations of fracture surface for as-received (a), and aged (b) composites [Source: (169)] .

on two successive heating runs for both aged and as-received composites. Materials exhibit similar dielectric properties on the first and second heating runs.

The first increase in ε' occurring near 110°C is attributed to the main relaxation ($T\alpha$) related to T_g . For the aged material, $T\alpha$ is located at a lower temperature than $T\alpha$ recorded for the as received sample. This feature is consistent with DSC (and dynamic mechanical) analysis showing a shift of T_g (and the main mechanical relaxation) towards the lower temperature for $C1^*$.

However, permittivity values of the aged sample recorded at 50°C and at various frequencies are not significantly different from those determined for the unaged sample in the same conditions (Fig. 6.5). This was unexpected because of the clear chemical degradation that was evidence in the $C1^*$ through DSC, Fig. 6.2. The chemical degradation should induce the formation of polar species and result in a significant increase in ε' at room temperatures. This unexpected behavior might originate from the superimposition of opposite effects and this will be discussed later in this manuscript (Fig. 6.13).

Moreover, it can be observed that on the first heating runs, $C1$ and $C1^*$ samples exhibit both a maximum in ε' close to 180°C for all measured frequencies.

This ε' peak shows no frequency dependence and is not detected on the second heating run, i.e. after the first heating run up to 300°C and cooling. This maximum in ε' can thus originate from (i) the presence of polar species (including water molecules) and/or (ii) some structural evolution (including chain recombination) of the polymer network.

Because of the shift of the main relaxation towards higher temperatures detected for the two composites on the second heating run, this ε' maximum is consistent with additional chain crosslinkings, i.e. with structural modification of polymer network. It is also consistent with the dynamic mechanical analysis showing a significant increase in the aged material stiffness at about the same temperature and characteristic of some chain recombination.

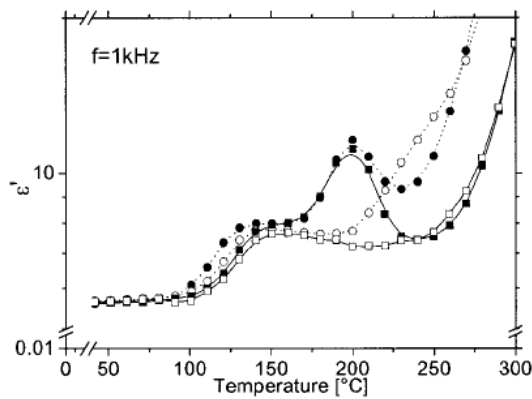


Figure 6.5 : Dielectric permittivity ε' vs. temperature recorded for $C1$ (■^{1st}, and □ second heating ramp) and $C1^*$ (●^{1st}, and ○^{2nd} heating ramp) at 1kHz. [Source: (169)]

The strong rise in ε' value displayed by $C1$ as $C1^*$ composites at high temperatures, i.e. at temperatures higher than 200°C (Fig. 6.5), is usually attributed to the diffusion of large polar species (170).

In this temperature range, the ε' values displayed by the aged composite are always higher than that exhibited by the as-received sample for a given temperature and frequency. In order to better compare the dielectric behaviors of these two materials at high temperatures, plots of ε' vs. frequency recorded at 230°C are shown in Fig. 6.6.

For both materials, the permittivity first decreases with increasing the frequency and then reaches a

plateau for higher frequencies, thus defining a critical frequency (ν). To interpret this behavior, two mechanisms can be proposed:

(i) At low frequency, the high ε' values displayed by composites can result from the presence of mobile polar species. For a given frequency, ε' value displayed by the aged material is higher than that of measured for the as-received sample. This is consistent with higher number and/or higher mobility of polar species shown by the aged material because of the chemical degradation of the polymer matrix induced by the aging in service.

(ii) With increasing frequency, the decrease in ε' displayed by both materials could be related to the progressive decreasing number of polar groups able to align along the alternating electric field direction. For frequencies higher than these critical values, polar groups can not follow the alternating electric field any longer.

It can be observed that critical frequencies displayed by both $C1$ and $C1^*$ materials respectively show no thermal history dependence. In addition, it is found that ν_{C1^*} for the aged material is almost one order higher than ν_{C1} recorded for the fresh material under the same conditions. This critical frequency can thus be employed as a probe of the aging effects undergone by the composites.

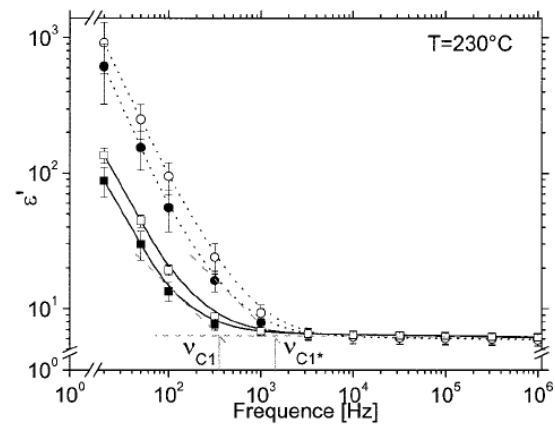


Figure 6.6 : Dielectric permittivity ε' vs. frequency recorded for $C1$ (■^{1st}, and □ second heating ramp) and $C1^*$ (●^{1st}, and ○^{2nd} heating ramp) at 1kHz. [Source: (169)]

To conclude, from a structural point of view, the aging in actual service conditions of an insulator based on epoxy resin reinforced by inorganic particles resulted in the followings effects:

1. a chemical degradation of the polymer matrix involving the formation of polar species,
2. a densification of the epoxy network due to the physical aging,
3. reduced interaction magnitude at the interface polymer/inorganic particles.

The comparison between the dielectric behaviors displayed by the aged and the as received materials can be summarized as follows:

1. at 230°C and for a given frequency, aged material exhibits higher ϵ' values and a shift of the critical frequency, ν_C , towards higher values. This can originate from higher number and/or higher mobility of polar species resulting from the chemical degradation of the polymer matrix occurring over a long service period.
2. the aged material exhibits no increase in ϵ' value measured at 50°C. This unexpected issue could result from opposite effects involving physical and chemical agings.

From these investigations, it is difficult to separate the relative contribution of the chemical aging from that of the physical aging on the overall structural changes and related dielectric properties shown by the composites.

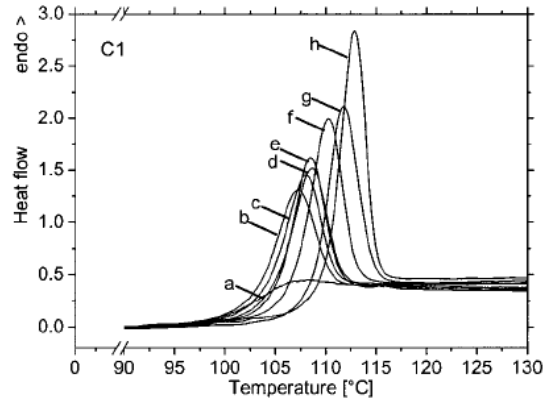
In order to evaluate the sole influence of physical aging on the microstructure including the polymer/particles interface of epoxy based composites and subsequently on the dielectric properties, laboratory structural aging tests were carried out.

6.1.3.2 Laboratory aging

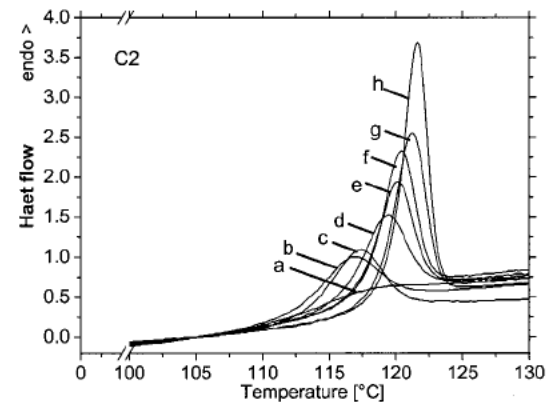
Over a 6 months period, the *C1* and *C2* composites were sampled for various aging times.

It was first required to verify that no chemical degradation occurs over time before discussing the influence of the physical aging of the materials. From the thermograms recorded on the second heating runs (rejuvenated samples), it can be observed that T_g remains almost constant regardless of the aging time. This was consistent with a minor or no chemical degradation during the physical aging.

Microstructure Evolution -Aging kinetics of the epoxy network For all samples, the thermograms immediately recorded after aging exhibit an endothermic peak whose magnitude increases with the aging time associated with a shift of T_g towards the higher temperatures, Fig. 6.7.



(α)



(β)

Figure 6.7 : Thermograms of as-received systems (a) and composites aged under laboratory conditions for (b) 9h, (c) 20h, (d) 5days, (e) 13 days, (f) 30 days, (g) 73 days, (h) 6 months -1^{st} heating run for the composites *C1* (α) and *C2* (β) [Source: (169)] .

Aging kinetics can be evaluated^(100;162;171) by plotting both T_g agedie, T_g onset of aged composites (Fig. 6.8–a), and the related enthalpy excess ΔH , (Fig. 6.2–b) recorded on the first heating run vs. aging time.

With increasing aging time up to 30 days, *C1* and *C2* composites first exhibit a linear shift of $T_{g_{aged}}$ towards the higher temperatures accompanied by a linear increase in the enthalpy excess with time. Then, for aging periods ranging from 30 days to 6 months,

the slopes of T_{gaged} and ΔH curves vs. aging time significantly increase. Based on data reported by Montserrat⁽¹⁰⁰⁾, ΔH and T_g are expected to reach constant values for long aging periods. In agreement with Kovacs⁽¹⁶²⁾ and Bauwens⁽¹⁷¹⁾, such an evolution of the enthalpy excess with aging time at $T_g - 18^\circ\text{C}$ clearly shows that the structural relaxation also called structural recovery is a non-linear phenomenon. Accordingly, it can be suggested that for aging times longer than 6 months at $T_g - 18^\circ\text{C}$, polymer networks in the $C1$ and $C2$ composite materials have almost reached their respective structural equilibrium states.

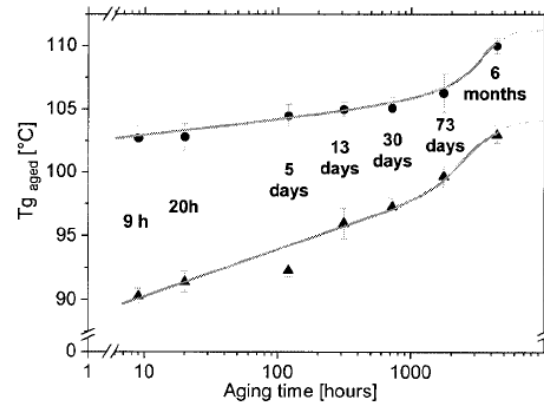
Thus, as described before in the introduction, such an evolution is related to a progressive and non-linear increase in density undergone by the polymer⁽¹⁶⁴⁾.

Dynamic mechanical analyses performed on the physically aged materials confirm that no chemical degradations of the polymer have occurred over time. Moreover, only a slight shift of the main relaxation towards the high temperatures is found with increasing aging time. Because of the experimental uncertainties, the expected increase in the vitreous Young's modulus for aged materials has not been detected.

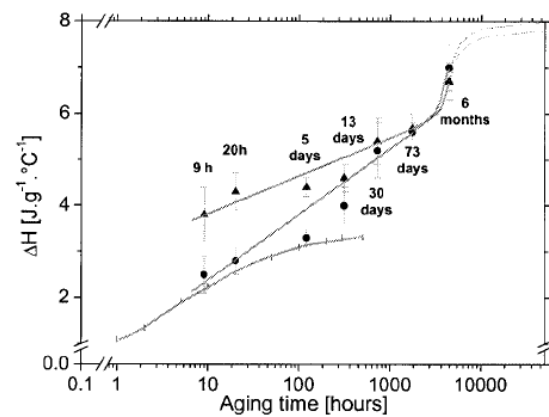
Dielectric behavior As for example, Fig. 6.9 shows the evolution of the real part of the permittivity ε' vs. temperature displayed by the $C1$ composite aged for various times ($C2$ composite exhibits a similar evolution).

At $T_g - 18^\circ\text{C}$ and for the longest aging times, the main relaxation located near 110°C at 320 Hz is significantly shifted towards the higher temperatures. Such an evolution points out the decrease in the molecular mobility of chains segments of the polymer network due to the decrease in free volume accompanying the structural recovery.

The maximum in ε' located at about 170°C exhibited by both composites is related to additional chain crosslinking reactions involving unreacted species. It can be noticed that the ε' maximum shown by the 6 months-aged material is located at a much higher temperature than that of displayed by the unaged sample. This can be related to the shift of T_g towards the higher temperatures displayed by the aged material. As a matter of fact, additional chain crosslinking based on thermally activated diffusion of unreacted



(a)



(b)

Figure 6.8 : Evolutions of T_g (a) and enthalpy excess ΔH (b) values as a function of aging time for the composites $C1$ (\blacktriangle) and $C2$ (\bullet). For comparison the values reported by Montserrat⁽¹⁰⁰⁾ on a similar formulation as $C2$ were added to the graph (+). [Source: (169)]

species should occur at even higher temperature than that of displayed by the unaged material.²

For higher temperatures, it can be noticed that the strong increase in ε' vs. temperature related to the mobility of polar species displayed by both composites shows no significant aging time dependence. This is consistent with no chemical degradations of the polymer network induced by physical aging.

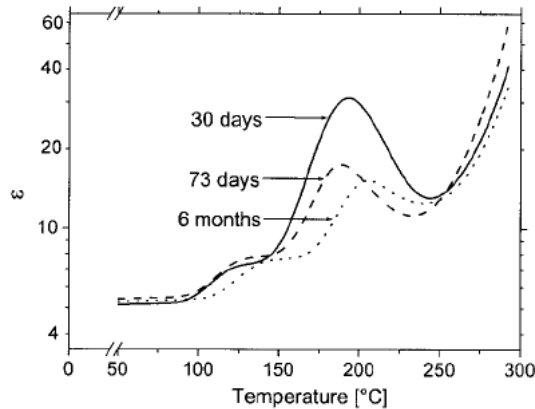


Figure 6.9 : Plots of dielectric permittivity ε' (1st heating run) vs. temperature at 320 Hz of the aged composite C1 for (—)30 days, (---) 73 days and (...) 6 months. [Source: (169)]

Now, the influence of the microstructural changes, *i.e.* the densification of the polymer network and the decrease in the polymer/fillers adhesion quality, induced by physical aging on the permittivity at insulator service temperatures are analyzed.

For example, plots of ε' vs. aging time measured at 50°C for various frequencies ranging from 100Hz to 1 MHz are shown in Fig. 6.10 and Fig. 6.11 for both composites.

With increasing aging time up to 73 days, both composites exhibit an increase in the real part of the permittivity for over the analyzed frequency range. It can be noticed that ε' values measured for sample aged for 6 months tend to be slightly but significantly lower than that those determined for the 73 days aged sample. Such an evolution suggests that ε' could have

²It seemed that the maximum of ε was somehow related to a “post-curing” of the epoxy network. This seemed reasonable because, it started just above the highest temperature achieved during the process. In addition, this peak could slowly be “erased” by ramping to higher progressively temperatures in the DSC. It seemed however beyond the scope of this study to further investigate if the samples could “post cure” below T_g . Even though the mobility is high enough for the samples to relax.

gone through a maximum for aging time ranging between 73 days and 6 months. The influence of the physical aging in the dielectric behavior of insulators in service conditions can be interpreted as follows:

The increase in ε' with increasing aging time up to 73 days may arise from the two following origins:

(i) the decrease in the volume induced by the structural recovery occurring on physical aging and leading to an increase in the relative volume ratio of molecular dipoles.

(ii) the presence of the polar species in the polymer network that can migrate to the polymer/filler interface over time leading to the formation of a “polar interphase”. The comparison between the dielectric behavior of unaged and aged composite suggests that the formation of such a “polar interphase” could be favored by the poor quality of the polymer/filler adhesion at the interface induced by the structural recovery occurring over aging time, Fig. 6.12. The decrease in ε' detected for both composites aged for 6 months could result from the diffusion and the removal of volatile polar species favored by long aging time.

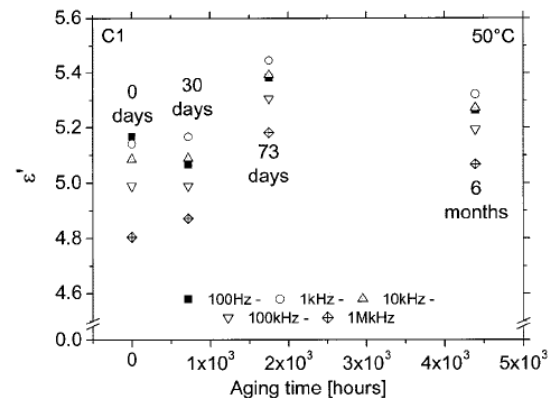


Figure 6.10 : Evolution of dielectric permittivity ε' (1st heating run) vs. aging time for the sample C1 unaged and aged for 30 days, 73 days 6 months, at 50°C and at several frequencies (ranging from 100Hz to 1MHz). [Source: (169)]

To elucidate the unexpected ε' value displayed at 50°C by the insulator aged in actual service conditions for 20 years, *i.e.* ε' is found to be not significantly different from the permittivity measured on the fresh material in the same conditions, while, it was expected to increase because of the presence of polar species, the dielectric behavior of the 20 years aged material is compared to those displayed by the laboratory aged samples, Fig. 6.13.

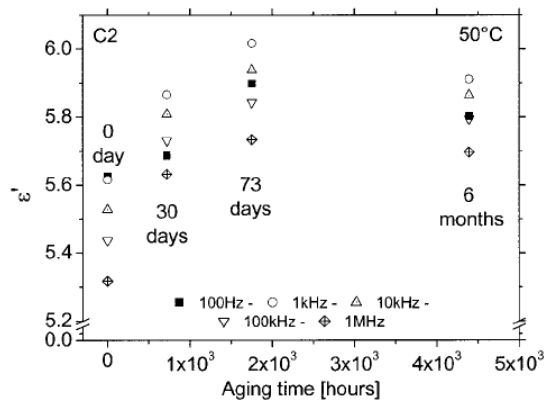


Figure 6.11 : Evolution of the dielectric permittivity ϵ' (1st heating run) vs. aging time for the sample C2 un-aged, aged 30 days, 73 days 6 months at 50°C and at several frequencies (ranging from 100Hz to 1MHz). [Source: (169)]

It can be observed that ϵ' values at 50°C shown by the C1* composite are very close to those displayed by both the unaged and 30 days aged C1 materials.

Based on the previous analysis of the evolution of ϵ' vs. laboratory aging times (Fig. 11) it can be suggested that the aging in actual service conditions results in two opposite effects on the dielectric behavior displayed by C1* at 50°C.

According to the first mechanism, ϵ' exhibited by the 20 years aged material at 50°C is expected to strongly increase because of the structural recovery that induces an increase in the amount of dipole per unit volume and/or that favors the formation of a "polar interphase". In contrast, over this very long time, both original volatile polar species and polar group resulting from the chemical degradation of the polymer network occurring on actual service conditions might be removed through diffusion mechanisms out of the material. This can result in a significant decrease in ϵ' . The opposite effects could counterbalance each other resulting in constant ϵ' values at 50°C.

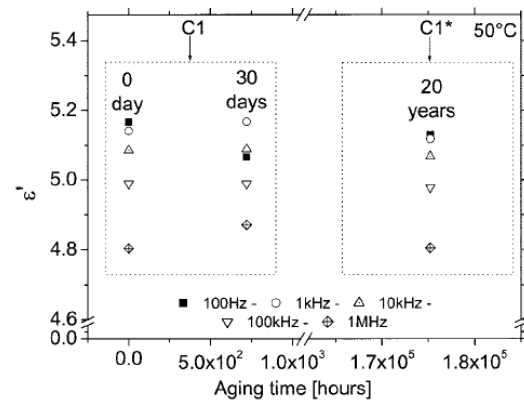


Figure 6.13 : Evolution of dielectric permittivity ϵ' (1st heating run) at 50°C and at several frequencies (ranging from 100Hz to 1MHz) vs. aging time for the unaged, aged for 30 days, and C1* samples. [Source: (169)]

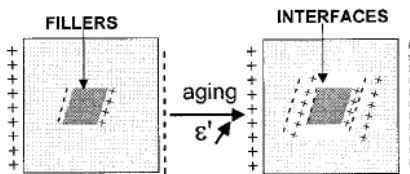


Figure 6.12 : Schematic representation of dipoles piling at the polymer/filler interface. [Source: (169)]

6.1.4 Conclusion

Microstructure and dielectric behavior changes undergone by an insulator based on epoxy reinforced by inorganic particles aged in actual service conditions over a long time, i.e. 20 years, have been investigated.

With respect to the characteristics displayed by the as received material based on the same composition, aging in service conditions results in the followings effects:

(i) a chemical degradation of the polymer network characterized by a shift of T_g towards the lower temperature. Such a chemical degradation gives rise to additional movable polar species whose presence are detected from dielectric measurements performed at high temperature, *i.e.* $T \geq 230^\circ\text{C}$. As a matter of fact, the shift of the critical frequency towards the higher values exhibited by the aged sample can result from an increase in the number and / or in motion ability of polar species. Such a critical frequency can constitute a probe of the chemical degradation of the polymer occurring over time in service conditions.

(ii) a structural recovery characterized by the presence of an endothermic peak near T_g on the thermograms.

(iii) a tendency to the particle debonding from the polymer matrix that could originate from both the chemical degradation and the physical aging.

(iv) no apparent change in the permittivity value measured at 50°C . However, it was expected an increase in ϵ' value because of the chemical degradation of the polymer that gives rise to polar species.

In order to identify the mechanisms leading to this unexpected result and in a more global way to evaluate the contribution of the structural recovery only on the composite properties, laboratory physical aging tests were carried out on two epoxy-based composites. First, the aging kinetics study points out that enthalpy excess (and T_g) is found to be a non-linear increasing function of the aging time. This is in agreement with Kovacs⁽¹⁶²⁾ and Bauwens⁽¹⁷¹⁾ data. Then, from SEM observations of fracture surfaces performed on aged samples, it was found that composites exhibit a tendency to particle debonding from the polymer matrix. Such a phenomenon could be related to the matrix densification due to the structural recovery and resulting in stress concentration at the polymer / filler interface.

Analysis of the dielectric behavior of aged materials showed that ϵ' measured at 50°C and at various frequencies increases with increasing aging time up to 73 days. This was related to (i) an increase in the relative volume ratio of dipoles because of the decrease in the polymer volume due to the structural recovery and / or (ii) the piling up of the original polar species at the matrix / filler interface that could be favored by the low adhesion quality between the polymer and the inorganic particles.

Permittivity value at 50°C displayed by the longest aged sample, *i.e.* aged for 6 months, was slightly but

significantly lower than that of measured for the 73 days aged sample. Such a decrease in ϵ' at 50°C for very long aging times could result from additional effect due to the removal through a diffusion process of volatile polar groups favored by long aging periods.

Accordingly, the mechanisms leading to apparently no changes in permittivity values measured at 50°C ($T < T_g$) exhibited by the 20 years aged insulator at various frequencies (Fig. 6.13) could result from the superimposition of the two following opposite effects,

(i) the first one is related to an increase in the relative volume ratio of dipoles due to the structural recovery and / or the piling up of the polar species at the polymer / particle interface

(ii) the second one acting in an opposite effect could be related to the removal of polar species, *i.e.* original polar molecules and / or additional polar species due to the chemical degradation occurring as the insulator underwent multistresses over a long time. This leads to a decrease that could counterbalance the ϵ' increase and result in a constant value of permittivity at 50°C .

6.2 Consequences on high voltage properties

From the previous section, a series of samples were chosen to characterize the influence of the aging process on the breakdown properties. The two samplings consisted of $C1$ and $C2$ composites aged in the laboratory Fig. 6.14a and 6.14b. Besides these samples, the $C1^*$ material that exhibited both chemical degradation and physical relaxation was also selected for this study.

Breakdown voltage measurements & SEM Characterization

The tests were performed at the ambient (20°C) under ac voltage supplied by a 50 kV, 50 Hz transformer. The breakdown voltages were determined as the average of four tests carried out in contact mode in ramp test. The specimen was immersed in silicon oil to prevent the surface discharges and flashovers.

The sample preparation and measurement technique to obtain the breakdown voltage were described above [LIEN].

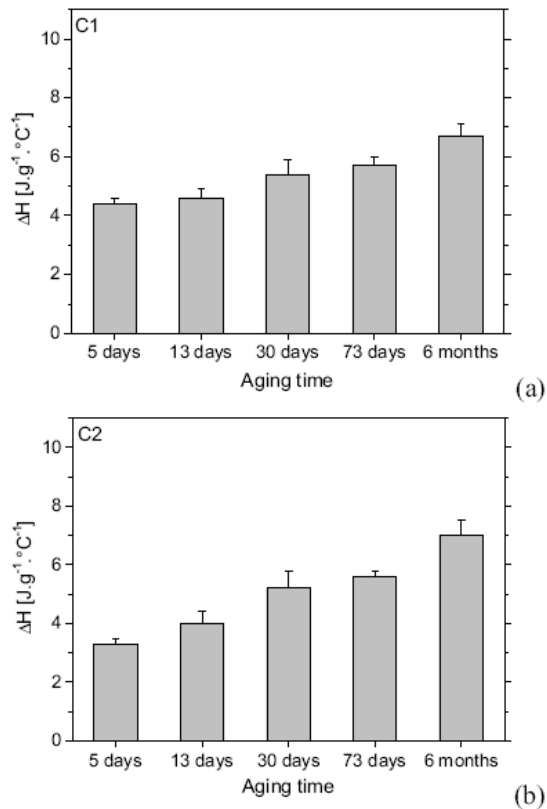


Figure 6.14 : Characterization of the structural relaxation of the epoxy through DSC: enthalpy excess ΔH as a function of aging time for the composites *C1* (a) and *C2* (b). [Source: (172)]

Observation of the breakdown tree paths were performed with a scanning electron microscope Stereoscan 440 LEICA. To obtain a good visualization of the treeing, a specific technique was performed which was described above.

6.2.1 Results and Discussion

The electrical breakdown field of the materials aged 20 years in service was first evaluated to quantify the influence of the global structural changes due to physical and chemical aging.

6.2.1.1 Effects of aging in actual service conditions on the electrical breakdown

Fig.6.15 shows a comparison of the field required for breakdown on as received composites (*C1*) and the aged counterpart (*C1**). As expected the 20 years old material exhibited a significant decrease in the electrical breakdown field both in quasi homogeneous and divergent fields. This decrease was however remarkably low (about 10%) taking into account the chemical degradations and structural modifications caused by 20 years aging in actual service conditions.

Here again appeared the need to separate to separate the relative contribution of the chemical modifications from that of the physical aging, on the dielectric breakdown. Much like the former section the study started by analyzing the influence of the sole physical aging.

6.2.1.2 The effects of physical aging on the electric breakdown

Fig. 6.16 and Fig. 6.17 show the evolution of the electric field required for the breakdown of the composites *C1* and *C2* as a function of enthalpy excess relative to laboratory aging time ranging from 5 days to 6 months. It was first noticed that the breakdown field monotonically increased with enthalpy excess (ΔH) both in divergent and quasi homogeneous configurations. Its variations obeyed an s shaped curve with ΔH (as with the aging time, not shown). All the plots could indeed be divided into three zones: (i) initially the breakdown field seemed to not depend on the structural aging of the matrix, (ii) for an enthalpy excess ranging from 3.5 and 6 $J.g^{-1}.^{\circ}C^{-1}$ the field to breakdown improved largely with a relatively

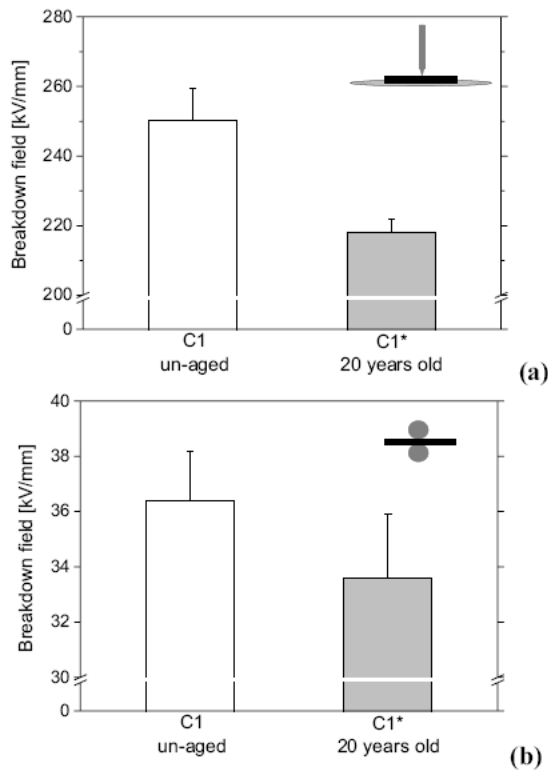


Figure 6.15 : Comparative breakdown field for $C1$ and $C1^*$ under divergent (a) and quasi-homogeneous (b) fields. [Source: (172)]

low variation of ΔH and (iii) for the highest ΔH (or aging times) a level off was evidenced.

This behaviour was observed for both $C1$ and $C2$ in both divergent and quasi homogeneous field configurations. Qualitatively, this set of experiments showed that the matrix densification led to a non linear improvement of the electrical properties under high electric field. In agreement with Champion and Dodd⁽⁹⁶⁾, it can be proposed that the densification of the matrix changes the trap site depth and density. This mechanism can thus alter the high field conduction process, impedes the tree growth and thereby improve the breakdown field.

For comparison, the fields to breakdown were normalized to their initial values (*i.e.* for $\Delta H \approx 0$) and represented in Fig. 6.18. The analysis of the data revealed:

1. two separate sets of data depending on the electrode geometry. The electric field configuration seemed thus to be the pertinent parameter separating small (quasi homogeneous field) and large (divergent field) sensitivity to physical aging.

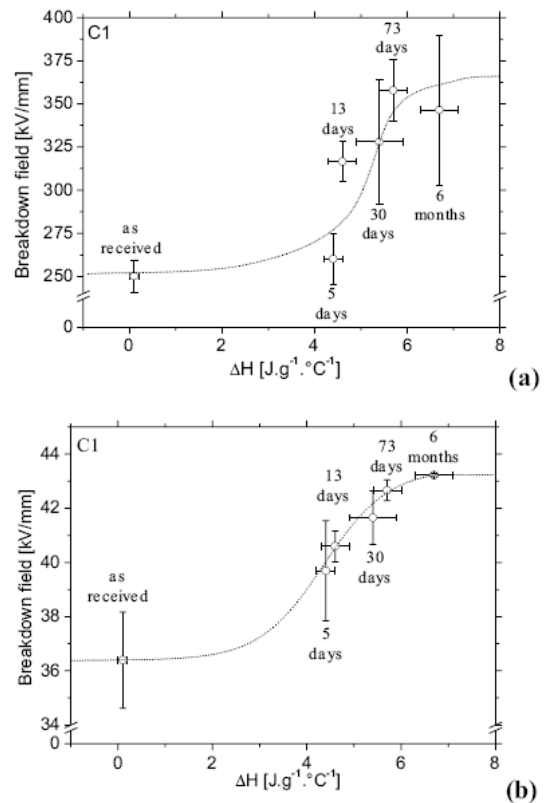


Figure 6.16 : Electrical breakdown field as a function of enthalpy excess under divergent (a) and quasi homogeneous (b) field for the composite $C1$. [Source: (172)] .

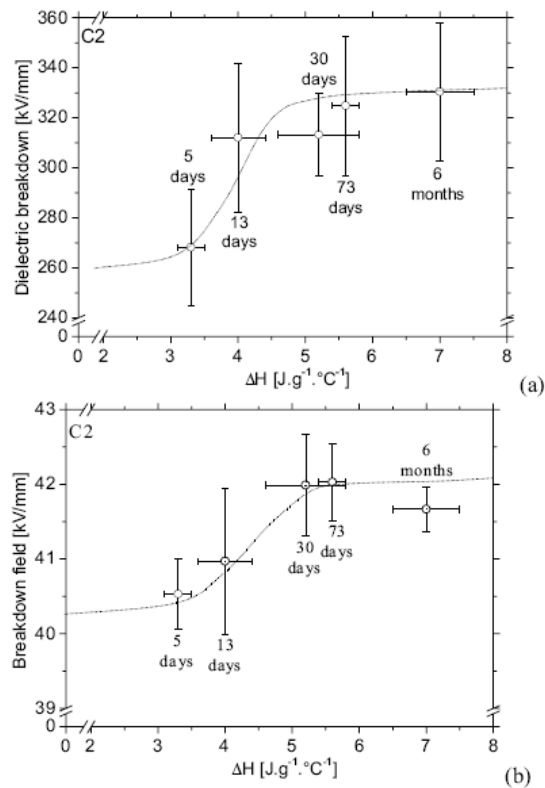


Figure 6.17 : Electrical breakdown field as a function of enthalpy excess under divergent (a) and quasi homogeneous (b) field for the composite C2. [Source: (172)]

- the two formulations exhibited rather minor differences, C1 was however overall more sensitive to the increase in ΔH than C2.

In order to understand these results, SEM observations were carried out on the fracture surfaces after breakdown under divergent and quasi homogeneous fields. Fig. 6.19 shows that under divergent field, the degradation was characterized by the formation of step arise trees, which were less than $3\mu m$ in length^(111;112). In contrast, under quasi homogeneous field, the electric field seemed to finally cause the formation of a $400\mu m$ in diameter crater without any remaining tree. These observations clearly revealed two distinct degradation mechanisms depending on the electrode geometry.

Based on the SEM observations, the differences in breakdown field vs. ΔH (or aging time) revealed by the materials between the two electrode arrangements can be interpreted as follow:

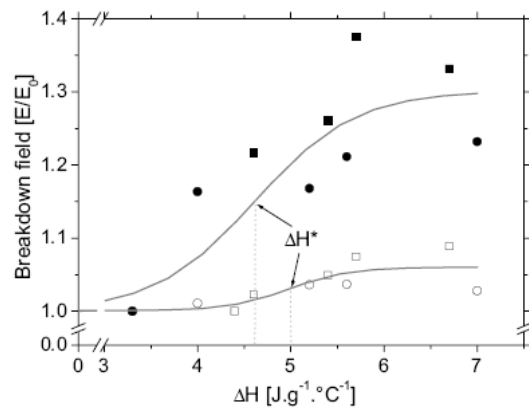


Figure 6.18 : Normalized breakdown field as a function of enthalpy excess under divergent field for the composite C1 (■) and C2 (●) and under quasi homogeneous field for the composite C1 (□) and C2 (○). [Source: (172)]

Under quasi homogeneous field, a global and broad breakdown cavity was observed. In this configuration the initial electrical field is macroscopically evenly distributed. The damage process could thus start with the help of the major flaws anywhere within the whole structure. Being the biggest heterogeneity, the filler is obviously expected to be the main origin for the field gradients. In particular, the biggest particles, those aligned to the electric field or with asperities primarily enhance the electric field close to their surfaces and the surrounding matrix can hence be defined as the “weakest link” in the composite. The presence of

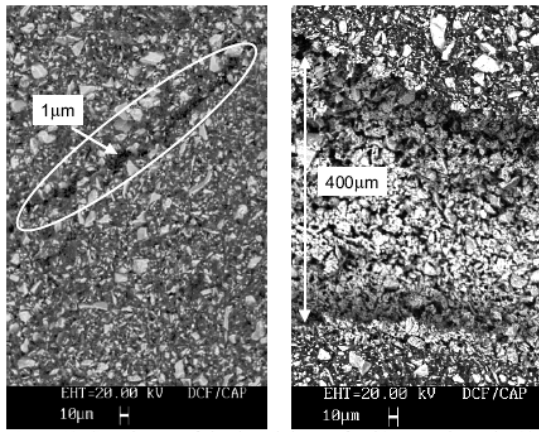


Figure 6.19 : SEM images of the degraded areas for $C2$ composite under (a) divergent field and (b) quasi-homogeneous field. [Source: (172)]

the particle is furthermore not altered by the structural modifications within the matrix. As a result, improving the properties of the polymeric host does not significantly change the main reason for breakdown.

In few words, under quasi homogeneous field, the global nature of the electric field causes a high sensitivity to major flaws anywhere in the composite and the very local matrix densification only results in a small increase in the breakdown field.

Under divergent field the damage took the form of a filamentary like structure. Because of the large field enhancement associated to the tip electrode, the tree naturally starts in the vicinity of the tip electrode. The final tree structures showed that the field remained localized during the whole damage process and eventually lead to quasi one-dimensional trees. This strongly cumulative process, spatially limited, prevented major flaws away from the trees controlling their development. The matrix densification could thus influence the tree propagation.

In summary, under divergent field, the local nature of the field causes a low sensitivity to major flaws in the composite and the breakdown field is more sensitive to the matrix improvement.

6.2.1.3 Results overview

As already noticed, the breakdown field of $C1^*$ was only slightly lower (10%) than that of the as received $C1$. It was however up to 40% lower than that of the $C1$ samples aged in laboratory, Fig. 6.20.

This result indicates that two opposite effects might alter the dielectric breakdown of $C1^*$. On the one hand the dielectric breakdown is expected to strongly increase because of the structural recovery. On the other hand, the multiple stresses in actual conditions lead to chemical degradations. The subsequent formation of polar groups and free radical could be induced under electric field:

- (i) a conduction current leading to overheating of the insulator by Joule effect that facilitates the dielectric breakdown by thermal effect
- (ii) an increase in the amount of ionizing collisions generating a mechanism of electric breakdown by avalanche.

Both phenomena result in a significant decrease in breakdown field. It is thus proposed that the above mentioned opposite effects counterbalance each other, resulting in a low decrease of field associated with dielectric breakdown after a 20 years aging in actual service conditions with respect to as received materials ($t = 0$).

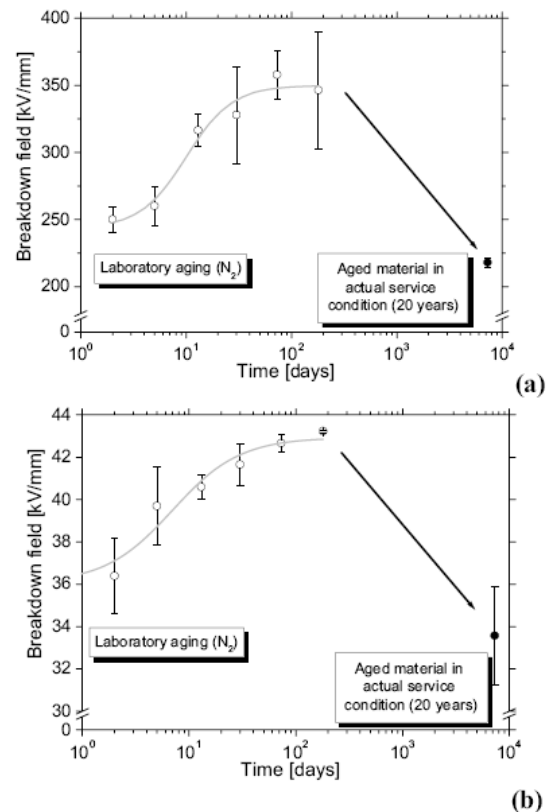


Figure 6.20 : Electrical breakdown field as a function of aging time under divergent (a) and quasi homogeneous (b) field for the composites $C1$ (\circ) and $C1^*$ (\bullet). [Source: (172)]

	Tip/Plane (DF)	Sphere/Sphere (QHF)
Amplitude (%)	30	6
ΔH^* (J.g ⁻¹ .°C ⁻¹)	4.6	5.0
Width (J.g ⁻¹ .°C ⁻¹)	0.54	0.32

Table 6.2 : Characteristics of the s-shaped curves in Fig. 6.18. The data was fitted to the Boltzmann function with the help of Origin® version 7.0 from OriginLab Corporation. Comparison of the results obtained in divergent (DF) and quasi-homogeneous (QHF) fields. [Source:(172)]

6.2.1.4 Relative influence of chemical and physical aging

It is finally striking that the decrease in field to breakdown after 20 years of real service conditions does not appear to depend on the nature of the electrical field, Fig. 6.20. The relative drop was indeed close to 10% both under divergent and quasi homogeneous fields for $C1^*$ when compared to the unaged $C1$. These two results apparently matched for very different reasons that do depend on the electrode configuration. A rough calculation was performed to investigate this interpretation, Table 6.3. This analysis was performed using the experimental measurement describing the individual sensitivity of the field to breakdown to (i) physical aging and (ii) degree of conversion, Fig. 5.15, page 70. In a first approximation, the chemical and physical influences were assumed to be independent.

- In the point plane configuration, the breakdown field strongly increases with the enthalpy excess. The polymer network also presents, for the same reason, a high sensitivity to chemical degradations of the organic matrix (109). Two strong effects thus oppose each other: a strong increase related to the physical aging and a strong decrease imparted by chemical degradations.

- In contrast, under quasi homogenous field, the dielectric strength is not much affected by either the physical aging or chemical degradation (109). Two effects, but with low amplitude thus oppose each other, basically leading to the same result as that of the divergent field configuration.

The absolute values of the field to breakdown measured and calculated assuming independent contributions thus qualitatively confirmed the influence of the electrode configuration. Only for the tip plane configuration was the calculation not very satisfactory. This difference between calculated and measured data for the divergent field could be due to some degree of interdependence between the physical and chemical phenomena. It is however important to note that the

sensitivity to chemical variation was only measured experimentally for a narrow range of extent of cure, α varying from 0.95 to 0.99 (109). On this range of α a linear relationship was established between the field to breakdown and the extent of cure, thus obtaining a constant sensitivity. For the present calculation, it was assumed that the linear dependence could be extrapolated down to $\alpha = 0.88$. This assumption should be first verified to conclude whether an interdependence between the chemical and physical structural changes alter the field to breakdown.

(1) Experimental field breakdown of $C1$ "as received" ($\alpha \approx 1$ and $\Delta H \approx 0$ J.g⁻¹.°C⁻¹)

Calculated field to breakdown with only chemical degradation

Hypothesis: For this calculation (corresponding to **I** in the Table 6.3) ΔH was assumed to be zero (no physical aging).

(2) α was approximated from the Tg of $C1^*$ using the Di Benedetto equation. This α value takes into consideration the chemical degradations of the $C1^*$ matrix(140)

(3) Field to breakdown of $C1^*$ ($\alpha \approx 0.88$ and $\Delta H \approx 0$ J.g⁻¹.°C⁻¹) calculated from the sensitivity of dielectric breakdown field to α (109)

Calculated field to breakdown with only physical aging

Hypothesis: For this calculation (corresponding to **II** in the Table 6.3) α was assumed to be one (no chemical degradation).

(4) Enthalpy excess associated with the physical aging of the composite $C1^*$ after 20 years in industrial aging(169)

(5) Field breakdown of $C1^*$ ($\alpha \approx 1$ and $\Delta H \approx 5.2$ J.g⁻¹.°C⁻¹) calculated with the curves of dielectric breakdown field versus ΔH (Fig. 6.16.a and Fig. 6.16.b).This curve was used as an abacus.

				Quasi Homogen.	Divergent
C1	(1)	Experimental field to breakdown fo C1 "as recieved" (kV/mm)		36	250
C1*	I Chemical Effect	(2)	α conversion degree	0.88	
		(3)	Field to breakdown (kV/mm)	29	130
	II Physical Effect	(4)	ΔH (J/g/oC)	5.2	
		(5)	Field to breakdown (kV/mm)	42	320
	III Chemical & Physical Effects	(6)	Calculated field to breakdown (kV/mm)	35	190
		(7)	Calculated field to breakdown (kV/mm)	34	170
		(8)	Experimental field to breakdown	34	220

Table 6.3 : Overview of the breakdown results: relative influence of the chemical and physical agings ; comparison between experimental data and numerical guesses [Source: (172)] .

Calculated field to breakdown with both chemical degradation and physical aging

Hypothesis: For these calculations (corresponding to *III* in the Table6.3) the influence of chemical and physical changes were assumed to be independent.

(6) and (7) Fields to breakdown of $C1^*$ ($\alpha \approx 0.88$ and $\Delta H \approx 5.2 \text{ J.g}^{-1}.\text{°C}^{-1}$) calculated using respectively:

$$E(\alpha, \Delta H) = E(\Delta H) + \frac{\partial E}{\partial \alpha} \times \Delta \alpha \quad (6)$$

$$E(\alpha, \Delta H) = E(\Delta H) \times \frac{E(\alpha)}{E(\alpha = 1)} \quad (7)$$

(8) Experimental field breakdown of $C1^*$ ($\alpha \approx 0.88$ and $\Delta H \approx 5.2 \text{ J.g}^{-1}.\text{°C}^{-1}$).

6.2.2 Conclusion

During 20 years in actual service conditions $C1^*$, an insulator based on epoxy reinforced by inorganic particles, underwent strong changes in its microstructure. DSC measurements indeed pointed out (i) a chemical degradation of the polymer network characterized by

a shift of T_g towards lower temperatures and (ii) a structural recovery that was detected by the presence of an endothermic peak, characteristic of the so called physical aging. Considering these modifications, a large decrease in breakdown field was expected. A 10% decrease in breakdown field was however measured with respect to the as received sample, both in quasi homogeneous and divergent fields. In order to identify the mechanisms leading to this surprising relative stability and to evaluate separately the contribution of the structural recovery on the composite properties, laboratory physical aging tests were carried out in a controlled atmosphere (nitrogen). The laboratory aged materials showed that breakdown field actually increased with increasing enthalpy excess (associated with the structural aging). This phenomenon was attributed to the densification of the matrix which impedes tree growth by the reduction of the free volume. These results indicate that two opposite effects alter the dielectric breakdown of $C1^*$ (i) the structural recovery which largely opposes dielectric breakdown and (ii) the multiple stresses in actual conditions which lead to chemical degradations and thereby lowers the field to breakdown. Both effects almost counterbalance each other after 20 years aging in actual service conditions.

It was also observed that the choice of the electrode geometry greatly altered the dielectric breakdown of these composites. It is proposed also here that in a quasi homogeneous field configuration the breakdown is mainly governed by the major flaws at the sample scale, namely the reinforcing particles. In other words, measurements performed for instance in a sphere sphere configuration are not very sensitive to variations within the polymeric matrix. On the contrary, under divergent field, the field initially enhanced on the tip electrode remains localized at the tip of the growing tree during the whole breakdown process. As a result, the major flaws might not be reachable by the damage tree and an improvement in the matrix properties induces a strong increase of breakdown field. The influence of the electrode arrangement was confirmed by a semi quantitative analysis based on the hypothesis that the chemical and physical modifications acted independently.

Projects...

Chapter 7

Research projects

⊙ **Introduction** ⊙

My research projects are directly related to the activities described in this report: the multi-scale/properties relationships in heterogeneous systems, with a focus on damage and aging. These projects also remain in strong interaction with industrial partners and fit into the scientific activity at LMOPS. It may be useful to note that these research projects are not virtual ones, but actually describe the main tasks in progress at the laboratory and in which I am involved. The description may seem a bit elusive to the people working on the projects, especially to the PhD candidates. This was done on purpose. The approach is described here, but the actual detailed results will be part of their degrees and is not to be disclosed before publication or graduation.

Contents

7.1	Aging of fuel cells	100
7.2	Modeling of the mechanical properties	101
7.3	New characterization device for electrical and mechanical properties	101
7.4	Energy density	102

7.1 Aging of fuel cells

This project is conducted in collaboration with Axane-Air Liquide, Ecole des Mines de Paris, 3M, A2E Technologies, and Bouygues Telecom. In the LMOPS there are four researcher involved (besides me): Profs N.D. Alb erola and C. Bas, Dr. J. Bernard (Post Doc fellow) and PhD candidate A.S. Dan erol.

Aging and degradation of the membrane electrode assembly (MEA) are the main issues that prevent the development of fuel cells on a large scale. There is a high demand for fuel cells, and a large amount of research is being carried out world wide. However, current MEAs are unable to meet the targeted lifetimes (roughly 10 000 h in continuous service). In addition, the durability of the core of the fuel cell is further reduced under “real world” conditions *i.e.* rapid load changes, cold-start, start-stop cycles, and variations in temperature, current density and relative humidity)

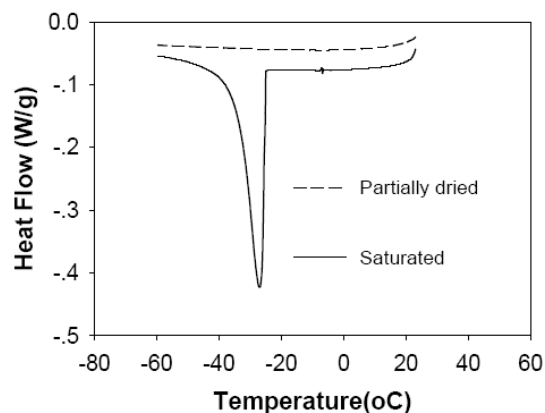


Figure 7.1 : DSC scans of water-saturated and partially dried (dried in ambient environment for about 30 minutes) Nafion 117; scan rate, $10^{\circ}\text{C}\cdot\text{min}^{-1}$

The challenge with this type of material is thus similar in nature to the work described in chapter 6 (page 77) of the current report. Unfortunately the microstructural changes induced by “accelerated aging” techniques seem to not correlate properly with on site aging. For this reason a much broader, approach was considered for this project.

At first, a systematic study will be undertaken on numerous fuel cells used in service and after various aging times and environmental conditions. The series

of results will then be compared with those obtained on cells aged in controlled conditions in the lab. The purpose of the accelerated aging procedures is, here again, to identify conditions where only one particular degradation or failure mode is activated, or in other words to separate as much as possible the contributions from the different aging parameters.

A difficult issue in this project is to identify “aging markers” that vary monotonically over time and relate to the expected property, *i.e.* the production of electric energy from Hydrogen and Oxygen. This step, of structural marker identification has started a year ago. The approach consists of characterizing the MAE after failures (that can therefore be considered as extremely “old”) in real conditions and running the characterizations described as relevant in the literature. A large series of physicochemical tests is hence currently being performed on the polymer to quantify the degradation, namely (i) Proton conductivity, and OCV electrochemical characterizations (ii) DSC, gas permeation, and WAXS, physicochemical characterizations and (iii) IR, and TGA to quantify the chemical stability. An example of expected results was extracted from the literature⁽¹⁷³⁾ and is presented in Fig. 7.1, it qualitatively shows how the DSC can be used to probe the amount of water in the polymeric membrane. In addition to these conventional techniques to characterize the MEA, a close attention is being paid to the electrode-membrane interface that is studied with mechanical, electrical and morphological analysis.

From the application point of view, three major outcomes will be delivered to industrial partner within two years. First, a way to “calibrate” the aging times between laboratory and on-site aging, this may involve many parameters concerning the actual history of the samples aged in service. Second, a reliable way to follow the actual aging of the MEA on active cells. The first results indicate that this could probably even

be performed *in situ*, while the cell is running and without taking the cells out of the stacks. Third, a fast and efficient way to improve the MEA with the help of both the structural parameters leading to failure, or in other words, to grade the core cells.

7.2 Modeling of the mechanical properties

This project is essentially carried out in the LMOPS with Prof P. Mélé and PhD candidate J.C. Honoré.

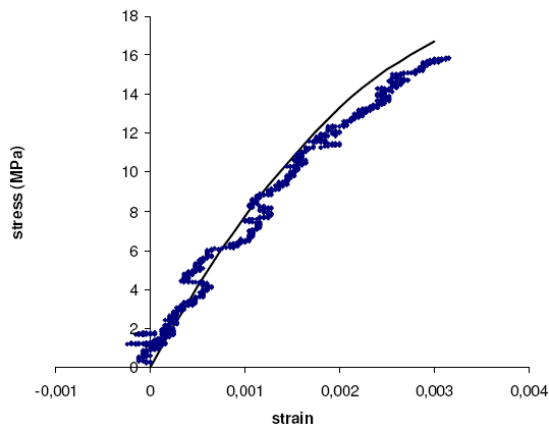


Figure 7.2 : Comparison of stress strain curves determined experimental (dots) and simulated with the finite element analysis applied to images (line), case of a unidirectional composite reinforced with 50 vol% of glass fibers.

This project is directly related to chapters 1 and 4 of the present report (pages 11 and , 47 respectively). The goal here is to better understand the relationships between the meso structure and mechanical properties

of polymer based composites. The approach is similar to that of chapter 4 and involves “meshing images” in order to run finite elements analysis. In the case of mechanical properties, the study started with unidirectional fillers in the transverse to avoid problems related to the 3D nature of the mechanical stresses. This study is also developed with a strong experimental aspect that involves characterization of the distribution in mechanical strain with local measurements and image correlation. This study is now somewhat mature and an example of the results is presented in Fig. 7.2. The macroscopic behavior of the composite is well understood with the help of the simulation with requires only one parameter that describes the damage of the polymer. In return the simulation showed that the damage started in the very early stage of the stress strain curve (few per thousands) because of the extreme stress and strain enhancement induced by the fillers. This observation is also in agreement with the very brittle behavior observed with these composites in the transverse direction.

7.3 New characterization device for electrical and mechanical properties

This project is essentially carried out in the LMOPS with Prof P. Mélé and PhD candidate T. Fathallah. The project also benefits from a collaboration with 01-dB Metravib represented by B. Duperray

The macroscopic behavior of composite materials is controlled by the intrinsic properties of the constituents and the arrangement of the phases on various scales. As described in this report, measurements of physical and physicochemical properties of heterogeneous systems may furnish informations far beyond the very popular percolation threshold. It was

also shown in chapter 2 that simultaneous measurements of electrical and mechanical properties could be brought much further.

The dynamic mechanical properties (called either *DMA* or *DMTA*) is a very common way of investigating the microstructure of polymers and composites. It is especially fruitful because of the $\tan(\delta)$ parameter

that is very sensitive to changes in molecular mobility. $\tan(\delta)$ is also appreciated because it does not depend on the sample's geometry. Surprisingly *in situ* measurements of electrical properties on a sample submitted to a periodic mechanical solicitation has rarely (if ever) been reported in the literature.

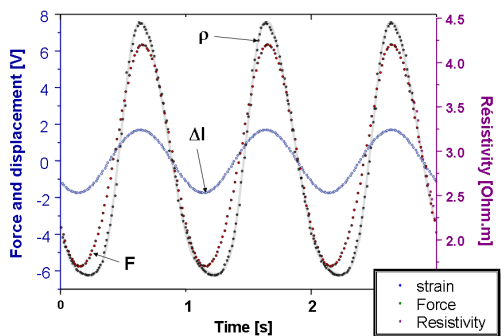


Figure 7.3 : Simultaneous measurement of the mechanical and electrical properties during low amplitude mechanical solicitations (the measurements were performed on a conducting vulcanized elastomer)

The goal of this project is to develop a characterization apparatus that will actually “probe” the structure of the composite at two different scales: the mechan-

ical properties will give information on the molecular dynamics of the polymer whereas the electrical properties will probe the mesostructure, at the fillers scale. A functioning prototype has been working in LMOPS for several months, and a simple example of the results is provided in Fig. 7.3. On this graph, one can observe that the electrical properties follow, much like the force and deformation a sine curve, with its own amplitude and $\tan(\delta)$. As a result a new $\tan(\delta)$ parameter was brought up, that was named $\tan(\delta_{em})$, where the “e” and “m” obviously stand for electrical and mechanical properties, respectively. This parameter does not seem to directly be related to the common $\tan(\delta_m)$. In addition, the data obtain with a rather simple vulcanized elastomer filled above the percolation threshold with common carbon black, show that other parameters are yet to be defined in order to properly describe these experiments. An extension to ac measurements is also scheduled for the near future.

The apparatus will obviously be very useful to investigate the structure-property relationships of polymer filled with conducting filler, it will also provide the users with a way to follow *in situ* geometric changes on samples submitted, for instance to temperature changes (stretched polymers). In addition, it is envisaged to utilize this device for many other applications like artificial muscles, piezzo electric material, and crystal liquid polymer to name but few.

7.4 Energy density

This project is mainly carried out in the CLIPS center of Case Western Reserve University (Cleveland, OH) with Profs A. Hiltner and E. Baer, and M. Mackey (PhD candidate). In addition, the project involves a collaboration with Dr M. Wolak and J. Shirk from the Naval Research Laboratory (Washington, DC).

Energy production and storage are becoming a growing problem in modern society. One efficient way of storing energy is the use of capacitors. These devices are commonly employed in the electronics industry for filtering or low energy storage applications. Their use in large storage applications is, however, very limited due to low energy density, which causes their size and weight to be unacceptably high. In spite of this, the demand for larger storage capacitors is increasing. One broad area, in particular, for implementation is battery replacement. The benefits

include extremely fast charge and discharge rates as well as more efficient energy use.

The performance of a capacitor is primarily governed by the core material: an electrical insulator referred to as a dielectric. The dielectric materials commonly employed nowadays rely on old technologies; they are principally made out of paper, ceramics, and common polymers. Polymeric dielectric cores have several good qualities compared to the more conventional materials. These include high efficiency, good mechanical properties, high stability/reliability, and

ease of processing. The major shortcoming, however, is its low energy density compared to many other types of capacitors (and virtually all batteries) making large storage impractical for high energy applications. The current value of ceramic, paper, and polymeric capacitors ranges from 0.1 to 10 J.cm³.

From a material standpoint, the energy density can be increased only by increasing two intrinsic properties of the dielectric: the permittivity and breakdown strength. The quantitative relation is $E=0.5.\epsilon_r.E_B^2$ where ϵ_r is the permittivity and E_B is the breakdown strength. Polymeric capacitors have a low energy density because there is no polymeric dielectric material that possesses both a high permittivity and high breakdown strength (Fig. 7; icons 1, 4, 5, and 8). Polypropylene and polycarbonate have very large breakdown strengths, but rather low permittivities. Polyvinylidene Difluoride (PVDF) on the other hand has a high permittivity but relatively low breakdown strength.

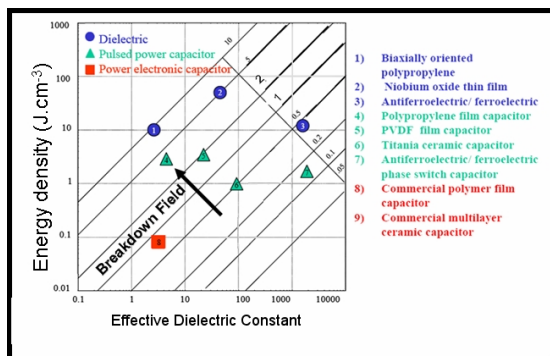


Figure 7.4 : Energy density of common dielectric materials⁽¹⁷⁴⁾

The approach to accomplishing the goal involves using microlayer coextrusion to produce a composite consisting of alternating layers of two polymers (one with a high permittivity and the other with a high breakdown strength). The composite is expected to have much better electrical properties than either of the components themselves. In addition to microlayering, improvements can be made by adding high permittivity fillers and stretching the film (orienting the polymer chains).

Microlayering puts a large amount of interface⁽¹⁷⁵⁾ into the composite, which is known to potentially increase the permittivity. This interface effect (called the Maxwell-Wagner-Sillar effect) is not fully understood, but is one benefit of the microlayering process

for this project. In regards to breakdown of microlayered films, it is uncertain where the composite's value will lie in relation to the pure components. However, a composite film consisting of two layers of the same material will have a higher breakdown than a single film of the same thickness. This has been shown to be particularly significant in the case of the two materials having a wide variation in breakdown strength. In addition, preliminary breakdown measurements on a PS-PMMA microlayered system have shown very promising results. More specifically, the breakdown of the PS-PMMA film seemed 1.5 times higher than that of PS and PMMA. Although the preliminary results have to be confirmed, they do show that a synergetic effect could be achieved through microlayering. We speculate that the breakdown strength is related to the sharpness of the interface (amount of interphase; Fig. 7.5), but more work in this area is necessary before any solid conclusions can be made.

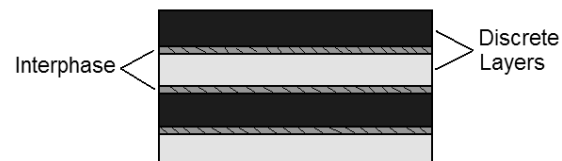


Figure 7.5 : Schematic of a 4-layer film showing the layers and interphase.

In addition, processing modification are envisaged. The first one involves blending high permittivity filler particles with either polymer prior to processing via microlayer coextrusion. Several prospective filler particles include alumina, Barium Strontium Titanate (BST), and silica. Besides the obvious increase in permittivity, the fillers may cause a barrier affect which enables one to safely operate at electric fields that are closer to the breakdown strength⁽¹⁰⁹⁾, see page 47.

The second processing variable is increasing the polymer chain alignment by stretching. Chain alignment increases the breakdown of polypropylene⁽¹⁷⁶⁾ and we speculate that a similar effect will occur in other polymers. Also, PVDF exhibits an enhanced permittivity when stretched

Future work includes microlayering a set of (PC)/PVDF films and measuring the permittivity and breakdown as a function of the number of layers (or layer thickness) and composition (ratio of the two components). In addition, the samples will be examined after breakdown to find structural evidence (besides the actual measured breakdown strength) for

the interface effect on the dielectric breakdown. The effect of bi-axially stretching these films will also be studied.

In order to optimize the capacitive energy density, some understanding of the structure-electrical properties will also have to be developed. Thus, the project includes a detailed analysis of the forced assembly structures, namely: morphological characterization through AFM and SEM and structural characterization, mainly through DSC.

Lists & references

List of Figures

1	The “multi-scale approach”: definition of the main three scales utilized in the manuscript: 1- macroscopic scale, essentially that of the final product, 2- mesoscopic scale, corresponding to the size of the <i>biggest heterogeneities</i> i.e. the fillers in the present case, and 3- microscopic scale, that of chemical interactions. This figure was developed with Prof. Patrice Mélé for the Master’s lectures . This was largely inspired by Fig. 9 in publication (1)	2
2	The three basic connectivity states on a network as a function of the number of active bonds.	5
3	Collection of critical exponent values t and corresponding critical threshold concentration x_c for various disordered conductor-insulator composites. The dashed line denotes the universal value $t \approx 2.0$, from Vionnet-Menot <i>et al.</i> ⁽¹³⁾	6
4	Summarized representation of the percolation process. The geometrical and physical quantities are presented on linear arbitrary scales.	6
5	dc electrical conductivity as a function of filler content (case of spherical filler) and comparison with percolation theory [Source: (21)]	7
6	Sensibility of the percolation threshold on the determination of the critical exponent. Slightly varying V_c , t varied from 1.76 ± 0.02 to $2 \pm 2 \times 10^{-10}$ to 2.18 ± 0.02 . Note that the quality of the fit is not much affected by the changes in V_c	7
7	Simple geometrical explanation for the divergence of the permittivity observed close but below the percolation threshold	8
8	The percolation threshold does not depend on the size of the box, however increasing the size of the system reduces the error on the estimation of V_c	8
1.1	Numerical simulations on a square lattice of links. All sites are occupied by conducting grains. The links bold a distribution of resonant circuits, from Clerc <i>et al.</i> ⁽²⁶⁾	12
1.2	2D random tessellation with Voronoi polygons (1000 edges). This graph was obtained with a probability of active bounds p equal to 0.6. Black segments represent active bounds (resistors) and the gray links represent non-active bounds (capacitors). Schematic representation of the electrodes, the voltage source, and the current measurement resistor [Source: (39)]	13
1.3	Real (■) and imaginary (O) parts of the conductivity at 1 kHz vs. occupation probability for a 2D Voronoi tessellation [Source: (39)]	13
1.4	(a) Definition of the short fiber’s positions in the cube being modelled, and (b) example of microstructure with 500 elements. Periodic conditions were applied in the Y and Z direction and the conductivity was computed in the X direction. Fibers intersecting the boundary of the cube in the X direction were cut [Source: (39)]	14
1.5	(a) Determination of the equivalent capacitor value: dashed lines represent the assumed field lines, and (b) Schematic representation of the microstructure and equivalent RC circuit. The dashed lines represent the capacity and the solid lines represent the resistors [Source: (39)]	15
1.6	Calculated geometric parameters: correlation length ξ (●) and strength of the infinite network P (□) vs. the filler content [Source: (39)]	17
1.7	Real part of the conductivity (p) and relative permittivity (●) determined at 1 <i>kHz</i> vs. filler content (top) experimental, and (bottom) simulated data [Source: (39)]	18

1.8	Frequency dependence of the conductivity at room temperature for composites filled with 0 (.), 1.5 (+), 3 (-), 4.8 (▲), 7 (□), 12 (○), and 16vol.% (*): (left) experimental, and (right) simulated data [Source: (39)]	19
1.9	Frequency dependence of the phase angle at room temperature for composites filled with 0 (Û), 1.5 (+), 3 (-), 4.8 (▲), 7 (□), 12 (●), and 16vol.% (*): (left) experimental, and (right) simulated data [Source: (39)]	19
2.1	Structural model for ethylene-octene copolymer as a function of comonomer content, from Bensason <i>et al.</i> (54)	22
2.2	Scanning electron micrograph of a cryofracture surface showing dispersion of the carbon black filler (20% v/v) [Source: (65)]	23
2.3	Current-voltage relationship of EO with 20% (v/v) Carbon Fibre, 45% (v/v) Low Structure Carbon Black, and 20% (v/v) High Structure Carbon Black before (open symbols) and after (solid symbols) straining to 20% [Source: (64)]	24
2.4	Resistivity as a function of filler content. The solid lines are the statistical percolation fit from Eq. 2.3 [Source: (64)]	24
2.5	Mechanical properties of composites with various amounts of carbon black. The solid lines are fits to the sliplink model, Eq. 2.6, with the shift factor from Eq. 2.5 for $f = 4.83$ [Source: (65)]	25
2.6	Rubber modulus $G_c = \sigma \cdot (\lambda - 1/\lambda^2)^{-1}$ of composites with various amounts of carbon black. The moduli were vertically shifted (by a shift factor α_v) to the match that of unfilled EO. [Source: (65)]	25
2.7	Comparison of the experimental shift factors with the Guth models for spherical particles (dotted line, Eq. 2.4) and rodlike particles (solid line. Eq. 2.5) [Source: (65)]	26
2.9	Definition of the four regimes in the resistivity-strain relationship. Case of EO filled with 20%(v/v) carbon black [Source: (65)]	27
2.8	Influence of carbon black content on the electrical properties under large strain. All carbon black contents are above the percolation threshold [Source: (65)]	27
2.10	Schematic representation of the proposed microstructural mechanisms for the changes in resistivity upon stretching [Source: (65)]	29
2.11	Schematic representation showing adsorption of a linear EO chain segment to the steplike edges of a carbon black particle, to produce good adhesion, adaptation from (74;75) [Source: (65)]	30
3.1	Potential energy of interaction between two charged particles [Source: (23)]	32
3.2	Frequency dependence of the conductivity for 0 (■), 0.012 (O), 0.03 (*), 0.06 (▼), 0.12 (□), 0.3 (▲), 0.48 (x), 0.6 (●), and 0.9 (◇) volume percent of carbon black with addition of $CuCl_2$ [Source: (23)]	34
3.3	Frequency dependence of the conductivity for 0 (■), 0.012 (O), 0.03 (*), 0.06 (▼), 0.12 (□), 0.3 (▲), 0.48 (x), 0.6 (●), and 0.9 (◇) volume percent of carbon black without addition of $CuCl_2$ [Source: (23)]	34
3.4	Real part of the conductivity at 1 kHz with (p) and without (u) addition of $CuCl_2$. dc electrical properties with (F) and without (E) addition of $CuCl_2$. Insets: comparison with power law dependence [Source: (23)]	35
3.5	Imaginary part of the conductivity at 1 kHz with (□)and without (●) ou (●) addition of $CuCl_2$. dc electrical properties with and without addition of $CuCl_2$. Insets: comparison with power law dependencies [Source: (23)]	35
3.6	Transmission optical micrographs of thin polished sections of cured material, (A1) 0.9%, (A2) 0.93%, and (A3) 0.96% without $CuCl_2$, and (B) 0.9% with $CuCl_2$ [Source: (23)]	36
3.7	Schematic representation of the experimental procedure	38
3.8	Transmission optical micrographs taken after 5, 12, and 40 <i>min</i> corresponding to the positions denoted by a , b , c [Source: (84)]	38

3.9	Electric current versus time for a CB content of 0.12% and an applied voltage of 30 V [Source: (84)]	38
3.10	Electrical resistivity for a CB content of 0.6% and applied voltages of 30 V (\square) and 60 V (\circ) [Source: (84)]	38
3.11	Electrical resistivity for a CB content of 0.6% and applied voltages of 30 V (\square) and 60 V (\circ). [Source: (84)]	39
3.12	Proposed mechanism of electrostatic charging of the CB particles (with acidic sites AH) by polymeric dispersants (with basic sites B), from Prasse <i>et al.</i> (85)	40
3.13	Degradation and breakdown mechanisms as a function of time and electric field(88).	44
4.1	Methodology utilized to determine the breakdown field [Source: (109)]	48
4.2	Potential distribution on a regular mesh before any breakdown occurred. The units are arbitrary on every axis.	49
4.3	Schematic representation of the macroscopic voltage (or local electric field) required to continue the breakdown propagation at each step of the simulation.	49
4.4	Distribution in current in the links during the breakdown process.	50
4.5	Influence of δi on the breakdown pattern (see text for details) [Source: (113)]	50
4.7	Elementary method for construction of equivalent network(118).	51
4.6	The steps of simulation of breakdown trees in heterogeneous materials (case of a composite in a homogeneous field). Photomicrograph 2D, segmented picture, equivalent network (the elements corresponding to the matrix have not been plotted to improve clarity) and dielectric breakdown simulation [Source: (109; 114)]	52
4.8	Example of possible meshing conditions: rough mesh mesh specific to the matrix “High quality” mesh, useful for breakdown simulation Interface refined mesh, suited for homogeneization purposes.	53
4.9	Initial field distribution, case of a two-phase composite with a ratio of ten in their intrinsic conductivities in a macroscopic homogeneous field, before any breakdown.(109)	54
4.10	Potential distribution after few breakdown steps, case similar similar to Fig. 4.9, bu in divergent field after 5 breakdown steps. [Source: (109)]	54
4.11	Interrelation between minimum particle distance and breakdown tree (plane - plane electrode arrangement).) [Source: (109)]	54
4.12	Example of semi local parameter: the smoothed amount of particle enhancing the electric field (curve on top) correlates to the weakest point in a composite revealed by 20 independent calculations.	54
5.1	Representation of the relative volume fraction as a function of the relative injection time (t_{rel}) for the 12 analyzed zones. from [Source: (140)]	60
5.2	Definition of the three independent parameters extracted from the thermogramms: T_g , ΔT_g , and ΔC_p . from [Source: (140)]	61
5.3	Histograms of populations of the three independent parameters: (a) T_g , (b) ΔT_g , and (c) ΔC_p (the experimental data are represented without accounting for the withdrawal position). from [Source: (140)]	62
5.4	T_g as a function of the relative injection time t_{rel} from [Source: (140)]	63
5.5	ΔT_g as a function of the relative injection time t_{rel} from [Source: (140)]	63
5.6	ΔC_p as a function of the relative injection time t_{rel} . [Source: (140)]	63
5.7	ΔT_g versus α for the C2 composites. [Source: (140)]	64
5.8	Schematic representation of T_g as a function of t_{rel} . from [Source: (140)]	64
5.9	Sampling of C2-composite with various conversion degrees (α) [Source: (109)]	66
5.10	Test specimens used to measure dielectric breakdown (a) point-plane electrodes and (b) spherical electrodes [Source: (109)]	66

5.11	Sample preparation for SEM treeing characterization [Source:(109)]	67
5.12	SEM picture of electrical tree in the composite under divergent field [Source:(109)]	68
5.13	SEM picture of electrical tree in the composite under quasi-homogenous field [Source:(109)]	69
5.14	Schematic representation of the proposed tree propagation in sphere-sphere (Global Weakest Link, left) and point-plane (Local Weakest Link, right) configurations [Source:(109)]	70
5.15	Dielectric Breakdown as a function of conversion degree under divergent (a) and quasi-uniform (b) fields [Source:(109)]	70
5.16	Dielectric Breakdown, measured in a point/plane configuration for both systems M2 and C2 (a) and schematic interpretation of the reinforcing influence (b) [Source:(109)]	71
5.17	Measured dielectric breakdown in sphere-sphere configuration for both systems M2 and C2 (a) and schematic interpretation of the influence of the filler (b) [Source:(109)]	72
5.19	Schematic representation of the method proposed to obtain various meshes from a single image: initial mesh obtained from the particle's geometry (left) and another mesh for the exact same particle (right). (The arrows are added to guide the eyes.) [Source:(109)]	73
5.20	Interrelation between minimum particle distance (light gray) and breakdown tree (dark gray) in a plane-plane electrode arrangement. [Source:(109)]	73
5.18	The steps of simulation of breakdown trees in heterogeneous materials (case of composite C2 in point-plane configuration).(a) SEM original Photomicrograph, (b) segmented picture, (c) equivalent network, (d) dielectric breakdown simulation (as continued after 50 steps), (e) dielectric breakdown simulation (as stopped after 325 stages) and (f) Weibull plot to obtain the field to breakdown [Source:(109)]	74
5.21	Dielectric breakdown field obtained from experiments (E) and simulation (S) for both systems M2 and C2 systems in both quasi-homogeneous and divergent fields. [Source:(109)]	75
6.1	Samples for aging times ranging from 9 hours to 6 months [Source:(169)]	79
6.2	Thermograms recorded for the as received material, C1 (second heating run), and for the 20-years-aged material, C1*,-first (solid lines) and second (dashed line) ramp of temperature [Source:(169)]	81
6.3	Real part of the dynamic mechanical modulus(E') vs. temperature shown by the C1 and C1* samples at 10Hz [Source:(169)]	82
6.4	SEM observations of fracture surface for as-received (a),and aged (b) composites [Source:(169)]	82
6.5	Dielectric permittivity ϵ' vs. temperature recorded for C1 (\blacksquare 1 st , and \square second heating ramp) and C1* (\bullet 1 st , and \circ 2 nd heating ramp) at 1kHz. [Source:(169)]	83
6.6	Dielectric permittivity ϵ' vs. frequency recorded for C1 (\blacksquare 1 st , and \square second heating ramp) and C1* (\bullet 1 st , and \circ 2 nd heating ramp) at 1kHz. [Source:(169)]	83
6.7	Thermograms of as-received systems (a) and composites aged under laboratory conditions for (b) 9h, (c) 20h, (d) 5days, (e) 13 days, (f) 30 days, (g) 73 days, (h) 6 months -1 st heating run for the composites C1 (α) and C2 (β) [Source:(169)]	84
6.8	Evolutions of Tg (a) and enthalpy excess ΔH (b) values as a function of aging time for the composites C1 (\blacktriangle) and C2 (\bullet). For comparison the values reported by Montserrat (100) on a similar formulation as C2 were added to the graph (+). [Source:(169)]	85
6.9	Plots of dielectric permittivity ϵ' (1 st heating run) vs. temperature at 320 Hz of the aged composite C1for (—)30 days, (- - -) 73 days and (. . .) 6 months. [Source:(169)]	86
6.10	Evolution of dielectric permittivity ϵ' (1 st heating run) vs. aging time for the sample C1 unaged and aged for 30 days, 73 days 6 months, at 50°C and at several frequencies (ranging from 100Hz to 1MHz). [Source:(169)]	86
6.11	Evolution of the dielectric permittivity ϵ' (1 st heating run) vs. aging time for the sample C2 un-aged, aged 30 days, 73 days 6 months at 50°C and at several frequencies (ranging from 100Hz to 1MHz). [Source:(169)]	87

6.12	Schematic representation of dipoles pilling at the polymer/filler interface. [Source:(169)] .	87
6.13	Evolution of dielectric permittivity ϵ' (1 st heating run) at 50°C and at several frequencies (ranging from 100Hz to 1MHz) vs. aging time for the unaged, aged for 30 days, and $C1^*$ samples. [Source:(169)]	87
6.14	Characterization of the structural relaxation of the epoxy through DSC: enthalpy excess ΔH as a function of aging time for the composites $C1$ (a) and $C2$ (b). [Source:(172)]	89
6.15	Comparative breakdown field for $C1$ and $C1^*$ under divergent (a) and quasi-homogeneous (b) fields. [Source:(172)]	90
6.16	Electrical breakdown field as a function of enthalpy excess under divergent (a) and quasi homogeneous (b) field for the composite $C1$. [Source:(172)]	90
6.17	Electrical breakdown field as a function of enthalpy excess under divergent (a) and quasi homogeneous (b) field for the composite $C2$. [Source:(172)]	91
6.18	Normalized breakdown field as a function of enthalpy excess under divergent field for the composite $C1$ (■) and $C2$ (●) and under quasi homogeneous field for the composite $C1$ (□) and $C2$ (○). [Source:(172)]	91
6.19	SEM images of the degraded areas for $C2$ composite under (a) divergent field and (b) quasi-homogeneous field. [Source:(172)]	92
6.20	Electrical breakdown field as a function of aging time under divergent (a) and quasi homogeneous (b) field for the composites $C1$ (○) and $C1^*$ (●). [Source:(172)]	92
7.1	DSC scans of water-saturated and partially dried (dried in ambient environment for about 30 minutes) Nafion 117; scan rate, $10^\circ\text{C}\cdot\text{min}^{-1}$	100
7.2	Comparison of stress strain curves determined experimental (dots) and simulated with the finite element analysis applied to images (line), case of a unidirectional composite reinforced with 50 vol% of glass fibers.	101
7.3	Simultaneous measurement of the mechanical and electrical properties during low amplitude mechanical solicitations (the measurements were performed on a conducting vulcanized elastomer)	102
7.4	Energy density of common dielectric materials ⁽¹⁷⁴⁾	103
7.5	Schematic of a 4-layer film showing the layers and interphase.	103

List of Tables

- 1 Collection of Universal exponents describing the percolation transition, in the vicinity of the percolation threshold. Geometrical quantities (P : strength of the percolating network, S : average size of finite clusters, G : number of finite clusters and ξ : correlation length). Physical quantities (ε : permittivity, σ : conductivity [$S.m^{-1}$], ρ : resistivity [$\Omega.m$]). 6
- 1.1 Numerical values for the critical exponents s and t calculated on a 2D random network, and comparison with predictions of the percolation theory [Source:(39)] 14
- 5.1 Coefficients of Determination and p – values Between T_g , ΔT_g , ΔC_p , and t_{rel} [Source:(140)] 63
- 5.2 Coefficients of Determination and p – values Between T_g , ΔT_g , ΔC_p , and α [Source:(140)] 63
- 5.3 Coefficient of determination and P value between field to breakdown and α . QHF and DF stand for Quasi Homogeneous Field and Divergent Field, respectively [Source:(109)] 70
- 6.1 Main characteristics of the epoxy-based composites utilized in this study. 80
- 6.2 Characteristics of the s-shaped curves in Fig. 6.18. The data was fitted to the Boltzmann function with the help of Origin® version 7.0 from OriginLab Corporation. Comparison of the results obtained in divergent (DF) and quasi-homogeneous (QHF) fields. [Source:(172)] 93
- 6.3 Overview of the breakdown results: relative influence of the chemical and physical agings ; comparison between experimental data and numerical guesses [Source:(172)] 94

Bibliography

- [1] E. Baer, A. Hiltner, and H. Keith, “Hierarchical structure in polymeric materials,” *Science*, vol. 235, pp. 1015–1022, 1987. [2](#), [107](#)
- [2] M. Sahimi, *Applications of percolation theory*. Taylor & Francis Bristol, PA USA, 1994. [5](#), [14](#)
- [3] D. Stauffer and A. Aharony, *Introduction to percolation theory*. Taylor London, 1994. [5](#), [14](#), [17](#)
- [4] F. Lux, “Models proposed to explain the electrical conductivity of mixtures made of conductive and insulating materials,” *J. Mater. Sci.*, vol. 28, pp. 285–301, 1993. [5](#), [12](#), [24](#), [32](#)
- [5] J. Clerc, G. Giraud, J. Roussenq, R. Blanc, J. Carton, E. Guyon, H. Ottavi, and D. Stauffer, “La percolation: Modèles, simulations analogiques et numériques,” *Annales de Physique*, vol. 8, no. 1, p. 104, 1983. [5](#)
- [6] A. T. Ponomarenko, V. G. Shevchenko, and N. S. Enikolopyan, “Formation processes and properties of conducting polymer composites,” *Adv. Polym. Sci.*, vol. 96, pp. 125–47, 1990. [5](#), [32](#)
- [7] S. R. Broadbent and H. J. M., “Percolation processes: I. crystals and mazes,” *Proc. Cambridge Philos. Soc.*, vol. 53, pp. 629–641, 1957. [5](#)
- [8] S. Kirkpatrick, “Percolation and conduction,” *Rev. Modern Phys.*, vol. 45, pp. 574–588, 1973. [5](#), [12](#), [24](#)
- [9] J. P. Clerc, G. Giraud, J. M. Laugier, and J. M. Luck, “The electrical conductivity of binary disordered systems, percolation clusters, fractals, and related models,” *Adv. in Phys.*, vol. 39, pp. 191–309, 1990. [6](#), [12](#), [32](#)
- [10] R. Zallen, *Physics of amorphous solids*. Wiley, New York, 1983. [6](#), [24](#)
- [11] T. A. Ezquerra, M. Kulescza, and F. J. Balta-Calleja, “Electrical transport in polyethylene-graphite composite materials,” *Synth. Met.*, vol. 41, pp. 915–20, 1991. [6](#), [33](#)
- [12] M. B. Heaney, “Measurement and interpretation of nonuniversal critical exponents in disordered conductor-insulator composites,” *Phys. Rev. B: Condens. Matter.*, vol. 52, pp. 12 477–80, 1995. [6](#)
- [13] S. Vionnet-Menot, C. Grimaldi, T. Maeder, and S. S. P. Ryser, “Tunneling-percolation origin of nonuniversality: theory and experiments,” *Phys. Rev. B: Condens. Matter.*, vol. 71, p. 064201, 2005. [6](#), [18](#), [107](#)
- [14] J. Yacubowicz and M. Narkis, “Dielectric behavior of carbon black filled polymer composites,” *Polym. Eng. Sci.*, vol. 26, pp. 1568–73, 1986. [6](#), [33](#)
- [15] T. A. Ezquerra, M. Mohammadi, F. Kremer, T. Vilgis, and G. Wegner, “On the percolative behavior of polymeric insulator-conductor composites: polyethylene-oxide-polypyrrole,” *J. Phys. C: Solid State Phys.*, vol. 21, pp. 927–41, 1988. [6](#), [33](#)

- [16] Y. Song, T. W. Noh, S. I. Lee, and J. R. Gaines, "Experimental study of the three-dimensional ac conductivity and dielectric constant of a conductor-insulator composite near the percolation threshold," *Phys. Rev. B: Condens. Matter.*, vol. 33, pp. 904–8, 1986. [6](#)
- [17] D. S. McLachlan and M. B. Heaney, "Complex ac conductivity of a carbon black composite as a function of frequency, composition, and temperature," *Phys. Rev. B: Condens. Matter.*, vol. 60, no. 18, pp. 12 746–12 751, Nov 1999. [6](#)
- [18] P. Potschke, S. M. Dudkin, and I. Alig, "Dielectric spectroscopy on melt processed polycarbonate–multiwalled carbon nanotube composites," *Polymer*, vol. 44, no. 17, pp. 5023–5030, Aug. 2003. [6](#)
- [19] L. J. Adriaanse, J. A. Reedijk, P. A. A. Teunissen, H. B. Brom, M. A. J. Michels, and J. C. M. Brokken-Zijp, "High-dilution carbon-black/polymer composites: hierarchical percolating network derived from Hz to THz ac conductivity," *Phys. Rev. Lett.*, vol. 78, pp. 1755–1758, 1997. [6](#)
- [20] I. A. Tchmutin, A. T. Ponomarenko, V. G. Shevchenko, N. G. Ryvkina, C. Klason, and D. H. McQueen, "Electrical transport in 0-3 epoxy resin-barium titanate-carbon black polymer composites," *J. Polym. Sci., Part B: Polym. Phys.*, vol. 36, p. 1847, 1998. [6](#)
- [21] L. Flandin, G. Bidan, Y. Bréchet, and J. Y. Cavaille, "New nanocomposite materials made of an insulating matrix and conducting fillers: processing and properties," *Polym. Compos.*, vol. 21, no. 2, pp. 165–174, 2000. [7](#), [12](#), [107](#)
- [22] A. L. R. Bug, S. A. Safran, G. S. Grest, and I. Webman, "Do interactions raise or lower a percolation threshold?" *Phys. Rev. Lett.*, vol. 55, no. 18, pp. 1896–1899, Oct 1985. [7](#)
- [23] L. Flandin, T. Prasse, R. Schueler, K. Schulte, W. Bauhofer, and J. Y. Cavaille, "Anomalous percolation transition in carbon-black-epoxy composite materials," *Phys. Rev. B: Condens. Matter.*, vol. 59, no. 22, pp. 14 349–14 355, 1999. [7](#), [22](#), [32](#), [34](#), [35](#), [36](#), [108](#)
- [24] Y. Gefen, A. Aharony, and S. Alexander, "Anomalous diffusion on percolating clusters," *Phys. Rev. Lett.*, vol. 50, no. 1, pp. 77–80, Jan 1983. [12](#), [14](#)
- [25] R. K. Chakrabarty, K. K. Bardhan, and A. Basu, "Measurement of AC conductance, and minima in loss tangent, of random conductor-insulator mixtures," *J. Phys.: Condens. Matter*, vol. 5, no. 15, pp. 2377–2388, 1993. [12](#), [13](#)
- [26] J. P. Clerc, F. Brouers, and A. K. Sarychev, "Modelisation of electrical intergrain contacts at high frequencies," *Physica A: Statistical and Theoretical Physics*, vol. 241, no. 1-2, pp. 289–295, Jul. 1997. [12](#), [107](#)
- [27] Y. V. Fyodorov, "Long-ranged model of random RL-C network," *Physica E*, vol. 9, pp. 609–615, 2001. [12](#)
- [28] D. Almond and B. Vainas, "The dielectric properties of random R-C networks as an explanation of the 'Universal' power law dielectric response of solids," *J. Phys.: Condens. Matter*, vol. 11, no. 46, pp. 9081–9093, 1999. [12](#)
- [29] R. Venkatesan, J. Davis, and J. Meindl, "Compact distributed RLC interconnect models - part III: transients in single and coupled lines with capacitive load termination," *IEEE Trans. Electron. Dev.*, vol. 50, no. 4, pp. 1081–1093, 2003. [12](#)
- [30] A. L. R. Bug, S. A. Safran, G. S. Grest, and I. Webman, "Do interactions raise or lower a percolation threshold?" *Phys. Rev. Lett.*, vol. 55, pp. 1896–9, 1985. [12](#)
-

- [31] I. Balberg, “Excluded-volume explanation of Archie’s law,” *Phys. Rev. B: Condens. Matter*, vol. 33, no. 5, pp. 3618–3620, Mar 1986. [12](#)
- [32] E. J. Garboczi, K. A. Snyder, J. F. Douglas, and M. F. Thorpe, “Geometrical percolation threshold of overlapping ellipsoids,” *Phys. Rev. E: Stat. Phys., Plasmas, Fluids*, vol. 52, pp. 819–28, 1995. [12](#)
- [33] E. J. Garboczi and J. F. Douglas, “Intrinsic conductivity of objects having arbitrary shape and conductivity,” *Phys. Rev. E: Stat. Phys., Plasmas, Fluids*, vol. 53, pp. 6169–6180, 1996. [12](#)
- [34] I. Balberg and N. Binenbaum, “Computer study of the percolation threshold in a two-dimensional anisotropic system of conducting sticks,” *Phys. Rev. B: Condens. Matter*, vol. 28, no. 7, pp. 3799–3812, Oct 1983. [12](#)
- [35] I. Balberg, N. Binenbaum, and N. Wagner, “Percolation thresholds in the three-dimensional sticks system,” *Phys. Rev. Lett.*, vol. 52, no. 17, pp. 1465–1468, Apr 1984. [12](#)
- [36] L. Flandin and J. Y. Cavallé, “Electrically conductive cellulosic microfibrils and matrices reinforced therewith,” Eur. Patent 96 600 133, 1996. [12](#)
- [37] J. Y. Cavallé and L. Flandin, “Microfibrilles de cellulose conductrice et composites les incorporants,” Eur. Patent 97 400 022, 1996. [12](#)
- [38] L. Flandin, “Etude expérimentale et modélisation microstructurale de l’évolution des propriétés électriques d’un matériau composite en cours de déformation,” Ph.D. dissertation, Université Joseph Fourier - Grenoble I, Grenoble (Isère), 1998. [12](#), [33](#), [39](#)
- [39] L. Flandin, M. Verdier, B. Bouterin, Y. Bréchet, and J. Y. Cavallé, “A 3D numerical simulation of ac electrical properties of short fiber composites,” *J. Polym. Sci., Part B: Polym. Phys.*, vol. 37, no. 8, pp. 805–814, 1999. [13](#), [14](#), [15](#), [17](#), [18](#), [19](#), [49](#), [107](#), [108](#), [113](#)
- [40] J. R. Shewchuk. (1997-2006) Triangle: Engineering a 2d Quality Mesh Generator and Delaunay Triangulator. [Online]. Available: <http://www.cs.cmu.edu/~quake/triangle.html> [12](#)
- [41] —, “Triangle: Engineering a 2d Quality Mesh Generator and Delaunay Triangulator,” in *Applied computational geometry: towards geometric engineering*, ser. Lecture Notes in Computer Science, M. C. Lin and D. Manocha, Eds. Springer-Verlag, May 1996, vol. 1148, pp. 203–222, from the First Acm Workshop on Applied Computational Geometry. [12](#), [67](#)
- [42] D. Yip, “Steps - spice text editing package utilizing schematics,” EECS Department, University of California, Berkeley, Tech. Rep. UCB/ERL M91/43, 1991. [13](#), [48](#)
- [43] Spice+, “Simulation program with integrated circuit emphasis, initially developed at eecs department of the university of california at berkeley.” [13](#), [67](#)
- [44] A. Okabe, B. Boots, and K. Sugihara, *Spatial tessellation concepts and applications of Voronoi diagrams*. Wiley: New York, 1992. [13](#)
- [45] I. Balberg and N. Binenbaum, “Cluster structure and conductivity of three-dimensional continuum systems,” *Phys. Rev. A: At. Mol. Opt. Phys.*, vol. 31, no. 2, pp. 1222–1225, Feb 1985. [14](#)
- [46] J. L. Meijering, “Interface area, edge length and number of vertices in crystal aggregates with random nucleation,” *Philips Res. Rep.*, vol. 8, pp. 270–290, 1953. [15](#)
- [47] G. A. Garfunkel and M. B. Weissman, “Noise scaling of continuum percolating films,” *Phys. Rev. Lett.*, vol. 55, pp. 296–9, 1985. [18](#)
-

- [48] L. Flandin, Y. Bréchet, R. Dendievel, and J. Y. Cavaillé, "Characterization of the damage in nanocomposite materials by a.c. electrical properties: experiment and simulation," *J. Mater. Sci.*, vol. 34, no. 8, pp. 1753–1759, 1999. [20](#), [22](#)
- [49] F. Dalmas, R. Dendievel, L. Chazeau, J.-Y. Cavaille, and C. Gauthier, "Carbon nanotube-filled polymer composites. numerical simulation of electrical conductivity in three-dimensional entangled fibrous networks," *Acta Mater.*, vol. 54, no. 11, pp. 2923–2931, Jun. 2006. [20](#)
- [50] G. Kraus, Ed., *Reinforcement of elastomers*. Ed. Interscience, New York, 1965. [22](#)
- [51] B. B. Boonstra, *Rubber technology and manufacture 2nd Ed*, C. M. Blow and C. Hepburn, Eds. Butterworth, London, for the Plastics and Rubber Institute, 1982. [22](#), [28](#)
- [52] K. P. Sau, T. K. Chaki, and D. Khastgir, "Carbon fiber filled conductive composites based on nitrile rubber (NBR), ethylene propylene diene rubber (EPDM) and their blend," *Polymer*, vol. 39, pp. 6461–6471, 1998. [22](#)
- [53] S. K. Bhattacharya, *Metal-filled polymers - properties and applications*, M. Dekker, Ed. Plastics Engineering, 1986. [22](#)
- [54] S. Bensason, J. Minick, A. Moet, S. Chum, A. Hiltner, and E. Baer, "Classification of homogeneous ethylene-octene copolymers based on comonomer content," *J. Polym. Sci., Part B: Polym. Phys.*, vol. 34, pp. 1301–15, 1996. [22](#), [108](#)
- [55] S. Bensason, S. Nazarenko, S. Chum, A. Hiltner, and E. Baer, "Elastomeric blends of homogeneous ethylene-octene copolymers," *Polymer*, vol. 38, pp. 3913–3919, 1997. [22](#)
- [56] —, "Blends of homogeneous ethylene-octene copolymers," *Polymer*, vol. 38, pp. 3513–3520, 1997. [22](#)
- [57] S. Bensason, E. V. Stepanov, S. Chum, A. Hiltner, and E. Baer, "Deformation of elastomeric ethylene-octene copolymers," *Macromolecules*, vol. 30, pp. 2436–2444, 1997. [22](#), [26](#), [29](#)
- [58] J.-C. Huang and H.-L. Huang, "Carbon black filled metallocene ethylene-octene copolymers," *J. Polym. Eng.*, vol. 17, pp. 213–229, 1997. [22](#), [27](#)
- [59] F. Carmona, "Conducting filled polymers," *Physica A*, vol. 157, pp. 461–9, 1989. [22](#), [32](#)
- [60] K. Miyasaka, K. Watanabe, E. Jojima, H. Aida, M. Sumita, and K. Ishikawa, "Electrical conductivity of carbon-polymer composites as a function of carbon content," *J. Mater. Sci.*, vol. 17, pp. 1610–16, 1982. [22](#), [32](#)
- [61] M. Narkis, A. Ram, and Z. Stein, "Electrical properties of carbon black filled crosslinked polyethylene," *Polym. Eng. Sci.*, vol. 21, pp. 1049–54, 1981. [22](#), [29](#)
- [62] X.-S. Yi, G. Wu, and D. Ma, "Property balancing for polyethylene-based carbon black-filled conductive composites," *J. Appl. Polym. Sci.*, vol. 67, pp. 131–138, 1998. [22](#), [29](#)
- [63] J. Kost, M. Narkis, and A. Foux, "Effects of axial stretching on the resistivity of carbon black-filled silicone rubber," *Polym. Eng. Sci.*, vol. 23, pp. 567–71, 1983. [22](#), [28](#)
- [64] L. Flandin, A. Chang, S. Nazarenko, A. Hiltner, and E. Baer, "Effect of strain on the properties of an ethylene-octene elastomer with conductive carbon fillers," *J. Appl. Polym. Sci.*, vol. 76, no. 6, pp. 894–905, 2000. [22](#), [23](#), [24](#), [28](#), [108](#)
- [65] L. Flandin, A. Hiltner, and E. Baer, "Interrelationships between electrical and mechanical properties of a carbon black-filled ethylene-octene elastomer," *Polymer*, vol. 42, no. 2, pp. 827–838, 2001. [23](#), [25](#), [26](#), [27](#), [28](#), [29](#), [30](#), [108](#)
-

- [66] A. Payne, *Reinforcement of elastomers*, G. Kraus, Ed. Ed. Interscience, New York, 1965. 25
- [67] T. Kurian, P. P. De, D. Khastgir, D. K. Tripathy, S. K. De, and D. G. Peiffer, "Reinforcement of EPDM-based ionic thermoplastic elastomer by carbon black," *Polymer*, vol. 36, pp. 3875–84, 1995. 25, 26
- [68] K. P. Sau, T. K. Chaki, and D. Khastgir, "Electrical and mechanical properties of conducting carbon black filled composites based on rubber and rubber blends," *J. Appl. Polym. Sci.*, vol. 71, pp. 887–895, 1999. 25
- [69] E. Guth, "Theory of filler reinforcement," *J. Appl. Phys.*, vol. 16, pp. 20–5, 1945. 25
- [70] X. Shui and D. D. L. Chung, "A new electromechanical effect in discontinuous-filament elastomer-matrix composites," *Smart Mater. Struct.*, vol. 6, pp. 102–105, 1997. 27
- [71] R. H. Norman, *Conductive rubbers and plastics*. Elsevier, Amsterdam., 1970. 27
- [72] J. Kost, M. Narkis, and A. Foux, "Resistivity behavior of carbon-black-filled silicone rubber in cyclic loading experiments," *J. Appl. Polym. Sci.*, vol. 29, pp. 3937–46, 1984. 28
- [73] Y. Fukahori and W. Seki, "Stress analysis of elastomeric materials at large extensions using the finite element method. part III. coalescence of primary and secondary cracks and generation of fracture surface roughness," *J. Mater. Sci.*, vol. 29, pp. 2767–74, 1994. 29
- [74] J.-B. Donnet, "Fifty years of research and progress on carbon black," *Carbon*, vol. 32, pp. 1305–10, 1994. 29, 30, 108
- [75] J. L. Leblanc, "A molecular explanation for the origin of bound rubber in carbon black filled rubber compounds," *J. Appl. Polym. Sci.*, vol. 66, pp. 2257–2268, 1997. 29, 30, 108
- [76] L. Karasek and M. Sumita, "Characterization of dispersion state of filler and polymer-filler interactions in rubber-carbon black composites," *J. Mater. Sci.*, vol. 31, pp. 281–9, 1996. 29, 32
- [77] J. Andrade, J. S., N. Ito, and Y. Shibusu, "Percolation transition in conducting polymer networks," *Phys. Rev. B: Condens. Matter.*, vol. 54, pp. 3910–3915, 1996. 32
- [78] C. M. Fortuin and P. W. Kasteleyn, "On the random-cluster model : I. introduction and relation to other models," *Physica*, vol. 57:4, pp. 536–564, 15 February 1972. 32
- [79] J. R. Harbour, M. J. Walzak, and R. P. Veregin, "Determination of the origin of the narrow ESR signal in carbon black filled polymers," *J. Colloid Interface Sci.*, vol. 138, no. 2, pp. 380–387, 1990. 32
- [80] R. Schueler, J. Petermann, K. Schulte, and H.-P. Wentzel, "Agglomeration and electrical percolation behavior of carbon black dispersed in epoxy resin," *J. Appl. Polym. Sci.*, vol. 63, pp. 1741–1746, 1997. 32, 33
- [81] E. J. W. Verwey and J. T. G. Overbeek, *Theory of the stability of lyophobic colloids*. Elsevier, Amsterdam, 1948. 32, 37
- [82] R. Schüler, "Entwicklung polymerer verbundwerkstoffe mit elektrischer leitfähigkeit," Ph.D. dissertation, TU Hamburg-Harburg, 1994. 33, 34, 39
- [83] M. Connor, S. Roy, T. Ezquerra, and F. Baltá Calleja, "Broadband a.c. conductivity of conductor-polymer composites," *Phys. Rev. B: Condens. Matter.*, vol. 57, pp. 2286–2294, 1998. 34
-

- [84] T. Prasse, L. Flandin, K. Schulte, and W. Bauhofer, "in situ observation of electric field induced agglomeration of carbon black in epoxy resin," *Appl. Phys. Lett.*, vol. 72, no. 22, pp. 2903–2905, 1998. [35](#), [38](#), [39](#), [108](#), [109](#)
- [85] T. Prasse, M.-K. Schwarz, K. Schulte, and W. Bauhofer, "The interaction of epoxy resin and an additional electrolyte with non-oxidised carbon black in colloidal dispersions," *Colloids Surf., A*, vol. 189, pp. 183–188, 2001. [40](#), [109](#)
- [86] T. Prasse, L. Flandin, and F. Knopf, "Werkstoff und Verfahren zum herstellen desselben," Eur. Patent 99 118 734, 1998. [40](#)
- [87] T. Prasse, L. Flandin, and H. Kunzig, "Herstellungsverfahren für einen Elektrostatisch leitfähigen Belag sowie danach hergestellter Belag," Eur. Patent 99 118 710, 1998. [40](#)
- [88] L. Dissado and J. Fothergill, *Electrical degradation and breakdown in polymers*, P. P. Ltd., Ed. G.C. Stevens, 1992. [43](#), [44](#), [45](#), [48](#), [58](#), [59](#), [68](#), [71](#), [78](#), [109](#)
- [89] H. Frohlich, "On the theory of dielectric breakdown in solids," *Proc. Roy. Soc. A*, vol. 188, pp. 521–532, 1947. [43](#)
- [90] J. J. O'Dwyer and B. L. Beers, "Thermal breakdown in dielectrics," in *1981 Annual Report Conference on Electrical Insulation and Dielectric Phenomena*, IEEE, 1981, pp. 193–198. [43](#)
- [91] J. K. Nelson, "The nature of divergent-field surge-voltage endurance in epoxy resin," *IEEE Trans. Diel. Electr. Insul.*, vol. 7, no. 6, pp. 764–771, 2000. [43](#)
- [92] K. Stark and C. Garton, "Electric strength of irradiated polythene," *Nature*, vol. 176, pp. 1225–1226, 1955. [43](#)
- [93] E. Hallen, *Electromagnetic theory*. Chapman & Hall, 1962. [43](#)
- [94] C. Brosseau and A. Béréal, "Computational electromagnetics and the rational design of new dielectric heterostructures," *Prog. Mater Sci.*, vol. 48, no. 5, pp. 373–456, 2003. [43](#)
- [95] C. Hudon, R. Bartnikas, and M. R. Wertheimer, "Effect of physico-chemical degradation of epoxy resin on partial discharge behavior," *IEEE Trans. Diel. Electr. Insul.*, vol. 2, no. 6, pp. 1083–1094, 1995. [43](#), [44](#)
- [96] V. Champion, J and J. Dodd, S, "The effect of voltage and material age on the electrical tree growth and breakdown characteristics of epoxy resins," *J. Phys. D: Appl. Phys.*, vol. 28, no. 2, pp. 398–407, 1995. [43](#), [45](#), [48](#), [58](#), [75](#), [90](#)
- [97] J. V. Champion, S. J. Dodd, and J. M. Alison, "The correlation between the partial discharge behaviour and the spatial and temporal development of electrical trees grown in an epoxy resin," *J. Phys. D: Appl. Phys.*, vol. 29, no. 10, pp. 2689–2695, 1996. [43](#), [58](#)
- [98] G. Loeffelmacher, "Über physikalisch chemischen vorgänge bei der ausbildung von entladungskanaelen in polyethylen und epoxydharz im inhomogenen wechelfeld," Ph.D. dissertation, Tu Hannover, 1976. [44](#)
- [99] T. Las, "Measurement of solid dielectric surface temperature increment arising from partial discharge activity," in *Conf. record of the 2000 IEEE International Symposium on Electrical Insulation*, Anaheim Usa, 2000. [44](#), [78](#)
- [100] S. Montserrat, "Physical aging studies in epoxy resins. I. kinetics of the enthalpy relaxation process in a fully cured epoxy resin," *J. Polym. Sci., Part B: Polym. Phys.*, vol. 32, no. 3, pp. 509–522, 1994. [44](#), [78](#), [79](#), [84](#), [85](#), [110](#)
-

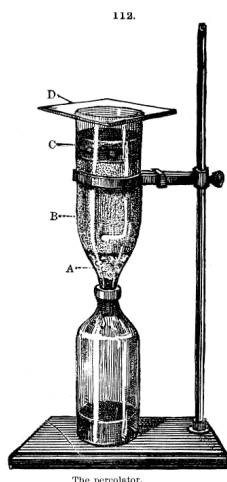
- [101] M. Beyer, *Electrical and dielectric behaviour of cast epoxy resins*. Institute of Electric Power Systems(Schering-Institute), Hannover University,, 1991, vol. 1. 44, 68, 78
- [102] V. Ollier-Dureault and B. Gosse, “Photo-oxidation and electrical aging of anhydride-cured epoxy resins,” *IEEE Trans. Diel. Electr. Insul.*, vol. 5, no. 6, pp. 935–943, 1998. 44, 78
- [103] D. M. Hepburn, I. J. Kemp, and J. M. Cooper, “Degradation of filled epoxy resin surfaces,” *Polym. Degrad. Stab.*, vol. 70, no. 2, pp. 245–251, 2000. 44, 78, 81
- [104] D. Hepburn, I. Kemp, A. Shields, and J. Cooper, “Degradation of epoxy resin by partial discharges,” *IEE Proc. Sci. Meas. Technol.*, vol. 147, no. 3, pp. 97–104, 2000. 44, 78, 81
- [105] D. Auckland, J. Cooper, and B. Varlow, “Factors affecting electrical tree testing,” *IEE Proceedings A*, vol. 139, no. 1, pp. 9–13, 1992. 45, 58
- [106] K. Wu, Y. Suzuoki, T. Mizutani, and H. Xie, “Model for partial discharges associated with treeing breakdown: III. PD extinction and re-growth of tree,” *J. Phys. D: Appl. Phys.*, vol. 33, pp. 1209–1218, 2000. 48, 58
- [107] L. A. Dissado and P. J. J. Sweeney, “Physical model for breakdown structures in solid dielectrics,” *Phys. Rev. B: Condens. Matter.*, vol. 48, no. 22, pp. 16 261–16 268, 1993. 48, 50, 68, 72
- [108] J. Martin, C. Tigges, R. Anderson, and J. Odinek, “Enhanced dielectric standoff and mechanical failure in field-structured composites,” *Physical Review. B, Condensed Matter*, vol. 60, no. 10, pp. 7127–7139, 1999. 48, 49, 50, 72, 73
- [109] L. Flandin, L. Vouyovitch, A. Bérroual, J. L. Bessède, and N. D. Albérola, “Influences of degree of curing and presence of inorganic fillers on the ultimate electrical properties of epoxy-based composites: experiment and simulation,” *J. Phys. D: Appl. Phys.*, vol. 38, no. 1, pp. 144–155, 2005. 48, 52, 54, 66, 67, 68, 69, 70, 71, 72, 73, 74, 75, 93, 103, 109, 110, 113
- [110] L. Dissado, “Understanding electrical trees in solids: From experiment to theory,” in *Laboratoire Matériaux Organiques à Propriétés Spécifiques, Chambéry, France*, April 2nd 2004. 49
- [111] P. Sweeney, L. Dissado, and J. Cooper, “Simulation of the effect of barriers upon electrical tree propagation,” *J. Phys. D: Appl. Phys.*, vol. 25, no. 1, pp. 113–119, 1992, kik. 50, 58, 91
- [112] A. L. Barclay, P. J. Sweeney, L. A. Dissado, and G. C. Stevens, “Stochastic modelling of electrical treeing: fractal and statistical characteristics,” *J. Phys. D: Appl. Phys.*, vol. 23, no. 12, pp. 1536–1545, 1990. 50, 68, 91
- [113] L. Flandin, L. Vouyovitch, N. Barraud, J. Bessède, A. Bérroual, and N. D. Albérola, “Modeling the dielectric breakdown in epoxy-based heterogeneous systems,” *High Voltage Engineering (ISH) J Smith Editor*, vol. 1, pp. 123–125, 2003. 50, 109
- [114] L. Flandin, J. Bessède, L. Vouyovitch, A. Bérroual, and N. D. Albérola, “Toward realistic modelling of dielectric breakdown in heterogeneous systems,” in *the 9th INSUCON International Electrical Insulation Conference (Berlin, Germany 18-20 June 2002)*, 2002. 50, 52, 67, 72, 109
- [115] W. Kai, Y. Suzuoki, T. Mizutani, and X. Hengkun, “Model for partial discharges associated with treeing breakdown : III. PD extinction and re-growth of tree,” *J. Phys. D: Appl. Phys.*, vol. 33, no. 10, pp. 1209–1218, 2000. 51
- [116] W. Rasband, *ImageJ is a free processing software developed at National Institutes of Health*, NIH, 1997. 51, 67
-

- [117] D. Stark, "Analysis of power supply networks in VLSI circuits," Computer Systems Laboratory, Departments of Electrical Engineering and Computer Science, Stanford University, Tech. Rep., 1991. 51, 72
- [118] —, "Analysis of power supply networks in vlsi circuits," CSL-TR-91-465, Stanford University, California, Computer Systems Laboratory Departments of Electrical Engineering and Computer Science Stanford University Stanford, California 943054055, 1991. 51, 109
- [119] Z. Djemai and A. Beroual, "Fractal dimension of discharges propagation on insulating interfaces," *Archives of Electrical Engineering*, vol. 47, no. 3, pp. 251–256, 1998. 58
- [120] V. Champion, J and J. Dodd, S, "Systematic and reproducible partial discharge patterns during electrical tree growth in an epoxy resin," *J. Phys. D: Appl. Phys.*, vol. 29, no. 3, pp. 862–868, 1996. 58, 68
- [121] O. Poznansky, "Bush region in the propagation of electrical degradation in polymers," *Comput. Theor. Polym. Sci.*, vol. 11, pp. 81–82, 2001. 58
- [122] K. Wu, Y. Sukuoki, T. Mizutani, and H. Xie, "Model for partial discharges associated with treeing breakdown : II. tree growth affected by pds," *J. Phys. D: Appl. Phys.*, vol. 33, pp. 1202–1208, 2000. 58
- [123] M. Nedjar, A. Boubakeur, A. Beroual, and M. Bournane, "Thermal aging of polyvinyl chloride used in electrical insulation," *Ann. Chim. - Sci. Mat.*, vol. 28, no. 5, pp. 97–104, 2003. 58
- [124] J. Holboll and M. Henriksen, "Partial discharge patterns and surface deterioration in voids in filled and unfilled epoxy," in *Conf. record of the 1992 IEEE international symposium on electrical insulation*, Baltimore Usa, 1992, pp. 354–358. 58, 59
- [125] C. P. Wong and R. S. Bollampally, "Mixed filler combinations for enhanced thermal conductivity of liquid for electronic packaging," in *1999 international symposium on advanced packaging materials*, 1999, pp. 113–117. 58
- [126] Y. S. Cho, M. J. Shim, and S. W. Kim, "Dielectric breakdown phenomena in Al₂O₃ filled DGEBA/MDA/SN composite system," *Compos. Interfaces*, vol. 8, no. 6, pp. 427–433, 2001. 58, 59, 68
- [127] A. Dissado, L. G. Mazzanti, and C. Montanari, G, "The role of trapped space charges in the electrical aging of insulating materials. digest of literature on dielectrics," *IEEE Trans. Dielect. Electr. Insul.*, vol. 4, no. 5, pp. 496–506, 1997. 58
- [128] T. Farr, R. Vogelsang, and K. Fr  hlich, "Propagation along barrier-interfaces in epoxy resin," in *Conference on electrical insulation and dielectric phenomena, CEIDP*, Cancun, Mexico, 2002. 58, 72
- [129] I. Fofana, A. Beroual, and A. Boubakeur, "Influence of insulating barriers on positive long air gaps in divergent field." in *11th International Symposium on High-Voltage Engineering (ISH 99) High Voltage Engineering : London, 23-27 August 1999.*, Iee-Conference-Publication, Ed., 1999, pp. (467; P.1) : 3.321.P3–3.324.P3. 58
- [130] S. M. Lebedev, O. S. Gefle, Y. P. Pokholkov, E. Gockenbach, H. Borsi, V. Wasserberg, N. Abedi, and J. Szczechowski, "Influence of high-permittivity barriers on PD activity in three-layer dielectrics," *J. Phys. D: Appl. Phys.*, vol. 37, no. 22, pp. 3155–3159, 2004. 58
- [131] S. Fugita, M. Ruike, and M. Baba, "Treeing breakdown voltage and tsc of alumina filled epoxy resin," in *IEEE annual report - Conference on electrical insulation and dielectric phenomena*, San Fransisco, 1996, pp. 738–741. 58, 71
-

- [132] P. Henk, T. Kortsens, and T. Kvarts, "Increasing the electrical discharge endurance of acid anhydride cured dgeba epoxy resin by dispersion of nanoparticle silica," *High Perform. Polym.*, vol. 11, no. 3, pp. 281–296, 1999. 58, 59
- [133] R. Masuda, W. Takahashi, and M. Ishii, "Particle size distribution of spherical silica gel produced by sol-gel method," *J. Non-Cryst. Solids*, vol. 121, no. 1-3, pp. 389–393, 1990. 59
- [134] W. Cook, M. Mehrabi, and G. Edward, "Ageing and yielding in model epoxy thermosets," *Polymer*, vol. 40, pp. 1209–1218, 1999. 59
- [135] A. Chateauminois, B. Chabert, J. P. Soulier, and L. Vincent, "Hygrothermal ageing effects on the static fatigue of glass/epoxy composites," *Composites*, vol. 24, no. 7, pp. 547–555, 1993. 59
- [136] G. C. Stevens and M. J. Richardson, "Factors influencing the glass transition of DGEBA-anhydride epoxy resins," *Polymer*, vol. 24, no. 7, pp. 851–858, 1983. 59
- [137] G. Van Assche and B. Van Mele, "Interphase formation in model composites studied by micro-thermal analysis," *Polymer*, vol. 43, no. 17, pp. 4605–4610, 2002. 59
- [138] J. L. Bailleul, V. Sobotka, D. Delaunay, and Y. Jarny, "Inverse algorithm for optimal processing of composite materials," *Composites Part A*, vol. 34, no. 8, pp. 695–708, Aug. 2003. 59, 60
- [139] F. Y. C. Boey and W. Qiang, "Experimental modeling of the cure kinetics of an epoxy-Hexaanhydro-4-Methylphthalicanhydride (MHHPA) system," *Polymer*, vol. 41, no. 6, pp. 2081–2094, 2000. 59
- [140] L. Vouyovitch, L. Flandin, G. Merle, J. L. Bessède, and N. D. Albérola, "Influence of the processing on the completion of curing in epoxy-based composites," *J. Appl. Polym. Sci.*, vol. 96, no. 4, pp. 1368–1376, 2005. 60, 61, 62, 63, 64, 66, 93, 109, 113
- [141] *Differential scanning calorimetry (DSC) - part 1 : general principles (ISO 11357-1:1997)*, Standardization, the International Organization for, 1998. 61
- [142] J. P. Pascault and R. J. J. Williams, "Glass transition temperature versus conversion relationships for thermosetting polymers," *J. Polym. Sci., Part B: Polym. Phys.*, vol. 28, no. 1, pp. 85–95, 1990. 62, 66
- [143] S. Montserrat, "Vitrification and physical ageing on isothermal curing of an epoxy resin," *J. Therm. Anal.*, vol. 37, pp. 1751–1758, 1991. 62, 78
- [144] —, "Vitrification and further structural relaxation in the isothermal curing of an epoxy resin," *J. Appl. Polym. Sci.*, vol. 44, no. 3, pp. 545–554, 1992. 62, 78
- [145] —, "Effect of crosslinking density on $\Delta C_p(tg)$ in an epoxy network," *Polymer*, vol. 36, no. 2, pp. 435–436, 1995. 62, 78
- [146] —, "Calorimetric measurement of the maximum glass transition temperature in a thermosetting resin," *J. Therm. Anal.*, vol. 40, pp. 553–563, 1993. 62, 78
- [147] J. Tukey, *Exploratory data analysis*. Princeton University: Addison-Wesley, 1977. 62
- [148] Y. Calventus, S. Montserrat, and J. M. Hutchinson, "Enthalpy relaxation of non-stoichiometric epoxy-amine resins," *Polymer*, vol. 42, no. 16, pp. 7081–7093, 2001. 64, 65
- [149] H. Stutz, "Theoretical evaluation and the effect of thermal degradation on the time-temperature-transformation (TTT) diagram of bisphenol a epoxies," *J. Appl. Polym. Sci.*, vol. 89, no. 14, pp. 3894–3896, 2003. 64
-

- [150] M. Akatsuka, Y. Takezawa, and S. Amagi, "Influences of inorganic fillers on curing reactions of epoxy resins initiated with a boron trifluoride amine complex," *Polymer*, vol. 42, no. 7, pp. 3003–3007, 2001. 65
- [151] W. G. Kim and J. Y. Lee, "Contributions of the network structure to the cure kinetics of epoxy resin systems according to the change of hardeners," *Polymer*, vol. 43, no. 21, pp. 5713–5722, 2002. 65
- [152] L. Vouyovitch, "Relations entre architecture et rupture diélectrique de composites isolants-isolants : approches expérimentale et théorique," Ph.D. dissertation, Université de Savoie, 2004. 66
- [153] J. Mason, "Breakdown of solid dielectrics in divergent fields," *Proc Iee*, vol. 102, pp. 254–258, 1955. 67, 69
- [154] H. Cheng and S. Torquato, "Electric-field fluctuations in random dielectric composites," *Phys. Rev. B: Condens. Matter.*, vol. 56, no. 13, pp. 8060–8068, 1997. 67, 72
- [155] L. Flandin and N. D. Albérola, "An innovative numerical tool to determine both local and global physical properties of strongly heterogeneous systems," *To Be Published*, vol. 0, p. XXX, 2007. 67
- [156] A. Gupta and A. Sen, "Aspects of breakdown in a model for disordered non-linear composites," *Physica A*, vol. 247, pp. 30–40, 1997. 71
- [157] T. Farr, R. Vogelsang, and K. Frohlich, "A new deterministic model for tree growth in polymers with barriers," in *2001 annual report conference on electrical insulation and dielectric phenomena*, 2001, pp. 673–676. 72
- [158] J. E. Martin, R. A. Anderson, and C. P. Tigges, "Simulation of the athermal coarsening of composites structured by a uniaxial field," *J. Chem. Phys.*, vol. 108, no. 9, pp. 3765–3787, 1998. 72
- [159] E. Martin, J. A. Anderson, R. and P. Tigges, C, "Simulation of the athermal coarsening of composites structured by a biaxial field," *J. Chem. Phys.*, vol. 108, no. 18, pp. 7887–7900, 1998. 72
- [160] V. Ollier-Dureault, "Vieillessement de surfaces d'isolateurs en résine époxy-anhydride : rôles respectifs des uv et du champ électrique," Ph.D. dissertation, Université Joseph Fourier, 1995. 78
- [161] V. Ollier-Dureault and B. Gosse, "Photooxidation of anhydride-cured epoxies: FTIR study of the modifications of the chemical structure," *J. Appl. Polym. Sci.*, vol. 70, no. 6, pp. 1221–1237, 1998. 78
- [162] A. J. Kovacs and J. M. Hutchinson, "Isobaric thermal behavior of glasses during uniform cooling and heating. Dependence of the characteristic temperatures on the relative contributions of temperature and structure to the rate of recovery. II. a one-parameter model approach," *J. Polym. Sci., B, Polym. Phys. E.*, vol. 17, no. 12, pp. 2031–2058, 1979. 78, 84, 85, 88
- [163] N. Heymans and B. Dequenne, "Relationship between conformation and enthalpy or volume relaxation in polycarbonate," *Polymer*, vol. 42, no. 12, pp. 5337–5342, 2001. 78
- [164] J. M. Hutchinson, "Physical aging of polymers," *Prog. Polym. Sci.*, vol. 20, no. 4, pp. 703–760, 1995. 78, 85
- [165] S. Montserrat, "Enthalpy relaxation of an epoxy-anhydride resin by temperature-modulated differential scanning calorimetry," *J. Polym. Sci., Part B: Polym. Phys.*, vol. 38, pp. 2272–2284, 2000. 78
- [166] S. Montserrat, C. Flaque, M. Calafell, G. Andreu, and J. Malek, "Influence of the accelerator concentration on the curing reaction of an epoxy-anhydride system," *Thermochim. Acta*, vol. 269–270, pp. 213–229, 1995. 78
-

- [167] S. Montserrat, J. Malek, and P. Colomer, “Thermal degradation kinetics of epoxy-anhydride resins : II. influence of a reactive diluent,” *Thermochim. Acta*, vol. 336, pp. 65–71, 1999. 78
- [168] —, “Thermal degradation kinetics of epoxy-anhydride resins : I. influence of a silica filler,” *Thermochim. Acta*, vol. 313, pp. 83–95, 1999. 78
- [169] L. Vouyovitch, L. Flandin, J. L. Bessède, and N. D. Albérola, “Evolutions of microstructure and dielectric behaviour of epoxy based insulator-insulator composites over long periods of time,” *J. Appl. Polym. Sci.*, vol. 100, pp. 3454–3464, June 2006. 79, 80, 81, 82, 83, 84, 85, 86, 87, 93, 110, 111
- [170] R. A. Pethrick and D. Hayward, “Real time dielectric relaxation studies of dynamic polymeric systems,” *Prog. Polym. Sci.*, vol. 27, no. 9, pp. 1983–2017, 2002. 83
- [171] C. Bauwens, Crowet and C. Bauwens, J, “Annealing of polycarbonate below the glass transition temperature up to equilibrium: a quantitative interpretation of enthalpy relaxation,” *Polymer*, vol. 27, no. 5, pp. 709–713, 1986. 84, 85, 88
- [172] L. Vouyovitch, N. D. Albérola, A. Bérroual, J. L. Bessède, and L. Flandin, “Dielectric breakdown of epoxy-based composites: relative influence of physical and chemical aging,” *IEEE Trans. Diel. Electr. Insul.*, vol. 13, no. 2, pp. 282–292, January 2006. 89, 90, 91, 92, 93, 94, 111, 113
- [173] Z. Lu, E. Manias, and D. Macdonald, “Dielectric relaxation spectroscopy studies on water-saturated nafion 117 membranes,” in *Electrochemical Society, 204th National Meeting*, 2003. 100
- [174] B. Tuttle, “Capacitor technologies: A comparison of competing options,” in *Sandia National Laboratories; Albuquerque, NM*. Baltimore , Maryland: DOE Hi-Tech Inverter Meeting, October 13 2004. 103, 111
- [175] R. Y. F. Liu, A. P. Ranade, H. P. Wang, T. E. Bernal-Lara, A. Hiltner, and E. Baer, “Forced assembly of polymer nanolayers thinner than the interphase,” *Macromolecules*, vol. 38, pp. 10 721–10 727, 2005. 103
- [176] J. Karger-Kocsis, *Polypropylene - An A-Z Reference*. Springer - Verlag., 1999. 103



Available online : http://www.sgm.univ-savoie.fr/HDR_LF/